

# Production and Evaluation of Novel Brachytherapy Sources

GABRIEL FAMULARI

MEDICAL PHYSICS UNIT  
MCGILL UNIVERSITY, MONTREAL

AUGUST, 2016

*A thesis submitted to McGill University  
in partial fulfillment of the requirements  
for the degree of Master of Science*

©Gabriel Famulari, 2016

*“The most beautiful thing we can experience is the mysterious. It is the source of all true art and science.”*

Albert Einstein

## ABSTRACT

Gamma emitting radioisotopes such as  $^{75}\text{Se}$ ,  $^{169}\text{Yb}$  and  $^{153}\text{Gd}$  are attractive candidates as brachytherapy radiation sources. The first aim of this work was to evaluate the potential of these novel sources, in terms of radiobiological advantages, for applications in high dose rate (HDR) brachytherapy. The radiation quality of these potential sources was evaluated using a combination of track structure simulations and numerical microdosimetric techniques, and the weighting factor related to fractionated radiotherapy was predicted from the microdosimetric distributions. The weighting factors were 1.10, 1.14, and 1.19 for  $^{75}\text{Se}$ ,  $^{169}\text{Yb}$  and  $^{153}\text{Gd}$ , respectively, which are considerably above unity. The second aim of this work was to examine the viability of production of  $^{153}\text{Gd}$  sources through radiochemistry experiments performed at McMaster Nuclear Reactor (MNR). A new, lower, effective thermal neutron capture cross section was evaluated, and the maximum achievable specific activity was predicted to be about 70 Ci/g of  $^{152}\text{Gd}$ . In addition, a purification method and a method to load the radioisotope onto a substrate for encapsulation were demonstrated to be effective. Finally, brachytherapy sources with intermediate energy have radial dose functions that are ideal for HDR brachytherapy application and present various dosimetric, microdosimetric, and radiobiological advantages over sources currently used in HDR brachytherapy, while reducing shielding requirements for the brachytherapy suite. Such sources can also potentially be used in combination with a rotating shield delivery system to deliver intensity modulated brachytherapy (IMBT).

## RÉSUMÉ

Des radioisotopes émetteurs de rayons gamma tels que  $^{75}\text{Se}$ ,  $^{169}\text{Yb}$  et  $^{153}\text{Gd}$  sont des excellents candidats comme sources de radiation pour la curiethérapie. Le premier objectif de ce travail était d'évaluer le potentiel de ces sources nouvelles, en termes d'avantages radiobiologiques, pour des applications en curiethérapie à haut débits de dose (HDD). La qualité de la radiation de ces sources potentielles a été évaluée en utilisant une combinaison de calculs Monte Carlo de la trajectoire exacte des particules et de techniques microdosimétriques numériques, et le facteur de pondération lié à la radiothérapie fractionnée a été prédite à partir de la distribution microdosimétrique. Les facteurs de pondération de rayonnement étaient 1,10, 1,14, et 1,19 pour  $^{75}\text{Se}$ ,  $^{169}\text{Yb}$  et  $^{153}\text{Gd}$ , respectivement, nettement au-dessus de l'unité. Le deuxième objectif de ce travail était d'examiner la viabilité de la production des sources de  $^{153}\text{Gd}$  grâce à des expériences de radiochimie réalisées au réacteur nucléaire de l'Université McMaster. Une nouvelle, plus basse, section efficace de capture de neutrons thermiques a été évaluée, et l'activité spécifique réalisable maximale a été estimée à environ 70 Ci/g de  $^{152}\text{Gd}$ . En plus, une méthode de purification et une méthode pour charger le radioisotope sur un substrat pour l'encapsulation se sont avérés efficaces. Enfin, les sources de curiethérapie avec énergie intermédiaire présentent des fonctions de dose radiale idéales pour la curiethérapie à HDD et présentent divers avantages dosimétriques, microdosimétriques et radiobiologiques comparé aux sources utilisées actuellement pour la curiethérapie à HDD, tout en réduisant les exigences de radioprotection pour la suite de curiethérapie. Ces sources peuvent également être utilisée en combinaison avec un système d'écran rotatif pour livrer la curiethérapie avec modulation d'intensité.

## *Acknowledgements*

I would like to thank my supervisor, Dr. Shirin Abbasinejad Enger, for guidance, encouragement and support throughout my academic studies. I would like to thank Dr. Andrea Armstrong, who, as a collaborator on our project, provided access to her laboratories and equipment at the McMaster Nuclear Reactor (MNR) High Level Laboratory Facilities (HLLF), guided numerous experiments in a short amount of time and provided much needed hands-on help. I would like to acknowledge all the help I have received from my co-authors: Dr. Andrea Armstrong, Tomas Urlich, Piotr Pater, and Dr. Shirin Abbasinejad Enger. I would like to thank Marc-André Renaud and Dr. Shirin Abbasinejad Enger for hands-on help with the Monte Carlo code Geant4. I would like to acknowledge support from the CREATE Medical Physics Research Training Network grant (number 432290) of the Natural Sciences and Engineering Research Council (NSERC) and NSERC discovery grant (number 241018). Finally, I would like to thank my peers for all the help they have provided and for all the fruitful discussions.

## CONTRIBUTION OF AUTHORS

This thesis is fully written by Gabriel Famulari. The core work of this thesis consists of 2 manuscripts, which will be submitted to peer-reviewed journals for initial review.

The first manuscript (Paper 1), "Microdosimetric evaluation of intermediate energy brachytherapy sources using Geant4-DNA", Gabriel Famulari, Piotr Pater, Shirin Abbasinejad Enger, presents work conducted by Gabriel Famulari. Piotr Pater assisted in the formulation of the methodology, and provided the codes used to perform track structure simulations and to sample tracks. Dr. Shirin Abbasinejad Enger provided general guidance and supervision.

The second manuscript (Paper 2), "Practical aspects of  $^{153}\text{Gd}$  as a radioactive source for use in brachytherapy", Gabriel Famulari, Tomas Urlich, Andrea Armstrong, Shirin Abbasinejad Enger, presents work conducted by Gabriel Famulari. Tomas Urlich conducted the chemical separation experiments. Dr. Andrea Armstrong provided access to her laboratories, provided the equipment to perform the experiments, helped conduct experiments and provided general guidance. Dr. Shirin Abbasinejad Enger provided general guidance and supervision.

# Contents

<b>Abstract</b>	<b>iii</b>
<b>Résumé</b>	<b>iv</b>
<b>Acknowledgements</b>	<b>iv</b>
<b>Contribution of Authors</b>	<b>vi</b>
<b>1 Background</b>	<b>1</b>
1.1 Cancer . . . . .	1
1.2 Radiation therapy . . . . .	2
1.3 Conventional brachytherapy . . . . .	3
1.3.1 Types of brachytherapy implants . . . . .	3
1.3.2 Source loading . . . . .	3
1.3.3 Treatment time . . . . .	4
1.3.4 Dose rate . . . . .	4
1.4 Intensity modulated brachytherapy . . . . .	4
1.5 Search for novel brachytherapy sources . . . . .	5
1.6 Objectives . . . . .	6
<b>2 Radiation Physics and Dosimetry</b>	<b>8</b>
2.1 Dosimetry concepts . . . . .	8
2.1.1 Fluence and flux . . . . .	8
2.1.2 Photon interaction spectrum . . . . .	9
2.1.3 Kerma . . . . .	9
2.1.4 Dose . . . . .	10
2.2 Radiation physics . . . . .	11
2.2.1 Photon interactions . . . . .	11
Rayleigh scattering . . . . .	11
Photoelectric effect . . . . .	11
Compton scattering . . . . .	11
Pair production and triplet production . . . . .	12
Photonuclear reactions . . . . .	12
Relative predominance of interactions . . . . .	13
Production of vacancies in atomic shells . . . . .	13
Photon beam attenuation . . . . .	14
2.2.2 Electron interactions . . . . .	14
Electron-orbital electron interactions . . . . .	14
Electron-nucleus interactions . . . . .	15

	Stopping power . . . . .	15
	Linear energy transfer . . . . .	16
2.3	Brachytherapy dose calculations . . . . .	16
2.4	Monte Carlo methods in radiation therapy . . . . .	19
	2.4.1 Basics of Monte Carlo simulations . . . . .	19
	2.4.2 Geant4 and Geant4-DNA . . . . .	20
<b>3</b>	<b>Radiobiology</b>	<b>21</b>
	3.1 Direct and indirect effects of ionizing radiation . . . . .	21
	3.2 Relative biological effectiveness . . . . .	22
	3.3 Linear-quadratic model . . . . .	23
<b>4</b>	<b>Microdosimetry</b>	<b>26</b>
	4.1 Application of microdosimetry to radiation quality . . . . .	26
	4.2 Microdosimetric quantities and parameters . . . . .	27
	4.3 Experimental microdosimetry . . . . .	30
	4.4 Simulation of microdosimetric distributions . . . . .	32
	4.5 Overview: Paper 1 . . . . .	33
<b>5</b>	<b>Radionuclide Production</b>	<b>34</b>
	5.1 Radioactivity . . . . .	34
	5.2 Neutron activation . . . . .	35
	5.3 Gamma spectroscopy . . . . .	36
	5.4 Production and encapsulation of brachytherapy sources . . . . .	37
	5.5 Overview: Paper 2 . . . . .	38
<b>6</b>	<b>Brachytherapy Source Characteristics</b>	<b>40</b>
	6.1 Physical characteristics . . . . .	40
	6.2 Dosimetric evaluation . . . . .	41
<b>7</b>	<b>Conclusions</b>	<b>44</b>
	<b>Bibliography</b>	<b>45</b>

# List of Figures

2.1	Regions of relative predominance of the three main forms of photon interaction with matter. The left curve represents the region where the atomic coefficients for the photoelectric effect and Compton effect are equal, the right curve is for the region where the atomic Compton coefficient equals the atomic pair production coefficient. Figure taken from IAEA, 2005. . . . .	13
2.2	Coordinate system used for brachytherapy dosimetry calculations. Figure taken from Rivard et al., 2004. . . . .	17
3.1	Direct and indirect action of radiation in biological systems. Figure taken from Hall and Giaccia, 2012. . . . .	22
3.2	Cell survival curves for sparsely and densely ionizing radiation. Figure taken from Hall and Giaccia, 2012. . . . .	24
6.1	Radial dose function $g_L(r)$ for the hypothetical $^{192}\text{Ir}$ , $^{75}\text{Se}$ , $^{169}\text{Yb}$ , $^{153}\text{Gd}$ and $^{125}\text{I}$ sources simulated in a water phantom with a 40 cm radius. . . .	42
6.2	2D Anisotropy function $g_L(r)$ for the hypothetical $^{192}\text{Ir}$ , $^{169}\text{Yb}$ , and $^{153}\text{Gd}$ sources at radial distance of 1 cm (solid line), 5 cm (dashed line) and 10 cm (dotted line). . . . .	43

# List of Tables

6.1	Physical properties of radionuclides. . . . .	40
-----	---	----

# List of Abbreviations

<b>AAPM</b>	<b>American Association of Physicists in Medicine</b>
<b>BE</b>	<b>Biological Effect</b>
<b>CNSC</b>	<b>Canadian Nuclear Safety Commission</b>
<b>CSDA</b>	<b>Continuous Slowing Down Approximation</b>
<b>DNA</b>	<b>DeoxyriboNucleic Acid</b>
<b>DSB</b>	<b>Double Strand Break</b>
<b>EBRT</b>	<b>External Beam RadioTherapy</b>
<b>ESTRO</b>	<b>European SocieTy for Radiotherapy and Oncology</b>
<b>GEANT4</b>	<b>GEometry ANd Tracking 4</b>
<b>HDR</b>	<b>High Dose Rate</b>
<b>HLLF</b>	<b>High Level Laboratory Facility</b>
<b>HPGe</b>	<b>High Purity Germanium</b>
<b>HPLC</b>	<b>High Pressure Liquid Chromatography</b>
<b>HVL</b>	<b>Half-Value Layer</b>
<b>ICRP</b>	<b>International Commission on Radiological Protection</b>
<b>ICRU</b>	<b>International Commission on Radiation Units and measurements</b>
<b>IMBT</b>	<b>Intensity Modulated BrachyTherapy</b>
<b>IMRT</b>	<b>Intensity Modulated RadioTherapy</b>
<b>ISO</b>	<b>International Standards Organisation</b>
<b>KERMA</b>	<b>Kinetic Energy Released per unit MAAss</b>
<b>KURBUC</b>	<b>Kyushu University and RadioBiology Unit Code</b>
<b>LDR</b>	<b>Low Dose Rate</b>
<b>LET</b>	<b>Linear Energy Transfer</b>
<b>LQ</b>	<b>Linear Quadratic</b>
<b>MC</b>	<b>Monte Carlo</b>
<b>MCDS</b>	<b>Monte Carlo Damage Simulation</b>
<b>MCTS</b>	<b>Monte Carlo Track Structure</b>
<b>MDR</b>	<b>Medium Dose Rate</b>
<b>MLC</b>	<b>Multi-Leaf Collimator</b>
<b>MNR</b>	<b>McMaster Nuclear Reactor</b>
<b>MOCA8B</b>	<b>MOnte CARlo 8B</b>
<b>NAA</b>	<b>Neutron Activation Analysis</b>
<b>ORNL</b>	<b>Oak Ridge National Laboratory</b>
<b>PDR</b>	<b>Pulsed Dose Rate</b>
<b>RBE</b>	<b>Relative Biological Effectiveness</b>
<b>RSBT</b>	<b>Rotating Shield BrachyTherapy</b>
<b>TEPC</b>	<b>Tissue Equivalent Proportional Counter</b>
<b>TG</b>	<b>Task Group</b>
<b>TVL</b>	<b>Tenth Value Layer</b>

# Physical Constants

Avogadro's constant	$N_A = 6.022 \times 10^{23} \text{ mol}^{-1}$
elementary charge	$e = 1.602 \times 10^{-19} \text{ C}$
electron rest mass	$m_e = 9.11 \times 10^{-31} \text{ kg}$
Planck's constant	$h = 6.626 \times 10^{-34} \text{ J s}$
pi	$\pi = 3.1415926$

# List of Symbols

$A$	activity	Bq
$D$	dose	Gy
$\dot{D}$	dose rate	Gy s <sup>-1</sup>
$E$	energy	J
$E$	binding energy	J
$E_K$	kinetic energy	J
$E_{\gamma,avg}$	average photon energy	J
$\bar{E}_{tr}$	mean energy transferred	J
$\bar{E}_{en}$	mean energy imparted	J
$I_{\gamma}$	fractional intensity	
$F$	anisotropy function	
$G_L$	geometry function line source	m <sup>-2</sup>
$K$	kerma	Gy
$\dot{K}$	kerma rate	Gy s <sup>-1</sup>
$\dot{K}_{\delta}$	kerma rate with energy cut-off $\delta$	Gy s <sup>-1</sup>
$N$	number of particles	
$N_0$	initial number of particles	
$N_{hist}$	number of histories	
$Q$	radiation quality factor	
$R$	net count rate	s <sup>-1</sup>
$R_{CSDA}$	CSDA range	m
$S$	surface area	m <sup>2</sup>
$S_K$	air-kerma strength	Gy m <sup>2</sup> s <sup>-1</sup>
$S$	stopping power	J m <sup>-1</sup>
$S_{col}$	collision stopping power	J m <sup>-1</sup>
$S_{rad}$	radiative stopping power	J m <sup>-1</sup>
$V$	volume	m <sup>3</sup>
$W_R$	radiation weighting factor	
$Z$	atomic number	
$a$	cross-sectional area	m <sup>2</sup>
$a$	specific activity	Bq kg <sup>-1</sup>
$d$	diameter	m
$d$	dose per fraction	Gy
$d_1$	single-event dose probability	
$f$	frequency	
$f_1$	single-event frequency probability	
$g_L$	radial dose function line source	
$h$	height	m
$h\nu$	initial photon energy	J
$h\nu'$	scattered photon energy	J

$l$	path length	m
$\bar{l}$	mean chord length	m
$m$	mass	kg
$n$	number of fractions	
$t$	time	s
$t_{1/2}$	half-life	s
$r$	radius	m
$r$	radial distance	m
$r_0$	reference radius	m
$w$	atomic weight	kg mol <sup>-1</sup>
$y$	lineal energy	J m <sup>-1</sup>
$\bar{y}_F$	frequency mean lineal energy	J m <sup>-1</sup>
$\bar{y}_D$	dose mean lineal energy	J m <sup>-1</sup>
$z$	specific energy	Gy
$\bar{z}$	average specific energy	Gy
$\bar{z}_F$	frequency mean specific energy	Gy
$\bar{z}_D$	dose mean specific energy	Gy
$\Gamma_{AKR}$	air-kerma rate constant	Gy m <sup>2</sup> s <sup>-1</sup> Bq <sup>-1</sup>
$\Lambda$	dose rate constant	m <sup>-2</sup>
$\Phi$	fluence	m <sup>-2</sup>
$\Phi_E$	fluence spectrum differential in $E$	m <sup>-2</sup>
$\Phi_{E,int}$	interaction spectrum differential in $E$	m <sup>-2</sup>
$\alpha$	initial slope survival curve	Gy <sup>-1</sup>
$\beta$	final slope survival curve	Gy <sup>-2</sup>
$\varepsilon$	relative photon energy	
$\eta$	detector efficiency	
$\theta$	scattering angle	rad
$\theta$	polar angle	rad
$\theta_0$	reference polar angle	rad
$\lambda$	decay constant	s <sup>-1</sup>
$\mu$	attenuation coefficient	m <sup>-1</sup>
$\mu_{en}$	energy absorption coefficient	m <sup>-1</sup>
$\mu_{tr}$	energy transfer coefficient	m <sup>-1</sup>
$\rho$	density	kg m <sup>-3</sup>
$\sigma$	cross section	m <sup>2</sup>
$\sigma_F^2$	frequency mean statistical variance	
$\sigma_D^2$	dose mean statistical variance	
$\phi$	flux	m <sup>-2</sup> s <sup>-1</sup>
$\phi$	recoil angle	rad
$\omega$	sampling weight	

*Dedicated to the love of my life...*

# Chapter 1

## Background

### 1.1 Cancer

A tumor begins when healthy cells change and grow uncontrollably, forming a mass. A tumor can be malignant (cancerous) or benign. A cancerous tumor can grow and spread, or metastasize, to other parts of the body (WHO, 2014). A benign tumor means the tumor can grow but will not spread. A benign tumor usually can be removed without it causing much harm.

The majority of cancers (90-95% of cases) are due to environmental factors (Anand et al., 2008). The remaining cancers are due to inherited genetics. Common environmental factors that contribute to cancer include tobacco, diet and obesity, infections, radiation, stress, lack of physical activity and environmental pollutants.

The Canadian Cancer Society (CCS, 2016) estimates that 45% of men and 42% of women are expected to develop cancer during their lifetimes. More importantly, 29% of men and 24% of women are expected to die from cancer, making cancer the leading cause of death in Canada. An estimated 200 000 new cases of cancer will occur every year in Canada. Lung, breast, colorectal and prostate cancer are the most common types of cancer in Canada, as they account for over half (51%) of all new cancer cases. The number of newly diagnosed cancer cases in Canada is increasing, but survival rates are also increasing. Due to scientific and technological advances in the last decades, important steps in providing tools for effective and successful cancer treatment have been made. Development of imaging modalities has made it possible to

detect cancer early, accurately diagnose it and improve the definition of target volumes or healthy tissue at risk. Radiation therapy alone or combined with chemotherapy and surgery, is used to treat cancer patients with curative intent, and has also an important role for palliation of symptoms from cancer.

## 1.2 Radiation therapy

Radiation therapy, or radiotherapy, refers to therapy using ionizing radiation, generally as part of cancer treatment to control or kill malignant cells. Radiation therapy may be curative in a number of types of cancer if they are localized to one area of the body. Radiation therapy can be divided into two general categories: external beam radiotherapy (EBRT) and brachytherapy.

EBRT is the most common form of radiation therapy (IAEA, 2005). The patient sits or lies on a couch and a beam of ionizing radiation is directed to the tumour site. EBRT is typically delivered using linear accelerators (linacs). Megavoltage photon and electron beams are by far the most widely used sources for EBRT. The aim of radiation therapy is to give an adequate radiation absorbed dose to the volumes containing malignant cells while minimizing the dose to healthy tissue.

Intensity modulated radiation therapy (IMRT) is an advanced radiotherapy technique used to minimize the amount of normal tissue being irradiated in the treatment field (ICRU, 2010). The intensity modulation is achieved by moving the leaves in the multi-leaf collimator (MLC) during the course of treatment, thereby delivering a radiation field with a non-uniform intensity. Each leaf in the MLC is aligned parallel to the radiation field and can be moved independently to block part of the field. By adjusting the position of the leaves, the radiation field can be matched to the shape of the tumour. IMRT can produce highly conformal dose distributions while limiting normal tissue toxicity. Today, the majority of patients receiving radiation therapy undergo IMRT.

Brachytherapy is a form of radiation therapy that uses radiation sources (most commonly radioactive isotopes) that are permanently or temporarily placed inside or near the tumour, giving a high radiation dose to the target volume while maintaining a low dose to surrounding healthy tissues. Brachytherapy requires the positioning of specialized applicators that are specifically designed for each anatomic site into body cavities and tissues to guide the radiation source to the tumour site.

The physical advantage of brachytherapy treatments compared with EBRT is the improved localized delivery of dose to the target volume of interest since the photons emitted from brachytherapy sources are low energetic, with short interaction distance and deposit most of their energy in the target. However, brachytherapy can only be used in cases where the tumour is well localized and relatively small. In a typical radiotherapy department, about 10-20% of all radiotherapy patients are treated with brachytherapy (IAEA, 2005). Its invasiveness compared to EBRT explains why it is a less frequently performed treatment, but its popularity is rising. Within all brachytherapy procedures, the main tumour sites are: gynaecology, prostate, breast, bronchus and head and neck cancer (Guedea2007). Essential to the success of brachytherapy is an accurate dose calculation and administration.

## 1.3 Conventional brachytherapy<sup>1</sup>

### 1.3.1 Types of brachytherapy implants

Brachytherapy treatments can be classified by the type of implant used. Brachytherapy can be administered by placing radioactive sources into body cavities close to the tumour volume (intracavitary), over the tissue to be treated (surface), in a lumen (intraluminal), or into arteries (intravascular). Sources can also be implanted within the tumour volume (interstitial) or during surgery (intraoperative). In general, the two most common types of brachytherapy treatments are interstitial and intracavitary.

---

<sup>1</sup>The information in this section is based on IAEA, 2005.

### 1.3.2 Source loading

Brachytherapy sources can be loaded through hot loading, where the applicator is preloaded and contains the radioactive sources at the time of placement into the patient or through afterloading, where the applicator is first placed into the region of interest and the radioactive sources are loaded later, either by hand (manual afterloading) or by a machine (remote afterloading). Hot loading is not performed in the clinic for radiation safety of the patient and staff.

### 1.3.3 Treatment time

Brachytherapy treatments can be categorized with respect to the treatment time. Radioactive sources can be implanted permanently or temporarily inside the patient. In a temporary implant, the dose is delivered over a short period of time and is removed afterwards. In a permanent implant, the dose is delivered over the lifetime of the source until it decays completely.

### 1.3.4 Dose rate

Brachytherapy treatments can also be classified based on their dose rates (ICRU, 1985). Low dose rate (LDR) brachytherapy refers to a treatment with the dose rate  $0.4\text{--}2\text{ Gy h}^{-1}$ . This is compatible with conventional manual or automatic afterloading techniques. Medium dose rate (MDR) brachytherapy refers to a dose rate of  $2\text{--}12\text{ Gy h}^{-1}$ . MDR brachytherapy is rarely performed in clinical practice. High dose rate (HDR) brachytherapy refers to a dose rate greater than  $12\text{ Gy h}^{-1}$ . In practice, HDR treatments are given with a substantially higher dose rate than that given by the lower limit of  $12\text{ Gy h}^{-1}$ . The main isotope used in conventional HDR brachytherapy is  $^{192}\text{Ir}$ . This is compatible with remote afterloading technology only, because of the high source activity.

The process of delivering pulsed-dose-rate (PDR) brachytherapy is similar to HDR, but radiation is delivered in short pulses over several hours. The source is left in place

for a number of hours or days. PDR combines the physical advantages of HDR technology (isodose optimization and radiation safety) with the radiobiological advantages of LDR brachytherapy. PDR brachytherapy is administered using a remote afterloader.

## 1.4 Intensity modulated brachytherapy

Normal tissue radiation toxicity is a limiting factor in brachytherapy delivery and can negatively impact the patient's quality of life. Dose escalation in the target area with the goal of improving the local tumor control and cure is limited in many cancer sites treated with conventional brachytherapy due to proximity to radiation sensitive normal tissues, such as urethra for prostate cancer, overlying skin for breast cancer, and salivary gland for head and neck cancer.

Intensity modulated brachytherapy (IMBT), also termed rotating shield brachytherapy (RSBT), is a novel HDR brachytherapy technique delivered through shielded, rotating catheters. IMBT removes the constraint that dose distributions must be radially symmetric about each individual catheter since active incorporation of partially-shielded brachytherapy sources can provide azimuthally anisotropic dose distributions that can be dynamically directed into tumor tissue and away from radiation sensitive healthy tissue, improving the therapeutic ratio. Ebert (Ebert, 2002; Ebert, 2006) claimed that introducing intensity-modulation to brachytherapy would provide a high-accuracy therapy with the potential for significant dose conformity. However, he came to the conclusion that transmission on the shielded side of the source should be less than 10% for a successful IMBT treatment. IMBT has been suggested for applications in interstitial brachytherapy for prostate cancer (Adams et al., 2014) and intracavitary brachytherapy for cervical cancer (Dadhkah et al., 2015).

A major challenge in enabling IMBT for interstitial applications is selecting an appropriate radioisotope and designing a rotating shield system that fits inside applicators with diameters in a range of about 1-2 mm. Brachytherapy can be administered by low-energy ( $E < 50$  keV), intermediate energy ( $50 \text{ keV} < E < 200$  keV) or high-energy

sources ( $E > 200$  keV) (Beaulieu2012). Brachytherapy sources are inserted into a patient's tissue where the space available for applicators is limited. The thickness of the shield must be in the sub-millimeter range to fit inside existing brachytherapy catheters and yet modify the intensity of the source by several half-value layers (HVLs). Sub millimeters of a dense metal can shield photons from the intermediate energy brachytherapy sources while several millimeters are needed to shield from high-energy sources such as  $^{192}\text{Ir}$ .

## 1.5 Search for novel brachytherapy sources

Radionuclides with intermediate energy gamma emissions and a long half-life are attractive candidates for novel brachytherapy sources.  $^{192}\text{Ir}$  ( $t_{1/2} = 72$  days,  $E_{\gamma,avg} = 360$  keV) is a widely used gamma isotope for HDR brachytherapy, but has the disadvantage of emitting high-energy gamma radiation that may cause normal tissue toxicity and beta emissions that are not accounted for in the clinical treatment planning systems. The high-energy gamma radiation from  $^{192}\text{Ir}$  require too large shield thickness, thus  $^{192}\text{Ir}$  is not an optimal source for interstitial IMBT. The emission of relatively high-energy gamma and the beta contamination justifies the search for a lower-energy photon-emitting source with comparable dose distribution and dose rate as  $^{192}\text{Ir}$ , but with longer half-life and less beta contamination. It is believed that a lower-energy photon source will offer radiological and radiobiological advantages over the isotopes currently in use in HDR brachytherapy.

Selenium-75 ( $^{75}\text{Se}$ ,  $t_{1/2} = 118.5$  days,  $E_{\gamma,avg} = 210$  keV) has been used as an alternative to  $^{192}\text{Ir}$  in industrial radiography, due to its softer gamma emission spectrum and significantly longer half-life (Grimm and Kaftal, 1996). Ytterbium-169 ( $^{169}\text{Yb}$ ,  $t_{1/2} = 32.0$  days,  $E_{\gamma,avg} = 93$  keV) has been considered as a new radiation source for brachytherapy applications (Mason et al., 1992; MacPherson and Battista, 1998), but is not currently manufactured. Gadolinium-153 ( $^{153}\text{Gd}$ ,  $t_{1/2} = 240.4$  days,  $E_{\gamma,avg} = 60$  keV) has theoretically been investigated as a brachytherapy source for use in IMBT (Enger, Fisher,

and Flynn, 2013; Adams et al., 2014).  $^{75}\text{Se}$ ,  $^{169}\text{Yb}$  and  $^{153}\text{Gd}$  have photon energy spectra and half-lives that make them excellent candidates for use as radioactive sources in BT.  $^{169}\text{Yb}$  and  $^{153}\text{Gd}$ , in particular, could potentially also provide a means for IMBT delivery.

## 1.6 Objectives

The purpose of this work was to evaluate the potential of the radionuclides  $^{75}\text{Se}$ ,  $^{169}\text{Yb}$  and  $^{153}\text{Gd}$  as novel radiation sources for use in conventional brachytherapy and IMBT. The first goal was to evaluate the dosimetric and radiobiological advantages of these sources through numerical methods. The dose distributions were calculated using Monte Carlo (MC) simulations, and the radiation quality of these potential sources was evaluated through numerical microdosimetric techniques. The second goal was to investigate the production, purification and immobilization techniques for  $^{153}\text{Gd}$  through a series of radiochemistry experiments.

## Chapter 2

# Radiation Physics and Dosimetry

## 2.1 Radiation physics<sup>1</sup>

### 2.1.1 Photon interactions

#### Rayleigh scattering

In Rayleigh (coherent) scattering, the photon interacts with a 'bound' orbital electron and is scattered at a small angle, essentially without losing any of its energy. The Rayleigh atomic cross section is proportional to  $Z^2/(h\nu)^2$ . The importance of Rayleigh scattering compared to other photon interactions is very small.

#### Photoelectric effect

In the photoelectric effect, the photon interacts with a 'tightly bound' orbital electron and is absorbed, while the orbital electron is ejected from the atom as a photoelectron with a kinetic energy  $E_K$  given as:

$$E_K = h\nu - E_B \quad (2.1)$$

where  $h\nu$  is the initial photon energy and  $E_B$  is the binding energy of the electron. The photoelectric atomic cross section is proportional to  $Z^4/(h\nu)^3$ .

---

<sup>1</sup>The information in this section is based on Podgorsak, 2010.

### Compton scattering

In Compton (incoherent) scattering, the photon interacts with an 'free and stationary' orbital electron, transfers part of its energy to a recoil electron, and is scattered at an angle  $\theta$ . The energy of the scattered photon  $h\nu'$  and the kinetic energy of the recoil electron  $E_K$  are given as follows:

$$h\nu' = h\nu \cdot \frac{1}{1 + \varepsilon(1 - \cos\theta)} \quad (2.2)$$

$$E_K = h\nu \cdot \frac{\varepsilon(1 - \cos\theta)}{1 + \varepsilon(1 - \cos\theta)} \quad (2.3)$$

where  $h\nu$  is the initial photon energy,  $\varepsilon = \frac{h\nu}{m_e c^2}$  is the normalized incident photon energy,  $m_e$  is the electron rest mass and  $c$  is the speed of light. The scattering angle  $\theta$  and the recoil angle  $\phi$  are related by:

$$\cot\phi = (1 + \varepsilon) \cdot \tan(\theta/2) \quad (2.4)$$

In general, as the initial photon energy increases, the angular distributions of the scattered photon and recoil electron become more forward peaked. The Compton atomic cross section decreases with increasing energy, and is proportional to  $Z$ .

### Pair production and triplet production

In pair production, the photon interacts with the field of a nucleus, disappears and an electron-positron pair is produced. Pair production has a minimum energy threshold of  $2m_e c^2 = 1.022$  MeV. In triplet production, the photon interacts with the field of an orbital electron, disappears, produces an electron-positron pair and transfers kinetic energy to an orbital electron. Triplet production has a minimum energy threshold of  $4m_e c^2 = 2.044$  MeV. The atomic cross sections for pair and triplet production increase with increasing energy, and are proportional to  $Z^2$ .

Pair production and triplet production are followed by the annihilation of the positron

with a 'free and stationary' electron, producing two annihilation photons, most commonly with energies of  $m_e c^2 = 0.511$  MeV each and emitted at about  $180^\circ$  from each other to satisfy the conservation of momentum and energy.

### **Photonuclear reactions**

Photonuclear reactions occur when a high energy photon is absorbed by the nucleus of an atom, resulting in the emission of a neutron or proton and a transformation of the nucleus into a radioactive reaction product. The reaction has a minimum energy threshold of about 10 MeV for most nuclei. The importance of the photonuclear reaction compared to other photon interactions is very small.

### **Relative predominance of interactions**

The probability of a photon to undergo any one of these interactions depends on the photon energy  $h\nu$  and the atomic number  $Z$  of the medium. The regions of relative predominance of the three main photon interactions are shown in figure 2.1. In general, the photoelectric effect dominates at low photon energies, Compton scattering dominates at intermediate energies, and pair (triplet) production dominates at very high energies. In the case of liquid water ( $Z_{eff} = 7.4$ ), the photoelectric effect dominates for energies below 20 keV, Compton scattering dominates in the 20 keV-10 MeV energy range, and pair production dominates for energies above 10 MeV.

### **Production of vacancies in atomic shells**

In the photoelectric effect, the Compton effect and triplet production, vacancies are produced in the atomic shells through the ejection of orbital electrons. When a core electron is removed, leaving a vacancy, an electron from a higher energy level may fall into the vacancy, resulting in a release of energy. This can either result in the emission of characteristic X-rays or through the ejection of an Auger electron.

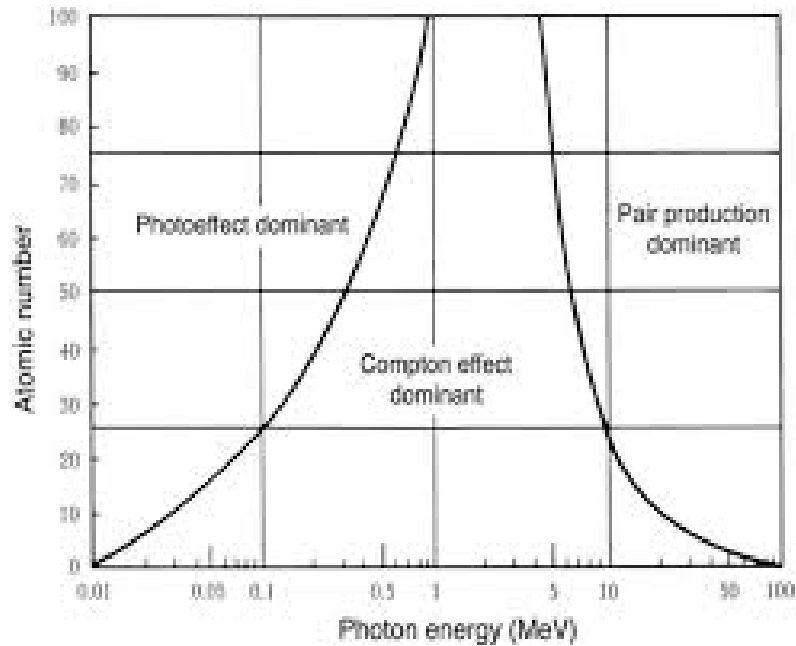


FIGURE 2.1: Regions of relative predominance of the three main forms of photon interaction with matter. The left curve represents the region where the atomic coefficients for the photoelectric effect and Compton effect are equal, the right curve is for the region where the atomic Compton coefficient equals the atomic pair production coefficient. Figure taken from IAEA, 2005.

### Photon beam attenuation

Photon beams are attenuated as they pass through matter, since photons can be absorbed in matter due to interactions such as the photoelectric effect and pair production. The HVL and tenth value layer (TVL) are defined as the thickness of the material that attenuates the photon beam intensity, or air kerma rate, to 50 % and 10% of its maximum value, respectively:

$$\text{HVL} = \frac{\ln 2}{\mu} \quad (2.5)$$

$$\text{TVL} = \frac{\ln 10}{\mu} \quad (2.6)$$

where  $\mu$  is the linear attenuation coefficient, which is dependent on the photon energy  $h\nu$  and the atomic number  $Z$  of the attenuator. The unit of HVL and TVL is cm. One TVL is equivalent to roughly 3.32 HVL.

The energy transfer coefficient  $\mu_{tr}$  at a photon energy  $h\nu$  is related to the linear attenuation  $\mu$  as follows:

$$\mu_{tr} = \mu \frac{\overline{E}_{tr}}{h\nu} \quad (2.7)$$

where  $\overline{E}_{tr}$  is the average energy transferred to charged particles in the attenuator. The energy absorption coefficient  $\mu_{en}$  at the photon energy  $h\nu$  is related to the linear attenuation  $\mu$  as follows:

$$\mu_{en} = \mu \frac{\overline{E}_{en}}{h\nu} \quad (2.8)$$

where  $\overline{E}_{en}$  is the average energy deposited by charged particles in the attenuator.

## 2.1.2 Electron interactions

### Electron-orbital electron interactions

Coulomb interactions between the incident electron and orbital electrons result in ionizations and excitations of the absorber atoms, through soft or hard collisions. Soft collisions occur when the electron interacts with the whole atom and transfers a small amount of energy to orbital electrons. Hard collisions occur when the electron interacts with an orbital electron and transfers a large amount of energy to orbital electrons. Ionization refers to the ejection of an orbital electron, while excitation refers to the transfer of the orbital electron to a higher shell.

### Electron-nucleus interactions

Coulomb interactions between the incident electron and nuclei of the absorber atom result in electron scattering and energy loss of the electron through bremsstrahlung (photon) production. The radiative yield increases with the kinetic energy of the electrons  $E_K$  and the atomic number  $Z$ .

## Stopping power

Stopping power  $S$  is a term used to describe the inelastic energy losses by an electron moving through a medium:

$$S = \frac{dE_K}{dl} \quad (2.9)$$

where  $dE_K$  is the kinetic energy loss per unit path length  $dl$ . The units of stopping power is  $\text{MeV cm}^{-1}$ . The total stopping power is divided into two components: the collision stopping power  $S_{col}$  and the radiative stopping power  $S_{rad}$ . The collision stopping power  $S_{col}$  is the part of stopping power that results from electron-orbital electron interactions. The radiative stopping power  $S_{rad}$  is the part of stopping power that results from electron-nucleus interactions.

Stopping powers can be used to calculate the electron range  $R$ , calculated in the continuous slowing down approximation (CSDA), as follows:

$$R_{CSDA} = \int_0^{E_{K_i}} \frac{1}{(S/\rho)} dE_K \quad (2.10)$$

where  $E_{K_i}$  is the initial kinetic energy of the electron. The unit of range is cm. The CSDA range is a very close approximation to the average path length travelled by a charged particle as it slows down to rest. This definition neglects energy loss fluctuations along the track, energy loss straggling, and scattering. The CSDA range represents an upper limit on the actual range that a charged particle can travel.

The restricted collision stopping power  $L_\Delta$  is given by:

$$L_\Delta = \frac{dE_\Delta}{dl} \quad (2.11)$$

where  $dE_\Delta$  is the energy lost by a charged particle due to soft and hard collisions in traversing a distance  $dl$  minus the total kinetic energy of the charged particles released with kinetic energies in excess of  $\Delta$ . The restricted stopping power excludes secondary electrons (delta-rays) with energies larger than a threshold value  $\Delta$  and that carry energy far from the primary track.

## Linear energy transfer

The linear energy transfer (LET) describes the average energy an ionizing particle transfers to the medium per unit distance. The unit of LET is keV  $\mu\text{m}^{-1}$ . LET depends on the nature of the radiation as well as on the materials transversed. In general, as the kinetic energy decreases, LET increases. LET is closely related to stopping power, however total stopping power has the nuclear stopping power component that is not contained in LET, since it does not result in electronic excitations. LET helps explain why some radiation is more effective than other radiation at producing biological damage for the same absorbed dose.

## 2.2 Dosimetry concepts

### 2.2.1 Fluence and flux

The particle fluence  $\Phi$  is defined as:

$$\Phi = \frac{dN}{dA} \quad (2.12)$$

where  $dN$  represent the number of particles incident on a sphere of cross-sectional area  $dA$  (ICRU, 2011). The SI unit for particle fluence is  $\text{m}^{-2}$ . This quantity is defined for monoenergetic beams. However, realistic photon and particle beams are almost always polyenergetic. For polyenergetic beams, the particle fluence spectrum replaces the particle fluence:

$$\Phi_E(E) = \frac{d\Phi}{dE}(E) \quad (2.13)$$

where  $\Phi_E(E)$  is the particle fluence spectrum differential in energy  $E$ .

The flux  $\phi$ , or particle fluence rate, is the quotient of the particle fluence  $d\Phi$  by the increment of time  $dt$ :

$$\phi = \frac{d\Phi}{dt} \quad (2.14)$$

The SI unit for flux is  $\text{m}^{-2} \text{s}^{-1}$ . Note that fluence (and flux) are defined at a point, however any measurement or simulation scores these quantities in a finite volume  $V$ . The definition of fluence is equivalent to a second, more general, definition based on path lengths (Papiez and Battista, 1994), which is useful when running MC simulations. The fluence can be defined as the quotient of  $l$  by  $V$  where  $l$  is the average total length of particle track segments contained within a finite volume  $V$ . This definition allows the calculation of fluence in macroscopic volumes, and does not assume that particle tracks inside the sampling volume are straight lines.

### 2.2.2 Photon interaction spectrum

The photon interaction spectrum, a quantity described in section 2 of paper 1, shows the energy distribution of the photons that interact in a finite volume  $V$  and transfer their energy to secondary charged particles, in this case, electrons:

$$\Phi_{E,int}(E) = \frac{d\Phi_{int}}{dE}(E) \quad (2.15)$$

where  $\Phi_{E,int}(E)$  is the photon interaction spectrum differential in energy  $E$ .

### 2.2.3 Kerma

Kerma is an acronym for "kinetic energy released per unit mass". It quantifies the average amount of energy transferred from indirectly ionizing radiation (such as photons and neutrons) to directly ionizing radiation (such as electrons, protons, and heavy ions):

$$K = \frac{d\bar{E}_{tr}}{dm} \quad (2.16)$$

where  $d\bar{E}_{tr}$  is the mean energy transferred from the indirectly ionizing radiation to charged particles in the medium per unit mass  $dm$  in a finite volume  $V$  (ICRU, 2011). Note that this quantity only takes into account the energy transferred, not the energy absorbed. The SI unit of kerma is Gy.

The total kerma is divided into two components: the collision kerma  $K_{col}$  and the radiative kerma  $K_{rad}$ . The collision kerma  $K_{col}$  is the part of kerma that leads to the production of secondary charged particles that dissipate their energy as ionization in or near the particle tracks in the medium. The radiative kerma  $K_{rad}$  is the part of kerma that leads to the production of radiative photons as the secondary charged particles slow down and interact in the medium. The average fraction of the energy transferred to secondary charged particles that is lost through radiative processes is represented by the radiative fraction  $\bar{g}$ . A frequently used relation between collision kerma  $K_{col}$  and total kerma  $K$  is written as follows:

$$K_{col} = K(1 - \bar{g}) \quad (2.17)$$

The kerma rate  $\dot{K}$  is the quotient of the kerma  $dK$  by the increment of time  $dt$ :

$$\dot{K} = \frac{dK}{dt} \quad (2.18)$$

The SI unit of kerma rate is  $\text{Gy s}^{-1}$ .

## 2.2.4 Dose

The absorbed dose  $D$  is defined as the mean energy imparted  $d\bar{E}_{en}$  by ionizing radiation per unit mass  $dm$  in a finite volume  $V$ :

$$D = \frac{d\bar{E}_{en}}{dm} \quad (2.19)$$

The energy imparted is the sum of all energy entering the volume minus all the energy leaving the volume (ICRU, 2011). The SI unit of absorbed dose is Gy. This quantity is applicable to both directly ionizing (electrons, protons, heavy ions) and indirectly ionizing (photons, neutrons) radiation. For indirectly ionizing radiation, energy is deposited by transferring energy to secondary charged particles, which then transfer their energy to the medium. Note that because secondary charged particles travel

in the medium and deposit energy along their tracks, this absorption of energy does not necessarily take place at the same location as the transfer of energy described by kerma. In the case where low energy photons react through the photoelectric effect and release photoelectrons that do not travel far and deposit their energy locally, then dose is essentially equal to collision kerma.

The absorbed dose  $D$  in a uniform medium of density  $\rho$  can be represented using the spectrum-averaged mass collisional stopping power ( $\bar{S}_{col}/\rho$ ):

$$D = \Phi \left( \frac{\bar{S}_{col}}{\rho} \right) \quad (2.20)$$

where  $\Phi$  represents the electron fluence.

The dose rate  $\dot{D}$  is the quotient of the dose  $dD$  by the increment of time  $dt$ :

$$\dot{D} = \frac{dD}{dt} \quad (2.21)$$

The SI unit of dose rate is  $\text{Gy s}^{-1}$ .

## 2.3 Brachytherapy dose calculations

Brachytherapy dose calculations are based on the American Association of Physicists in Medicine (AAPM) Task Group No. 43 (TG-43) protocol (Nath et al., 1995; Rivard et al., 2004). The protocol uses a combination of air-kerma rate measurements, performed in the clinic, and published datasets in the reports for existing source models, to calculate 2D dose distributions in water. The general 2D dose rate equation described by the TG-43 formalism is given as:

$$\dot{D}(r, \theta) = S_K \cdot \Lambda \cdot \frac{G_L(r, \theta)}{G_L(r_0, \theta_0)} \cdot g_L(r) \cdot F(r, \theta) \quad (2.22)$$

where  $r$  denotes the distance from the center of the active source to the point of interest,  $r_0$  denotes the reference distance (1 cm),  $\theta$  denotes the polar angle of the point

of interest relative to the source longitudinal axis, and  $\theta_0$  denotes the reference angle ( $90^\circ$ ). The coordinate system is shown in figure 2.2. The parameters introduced by the formalism will be described below.

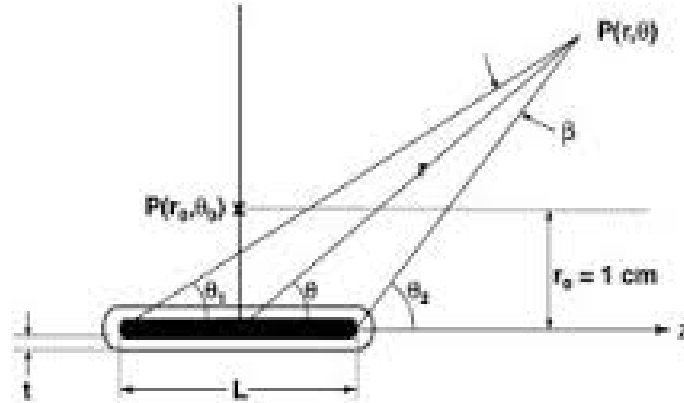


FIGURE 2.2: Coordinate system used for brachytherapy dosimetry calculations. Figure taken from Rivard et al., 2004.

The air-kerma strength  $S_K$  is the air-kerma rate  $\dot{K}_\delta(d)$  *in vacuo* at a distance  $d$  due to photons of energy greater than  $\delta$  multiplied by the square of the distance:

$$S_K = \dot{K}_\delta(d) \cdot d^2 \quad (2.23)$$

The unit of air-kerma strength is  $U = \text{cGy cm}^2 \text{ h}^{-1}$ . The air-kerma rate measurements are typically performed at 1 m from the source center, ensuring the distance is large compared to the linear dimensions of the source and detector. The energy cut-off  $\delta$  is intended to exclude low-energy photons that increase the air-kerma rate, but do not contribute significantly to dose at distances greater than 1 mm in water. The value is typically 5 keV for low-energy brachytherapy sources.

The dose rate constant  $\Lambda$  is the ratio of the dose rate at the reference position  $\dot{D}(r_0, \theta_0)$  and the air-kerma strength  $S_K$ :

$$\Lambda = \frac{\dot{D}(r_0, \theta_0)}{S_K} \quad (2.24)$$

The unit of the dose rate constant is  $\text{Gy s}^{-1} \text{ U}^{-1}$ . The dose rate constant essentially converts a kerma rate in air to a dose rate in water, and is dependent on the source

isotope and model.

The geometry function  $G_L(r, \theta)$  provides an approximate estimate of the dose rate variation as a function of position based on a line source approximation of the distribution of radioactivity within the source:

$$G_L(r, \theta) = \begin{cases} \frac{\beta}{Lr \sin \theta} & \text{if } \theta \neq 0^\circ \\ \frac{1}{r^2 - L^2/4} & \text{if } \theta = 0^\circ \end{cases}$$

where  $L$  is the active length of the source and  $\beta = 2\arctan(l/2r)$  is the angle subtended by the tips of the line source with respect to the point of interest. The unit of the geometry function is  $\text{cm}^{-2}$ . The geometry function neglects the effects of scattering and attenuation. It is independent of the source isotope and model (only the active length is required).

The radial dose function  $g_L(r)$  accounts for dose fall-off on the transverse plane due to photon scattering and attenuation, in addition to the fall-off predicted by the geometry function:

$$g_L(r) = \frac{\dot{D}(r, \theta_0)}{\dot{D}(r_0, \theta_0)} \cdot \frac{G_L(r_0, \theta_0)}{G_L(r, \theta_0)} \quad (2.25)$$

The radial dose function is equal to unity at the reference distance  $r_0$  (1 cm).

The 2D anisotropy function  $F(r, \theta)$  describes the variation in dose rate as a function of polar angle  $\theta$  and distance  $r$  due to photon scattering and attenuation, in addition to the fall-off predicted by the geometry function:

$$F(r, \theta) = \frac{\dot{D}(r, \theta)}{\dot{D}(r, \theta_0)} \cdot \frac{G_L(r, \theta_0)}{G_L(r, \theta)} \quad (2.26)$$

The 2D anisotropy function is equal to unity at the reference angle  $\theta_0$  ( $90^\circ$ ).  $F(r, \theta)$  is generally displayed as a function of  $\theta$  for various depths  $r$ .

## 2.4 Monte Carlo methods in radiation therapy

### 2.4.1 Basics of Monte Carlo simulations

The transport of particles in matter can be solved in an exact manner by the MC method (Andreo, 1991). Particles are generated according to the source energy and angular distributions, they travel a certain distance (determined by a probability distribution) to the site of a collision and scatter into another direction, deposit energy and/or release secondary particles. This procedure is continued until the particle is absorbed or leaves the geometry under consideration. The principles of a general purpose MC code for particle transport can be described as a three step process, each step requiring a random number generator to sample from a probability distribution. First, the step length of the particle is determined by sampling of the total interaction cross-section, and the particle is transported to its new position. Then, the type of interaction event occurring after the step is decided by sampling the relative magnitudes of the individual cross-sections. Finally, the energy and/or direction of the primary and secondary particles (if secondary particles are ejected) are obtained by sampling the angular differential cross-section for the given interaction. Quantities of interest can be calculated by averaging over a given set of particle histories. In general, the statistical uncertainty decreases with the number of histories  $N_{hist}$ , and is inversely proportional to  $\sqrt{N_{hist}}$ .

In general, MC simulations can be quite computationally expensive and can lead to very long computation times. In order to improve the efficiency of the simulation, variance reduction techniques can be performed to allow the user to tune the part of the simulation to the part of the problem space (particle type, energy, position) most relevant to the application. Examples of variance reduction techniques include bremsstrahlung splitting, interaction forcing, range rejection, and Russian roulette.

Electron transport can also lead to problems with regards to computation time. In the process of slowing down, electrons may undergo hundreds of thousands of collisions, for most of which the electrons' directions and energies are only slightly changed. Condensed history techniques (Berger, 1963), which are based on multiple

scattering theory (Goudsmit and Saunderson, 1940), use the fact that individual collisions between electrons and atoms generally have an extremely small effect on an electron's direction and energy. In this method, the physical electron transport is approximated, rather than directly simulated. Groups of individual collisions are approximated by larger, "macro collisions", which describe the cumulative effect of a large number of physical interactions. These techniques reduce the number of simulated collisions, which improve the computational efficiency of the program.

Event-by-event simulations are handled with MC track structure (MCTS) codes. MCTS algorithms simulate the full slowing-down of low-energy charged particles down to a cutoff energy of about 10 eV. The availability of MCTS codes has made it possible to make theoretical investigation of energy deposition patterns down to the nanometre scale in simple environments such as water. MCTS simulations have become an important tool in biophysical modelling of radiation damage in mammalian cells.

#### **2.4.2 Geant4 and Geant4-DNA**

Geant4 (an acronym for "Geometry and tracking 4") is a MC toolkit for simulating the passage of particles through matter (Agostinelli et al., 2003). It includes a complete range of functionality including tracking, geometry, physics models and scoring. The set of physics models include electromagnetic, hadronic and optical processes, for a large variety of particles, materials and elements, over a very wide energy range (from 250 eV to 1 PeV, depending on the particle type). It has been designed to handle the implementation of complex geometry into the system, the materials involved, the generation of primary particles, the physics processes governing particle interaction and production, the storage of events and tracks, the scoring of sensitive detector components, and the visualisation of the geometry and particles track, using object-oriented technology implemented in the C++ programming language. Each component of the simulation is implemented in a separate class, to allow the easy adaptation for optimal use. Application areas include high energy, nuclear, medical, accelerator and space

physics. Geant4 is developed at CERN as an international collaborative project and the software and source code can be downloaded from the Geant4 project website at CERN.

The Geant4 toolkit is continuously being extended with physical, chemical and biological models in order to simulate radiation interaction with matter. The Geant4-DNA (Bernal et al., 2015; Incerti et al., 2010) physics processes and models can simulate event-by-event interactions of particles (photons, electrons, protons, neutrons, heavy ions) in liquid water down to the eV scale. The Geant4-DNA processes simulate explicitly every interaction without relying on condensed history techniques. The electron interaction processes are based on a combination of semi-empirical models and on the plane-wave Born approximation. The Geant4-DNA processes for electrons include elastic scattering (Champion model), electronic excitation and ionisation of the water molecule (Born approximation), dissociative electron attachment (Sanche model), and vibrational excitation of the molecule (Melton model). Photon interactions are based on the Livermore model. By using Geant4-DNA, damage induced by ionizing radiation on the cellular and subcellular scale can be calculated.

# Chapter 3

## Radiobiology

### 3.1 Direct and indirect effects of ionizing radiation

When cells are exposed to ionizing radiation, the standard physical and chemical effects between radiation and the atoms or molecules of the cells occur in a first stage and the possible biological damage to cell functions follows later. The biological effects of radiation result mainly from damage to deoxyribonucleic acid (DNA), which is the primary critical target. However, there are also other sites in the cell that, when damaged, may lead to cell death. When directly ionizing radiation is absorbed in biological material, the damage to the cell may occur through direct and indirect action (IAEA, 2005).

In direct action, the radiation interacts directly with the critical target within the cell. The ionizations and excitations occurring in the target initiate a chain of physical and chemical events that eventually lead to biological damage. Direct action is the dominant process by which high LET particles produce biological damage.

In indirect action, the radiation interacts with other atoms or molecules in the cell (mostly water) to produce free radicals that are able to diffuse far enough to reach and damage critical targets. A free radical is an atom or molecule carrying an unpaired orbital electron in the outer shell (valence electron), and is associated with a high degree of chemical reactivity. When radiation interacts with a water molecule, short-lived free radicals such as  $\text{H}_2\text{O}^+$  (water ion) and  $\text{OH}^\bullet$  (hydroxyl radical) are produced, leading to changes in DNA from breakage of chemical bonds. It is estimated that about

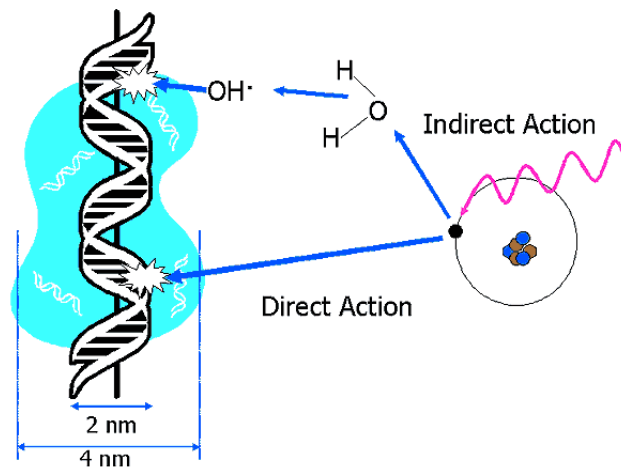


FIGURE 3.1: Direct and indirect action of radiation in biological systems.  
Figure taken from Hall and Giaccia, 2012.

two thirds of the biological damage by low LET radiation to DNA in mammalian cells is caused by the hydroxyl radical. The presence of oxygen enhances the production of reactive oxygen species (peroxides, superoxides, hydroxyl radical, singlet oxygen) in water, leading to a greater amount of radiation damage. Tumor cells in a normal oxygen environment can be as much as 3 times more sensitive to radiation damage than those in a hypoxic environment. Unlike direct action, this component of radiation damage is most easily modified by chemical protectors or sensitizers.

Radiation induces a large number of lesions in DNA, most of which are repaired successfully by the cell. If cells are irradiated with a modest dose of radiation, many single strand breaks (SSBs) occur. A SSB is of little significance as far as cell killing is concerned because it is repaired readily using the opposite strand as a template. If the repair is incorrect, it may result in a mutation. If both strands of the DNA are broken and the breaks are well separated, the breaks are repaired independently. By

contrast, if the breaks in the two strands are opposite one another or separated by only a few base pairs, this may lead to a double-strand break (DSB), resulting in the cleavage of chromatin into two pieces. DSBs are believed to be the most important lesions produced in chromosomes by radiation. The yield in irradiated cells is about 0.04 times that of SSBs, and they are induced linearly with dose, indicating that they are formed by single tracks of ionizing radiation.

## 3.2 Relative biological effectiveness

The relative biological effectiveness (RBE) is a ratio of the doses for two different radiation sources that yield the same biological effect in a given biological system, under identical conditions.

$$\text{RBE} = \frac{D_{\gamma}}{D_X} \quad (3.1)$$

where the subscripts  $\gamma$  and  $X$  represent the reference radiation and the test radiation, respectively (ICRP, 1990). The reference radiation is conventionally  $^{60}\text{Co}$  gamma rays. The biological effect depends on the absorbed dose, but also on several other factors, such as dose rate, fractionation scheme, radiation quality, biological system and biological endpoint. Biological endpoints can include cell death, chromosome aberrations, mutations, induction of double strand breaks (DSBs) and carcinogenic transformations (Hall and Giaccia, 2012).

In general, the RBE increases as a function of LET up to a maximum at around  $100 \text{ keV } \mu\text{m}^{-1}$ . It is believed that this peak in efficiency is reached when the clustering of energy deposition events matches the average interstrand distance (2 nm) in the DNA molecule. At higher LET values, more energy is deposited between the strands without an increase in biological damage.

In dosimetry, the RBE is represented by the radiation weighting factor  $W_R$  (ICRP, 2003), previously defined as quality factor  $Q$  (ICRP, 1990). The weighting factor for a given radiation quality converts an absorbed dose into a biological equivalent dose.

### 3.3 Linear-quadratic model<sup>1</sup>

A cell survival curve describes the relationship between the surviving fraction of irradiated cells and the absorbed dose. The linear-quadratic (LQ) model assumes that there are two components to cell killing by radiation, one that is proportional to dose ( $\alpha D$ ) and one that is proportional to the square of the dose ( $\beta D^2$ ). The expression for the cell survival curve is:

$$SF(D) = e^{-\alpha D - \beta D^2} \quad (3.2)$$

where SF is the surviving fraction at a given dose  $D$ ,  $\alpha$  is the initial slope of the cell survival curve and  $\beta$  is the quadratic component of the cell survival curve. The  $(\alpha/\beta)$  ratio gives the dose at which the linear and quadratic components of cell killing are equal. The LQ formalism describes a biophysical model of cell killing, where  $\alpha$  depends both on the biological endpoint and the radiation quality, while  $\beta$  only depends on the endpoint.

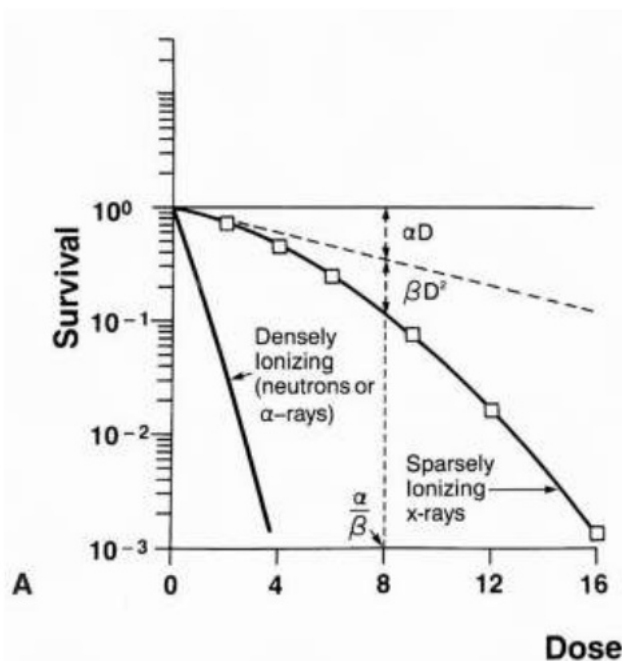


FIGURE 3.2: Cell survival curves for sparsely and densely ionizing radiation. Figure taken from Hall and Giaccia, 2012.

<sup>1</sup>The information in this section is based on Hall and Giaccia, 2012.

An organ or tissue expresses response to radiation damage either as an early (acute) effect or as a late (chronic) effect. The cell survival curves for late responding tissues are more curved than those for early responding tissues. For early effects, the  $(\alpha/\beta)$  ratio is large and  $\alpha$  dominates at low doses. For late effects,  $(\alpha/\beta)$  is small and  $\beta$  has an influence at doses lower than for early responding tissues. The  $\alpha$  and  $\beta$  components of mammalian cell killing are equal at approximately  $(\alpha/\beta) = 10$  Gy and  $(\alpha/\beta) = 3$  Gy for early and late effects, respectively.

For a single acute dose  $D$ , the biological effect (BE) is given by:

$$\text{BE} = \alpha D + \beta D^2 \quad (3.3)$$

However, radiation therapy is typically delivered in several, smaller doses over a period of several days. When the total radiation dose  $D$  is divided into  $n$  well-separated fractions of dose  $d$ , there is enough time to allow full repair of sublethal lesions between the fractions. In the case of fractionated radiotherapy, the shoulder of the survival curve has to be repeated many times and, as a result, the effective dose-response relationship is closer to an exponential function of dose and the quadratic component of cell killing is reduced. The biological effect for fractionated radiotherapy is given by:

$$\text{BE} = n(\alpha d + \beta d^2) = \alpha D \left( 1 + \frac{d}{(\alpha/\beta)} \right), \quad (3.4)$$

Fractionated radiotherapy has many benefits. The time interval between radiation fractions preferentially allows normal cells to repair sublethal DNA damage. It allows the repopulation of normal healthy cells, reassortment of tumor cells into more radiosensitive phases of the cell cycle and perfusion of oxygen into hypoxic regions of tumors. Fractionation essentially minimizes normal tissue toxicity (repair, repopulation) while improving the cell killing effect in the tumor (reoxygenation, reassortment).

# Chapter 4

## Microdosimetry

### 4.1 Application of microdosimetry to radiation quality

Ionizing radiation is a source of a variety of biological effects, including cell inactivation, cell death, chromosome aberrations, mutations, induction of DSBs and carcinogenic transformations. The detailed understanding of the mechanisms by which these effects are induced are related to the patterns of energy deposition in microscopic regions or domains. The concept of average absorbed dose to a macroscopic volume (as an approximation of dose to a point) is not sufficient to characterize radiation damage.

Microdosimetry was defined by Rossi and Zaider (Rossi and Zaider, 1995) as "the systematic study and quantification of the spatial and temporal distribution of absorbed energy in irradiated matter". Microdosimetry is the theoretical and experimental investigation of the imparted energy probability distributions in a small, "microscopic" volume of matter that is crossed by single ionizing particles. Depending on their microdosimetric distributions, the energy required for a given level of biological effect may vary significantly between different radiation qualities. A knowledge of such energy distributions is required to explain the relative effectiveness of different types of radiation. Microdosimetry can be used to identify regions of concentrated ionization clusters, which are crucial for describing the mechanisms of radiation damage.

The distribution of the deposited energy will be related to LET, but will also take into consideration all the related stochastic effects (energy loss straggling, energy transport due to delta rays, variation of LET along the track, finite range of particles, angular

scattering) that are disregarded in the LET concept. (Kellerer, 1985) If the probability of damage in a given domain is related to the energy imparted in the volume, then it might be better described by the microdosimetric distribution for the same object size than by the LET.

Microdosimetry has been used extensively to characterize radiation quality in radiation therapy and radiation protection (Lindborg and Nikjoo, 2011). Systematic microdosimetric measurements are faster and cheaper to perform than radiobiological experiments. The dose mean lineal energy  $\bar{y}_D$ , defined in section 4.2, is a recommended quantity for the evaluation of radiation quality. However, lineal energy distributions can vary significantly with the size and shape of the scoring volumes used. One reason to study energy depositions in variable volume sizes is to see if a match between a measured quantity and some beam quality characteristics can be found for a specific size. It has been determined that the energy deposition patterns to a site with a diameter of around 10 nm can provide insights on the RBE of the radiation in radiotherapy applications (Lindborg et al., 2013), for a variety of endpoints taken from *in vitro* experiments with cell lines and *in vivo* experiments with animals. This has been observed for both low- and high-LET radiation, including photon, proton, neutron and heavy ion therapy beams.

## 4.2 Microdosimetric quantities and parameters

Specific energy  $z$  is defined as:

$$z = \frac{E}{m} \quad (4.1)$$

where  $E$  is the energy imparted to a small volume of mass  $m$  (ICRU, 1983). Specific energy values are typically expressed in units of Gy. In microscopic dimensions, where the fluctuation in energy deposition becomes of increasing importance, specific energy is the appropriate description of energy deposition instead of average absorbed

dose. The specific energy varies with the absorbed dose  $D$  and is defined for multiple events. An event essentially consists of an individual interaction of a charged particle track with a target volume. An event denotes the interaction of statistically correlated particles, including secondary particles. By definition, an event requires an energy deposition; the passage of a charged particle without energy transfer to the site is therefore not counted as an event. In a multiple-event spectrum, there are several events that contribute to the energy imparted. Both the number of events and the energy imparted in each event are described by Poisson statistics. The mean specific energy  $\bar{z}$  is the microdosimetric equivalent of absorbed dose:

$$\bar{z} = \int_0^{\infty} z f(z, D) dz \quad (4.2)$$

where  $f(z, D)$  represents the frequency distribution of specific energy  $z$  at dose  $D$ . At larger doses, the distribution tends to a normal distribution centered at  $D$ . Note that specific energy distributions can also be defined for single events. The single-event frequency mean and dose mean lineal energy  $\bar{z}_D$  are defined as:

$$\bar{z}_F = \int_0^{\infty} z f_1(z) dz \quad (4.3)$$

$$\bar{z}_D = \int_0^{\infty} z d_1(z) dz = \frac{\int_0^{\infty} z^2 f_1(z) dz}{\int_0^{\infty} z f_1(z) dz} = \frac{\overline{z_F^2}}{\bar{z}_F} \quad (4.4)$$

where  $f_1(z)$  and  $d_1(z)$  represent the normalized frequency and dose distributions of specific energy for single events, respectively. To account for the overlap of multiple tracks in the scoring volumes at large doses, the multiple-track distribution  $f(z, D)$  can be obtained by the convolution of the single-track distributions  $f_1(z)$ . The absolute cumulative frequency distribution  $f(> E)$  for the deposition of an amount of energy greater than  $E$  has conventionally been specified for a single target randomly positioned in a water phantom uniformly irradiated with 1 Gy. Ideally, the frequency of

hits of any size in a target is given by:

$$f(> 0) = \frac{1}{\bar{z}_F}. \quad (4.5)$$

The relative cumulative frequency distribution is denoted  $(f > E)/(f > 0)$  and does not depend on the absorbed dose.

Lineal energy  $y$  is defined for single events only:

$$y = \frac{E}{\bar{l}} \quad (4.6)$$

where  $E$  is the energy imparted in a single event and  $\bar{l}$  is the mean chord length of the object under mean free path ( $\mu$ ) randomness, which means all tracks intersecting the sphere originate uniformly from random points in space and are isotropically distributed (Kellerer, 1985). The mean chord length  $\bar{l}$  is equal to  $\frac{4V}{S}$  for a convex site of volume  $V$  and surface area  $S$ . Lineal energy values are typically expressed in units of keV  $\mu\text{m}^{-1}$ . The single-event frequency mean and dose mean lineal energy,  $\bar{y}_F$  and  $\bar{y}_D$ , are defined as:

$$\bar{y}_F = \int_0^{\infty} y f_1(y) dy \quad (4.7)$$

$$\bar{y}_D = \int_0^{\infty} y d_1(y) dy = \frac{\int_0^{\infty} y^2 f_1(y) dy}{\int_0^{\infty} y f_1(y) dy} = \frac{\overline{y_F^2}}{\bar{y}_F} \quad (4.8)$$

where  $f_1(y)$  and  $d_1(y)$  represent the normalized frequency and dose distributions of lineal energy for single events, respectively. It follows that the dose average is always greater than the frequency average. The single-event frequency and dose distributions are independent of the absorbed dose and are characteristic of the radiation quality itself. Lineal energy distributions are usually displayed by plotting  $y \cdot d_1(y)$  on a linear scale vs  $y$  on a logarithmic scale. In this type of display, equal areas under the curve between two values of  $y$  represent equal amounts of absorbed dose. The variance of

the frequency and dose distributions can be calculated as follows:

$$\sigma_F^2(y) = \overline{y_F^2} - \bar{y}_F^2 = (\bar{y}_D - \bar{y}_F)\bar{y}_F \quad (4.9)$$

$$\sigma_D^2(y) = \left[ \left( \frac{2\bar{y}_F\sigma_F(y)}{\bar{y}_F^2} \right)^2 + \left( \frac{\sigma_F(y)}{\bar{y}_F} \right)^2 \right] \bar{y}_D^2 \quad (4.10)$$

The first term within the bracket in equation 4.10 is determined by a first order approximation of the variance of the square of  $y$  using a Taylor expansion (Benaroya, Han, and Nagurka, 2005), such that:  $\sigma_F^2(y^2) \approx (2\bar{y}_F)^2\sigma_F^2(y)$ . It is known that the variance of the average of independent random variables decreases with the number of events  $n$ . Since the events are independent by definition, the variance in the mean of the single-event spectrum will be inversely proportional to  $n$ .

The fundamental difference between quantities like absorbed dose  $D$  and specific energy  $z$ , or LET and lineal energy  $y$ , is their relation to the stochastic nature of radiation interaction. Absorbed dose and LET are macroscopic quantities defined by average energy depositions, while specific and lineal energy are stochastic quantities described by distributions of energy deposition events.

### 4.3 Experimental microdosimetry

Experimental microdosimetry measures the energy imparted in an event-by-event manner inside a tissue equivalent unit density simulated site diameter of the order of micrometers. The instrument which is widely used for this purpose is the tissue equivalent proportional counter (TEPC). TEPCs were constructed to mimic the elemental composition of biological tissue of microscopic site size with the ability to measure the energy imparted by ionizing radiation events (Waker, 1995). The detector is typically made of tissue equivalent plastic and filled with propane or methane based tissue-equivalent gas. The detector gas is at a very low pressure such that the mass of the gas is approximately that of a cell.

A TEPC collects data as a function of time to measure the dose and estimate the dose equivalent by making spectral measurements of the lineal energy loss of the radiation as it passes through the detector volume. The radiation interaction with the gas will generate a number of ion pairs related to the size of the energy deposition event. Charge produced by ionization in the fill gas is multiplied providing an amplified signal proportional to the energy imparted. With sufficient gain, the energy deposited by individual charged particle tracks can be recorded as a pulse-height single-event spectrum.

Measurements of the energy deposition from single events can be difficult at high dose rates and in pulsed radiation fields due to pile-up of several events. Some of these experimental limitations can be reduced when using the variance-covariance method (Kellerer and Rossi, 1984; Lillhok et al., 2007) in which  $\bar{y}_D$  is determined from the multiple-event energy distribution of specific energy determined in two detectors exposed in the same field. To correct for a beam intensity variation, one can subtract the relative covariance between the two detectors. The purpose of the second detector is to monitor beam variations. The measurements are based on charge measurements during specific time intervals and the method can be used in pulsed beams without pile-up effects.

Although critical targets (DNA, nucleosome, centromere) are on the order of nanometers (Nikjoo and Lindborg, 2010), microdosimetric distributions are typically derived for a 1  $\mu\text{m}$  tissue-equivalent diameter, for which measurements have classically been obtained. In order to describe the mechanisms of radiation damage at the level of these radio-sensitive structures, we need to quantify the energy deposition patterns on these smaller scales. Since measurements of the energy deposition in nanometer sized volumes is very difficult and contain extremely large uncertainties, track structure simulations are the preferred method to calculate quantities of interest in these small volumes.

## 4.4 Simulation of microdosimetric distributions

The net result of a MCTS calculation is a simulated track consisting of the three-dimensional positions of all energy deposition events as well as the amount of energy deposited at each transfer point. The calculation of microdosimetric spectra may be performed with the aid of MC techniques, by simulating radiation events passing through scoring volumes. In experimental microdosimetry, a fixed volume (the proportional counter) is traversed by random tracks and the energy deposited is recorded in an event-by-event manner. However, in track structure simulations, the opposite procedure is adopted, as the sampling volumes are typically randomly overlaid onto the particle tracks, and the energy deposited is then stored.

There are many ways one can obtain microdosimetric distributions in a volume using MCTS simulations. The uniform sampling method consists of completely enclosing the track in a virtual volume, say, a box or a sphere, and then randomly overlaying smaller scoring sites inside the given volume, and recording the energy deposited in each scoring volume. An alternative is to voxelize the virtual volume before superimposing the track (Nikjoo et al., 1991; Incerti et al., 2013). The efficiency of this procedure is generally less than one, since not all the scoring volumes will record a non-zero energy deposition. For instance, for low-LET radiation and  $r < 10$  nm, the efficiency is on the order of 1 % (Rossi and Zaider, 1995). Using this method, as the LET of the particle decreases and the scoring volume decreases, the cost in terms of computation time increases.

A more efficient method is to overlay the scoring volumes within the associated volume of the track. The associated volume of a track is the volume around a track that has a sampling efficiency of exactly one (Rossi and Zaider, 1995). Conceptually, it represents the union of the sampling spheres centered at each transfer point. Any sphere placed with its center in it will be within at most one radius from at least one transfer point. Random sampling can be performed by sampling the interaction points and randomly placing scoring volumes within the radius of the transfer point. Since

the sampling is not performed uniformly in space, each energy deposition event needs to be weighed appropriately. The details of the sampling procedure are described in section 2 of paper 1.

## 4.5 Overview: Paper 1

The purpose of the first study (see Paper 1) was to evaluate the radiation quality of intermediate-energy brachytherapy sources using microdosimetric techniques, and then relate the microdosimetry to a clinical RBE or weighting factor  $W_R$  at clinically relevant doses and dose rates for fractionated radiotherapy. It has been claimed that the dose mean lineal energy  $\bar{y}_D$  in a volume of about 10 nm is approximately proportional to the  $\alpha$ -ratio derived from the LQ relation in fractionated radiotherapy for both high- and low-LET radiation. These results were obtained from a combination of MCTS simulations and experiments, and seemed relatively consistent for different types of radiation (photon, electron, neutron, proton, and carbon ion beams).

In this study, we have presented a new methodology to obtain lineal energy distributions using a combination of MCTS simulations using the newly available Geant4-DNA physics processes and an efficient track sampling algorithm based on the associated volume method. The first part of the study showed that the track sampling algorithm adopted in our methodology was equivalent to spatially uniform sampling for a range of monoenergetic electron energies and scoring volumes. The next part of the study showed that the low energy physics models implemented in Geant4-DNA produced consistently lower  $\bar{y}_D$  values for electrons and photon beams than those predicted by older studies. This led to the conclusion that, according to the newer low energy physics models for electrons, the  $\bar{y}_D$ -ratio was approximately equal to the  $\alpha$ -ratio for a volume of about 30 nm instead of 10 nm for low LET radiation.

Based on these findings, the weighting factors predicted were 1.10, 1.14, and 1.19 for  $^{75}\text{Se}$ ,  $^{169}\text{Yb}$ , and  $^{153}\text{Gd}$ , respectively. The intermediate energy sources  $^{75}\text{Se}$ ,  $^{169}\text{Yb}$ , and  $^{153}\text{Gd}$  were up to 15 % more biologically effective than current  $^{192}\text{Ir}$  sources.

# Chapter 5

## Radionuclide Production

### 5.1 Radioactivity<sup>1</sup>

Radioactive decay occurs when a radioactive isotope decays into a stable daughter isotope. The number of radioactive atoms  $N(t)$  as a function of time  $t$  is governed as follows:

$$N(t) = N_0 e^{-\lambda t} \quad (5.1)$$

where  $N_0$  represents the initial quantity of radioactive atoms and  $\lambda$  is the decay constant. The decay constant  $\lambda$  is related to the half-life  $T_{1/2}$  of the radionuclide as follows:

$$\lambda = \frac{\ln 2}{T_{1/2}} \quad (5.2)$$

The activity  $A$  of a radioactive substance at a given time  $t$  is defined as the product of the decay constant  $\lambda$  and the number of radioactive nuclei  $N$ :

$$A(t) = \lambda N(t) = \lambda \frac{m(t)N_A}{w} \quad (5.3)$$

where  $m$  is the mass of the radionuclide,  $N_A$  is Avogadro's constant and  $w$  is the atomic weight of the element. The specific activity  $a$  is the ratio of the activity  $A$  per unit mass

---

<sup>1</sup>The information in this section is based on IAEA, 2005.

$m$  of radioactive nuclide or element (must be specified when quoting):

$$a = \frac{A}{m} \quad (5.4)$$

The practical specific activity is smaller than the theoretical carrier-free specific activity because the source contains stable isotopes in addition to radioactive isotopes.

The specific air kerma rate constant  $\Gamma_{AKR}$  is related to the air kerma rate  $\dot{K}_{air}$ , measured in air, as follows:

$$\Gamma_{AKR} = \frac{\dot{K}_{air}d^2}{A} \quad (5.5)$$

where  $d$  is the distance from the point source with activity  $A$ .

## 5.2 Neutron activation<sup>2</sup>

Neutron activation is the process by which neutron radiation induces radioactivity in materials. It occurs when atomic nuclei capture free neutrons, become heavier and enter excited states. The excited nucleus often decays immediately by emitting nuclear radiations such as gamma rays -  $(n,\gamma)$  reactions - or beta particles -  $(n,\beta^\pm)$  reactions. The process of neutron capture, even after any intermediate decay, often results in the formation of an unstable activation product.

Activation of nuclides occurs when a stable parent isotope P is bombarded with neutrons in a nuclear reactor and transforms into a radioactive daughter D that decays into a granddaughter G. The equation for radionuclide production is given by:

$$\frac{dN_D}{dt}(t) = \phi\sigma_P N_P(t) - \lambda_D N_D(t) \quad (5.6)$$

where  $N_P$  and  $N_D$  represent the number of parent and daughter nuclides at a given time  $t$ , respectively,  $dN_D/dt$  is the rate of change in the number of daughter nuclides at a given time  $t$ ,  $\phi$  is the flux of neutrons in the reactor,  $\sigma_P$  is the activation cross section

<sup>2</sup>The information in this section is based on IAEA, 2005.

of the parent isotope, and  $\lambda_D$  is the decay constant of the daughter radionuclide. This equation can be generalized to any situation by stating that the rate of change in the number of nuclides is equivalent to the sum of the rate of production minus the sum of the rate of loss through radioactive decay and/or neutron activation processes.

The neutron capture cross section  $\sigma$  and neutron flux  $\phi$  used in the production equations are generally specified for thermal neutrons ( $E_K = 0.025$  eV), and exclude higher energy neutrons such as epithermal, resonance, intermediate, and fast neutrons, which are also produced in the nuclear reactor. This approximation is valid because the neutron capture cross section is typically much greater for thermal neutrons than it is for high energy neutrons, with the exception being resonance peaks. In order to avoid discrepancies, it is suggested to estimate production rates in a highly thermalized flux.

### 5.3 Gamma spectroscopy

Gamma spectroscopy is the quantitative study of the energy spectra of gamma-ray sources (Gilmore and Hemingway, 1995). When these emissions are detected and analyzed with a spectrometer, the energy spectrum produced can be used to determine the identity and quantity of gamma emitters present in a gamma source. The equipment used in gamma spectroscopy includes an energy-sensitive radiation detector, electronics to process detector signals produced by the detector, such as a multichannel analyzer, and associated amplifiers and data readout devices to generate, display, and store the spectrum. The most common spectrometer is the high purity Germanium (HPGe) detector, a semiconductor detector.

The count rate  $R$  measured by a detector at a peak energy  $E_\gamma$  is related to the activity  $A$  of the source as follows:

$$R(E_\gamma) = A \cdot \eta(E_\gamma) \cdot I_\gamma(E_\gamma) \quad (5.7)$$

where  $\eta$  is the detector efficiency at energy  $E_\gamma$  and  $I_\gamma$  is the relative intensity of gamma

emission at energy  $E_\gamma$ . The probability that an emitted gamma ray will interact with the detector and produce a count is the efficiency  $\eta$  of the detector. The efficiency of the detector is dependent on the photon energy. In general, larger and wider detectors have higher efficiency than smaller and narrower detectors, although the shielding properties of the detector material are also important factors. Detector efficiency is measured by comparing the count rates in each peak of the spectrum from a source of known activity, to the count rates expected from the known intensities of each gamma ray.

## 5.4 Production and encapsulation of brachytherapy sources

The radioisotope component of a brachytherapy source is generally introduced either in the form of a solid wire, as in the case of  $^{192}\text{Ir}$ , or as a solid substance that has been impregnated with a liquid radioisotope and allowed to dry, as is done for  $^{125}\text{I}$ . The appropriate method depends on the chemical form in which the radioisotope is obtained, and is directly influenced by the production route that is used to generate the radioisotope.

Chemical purification may be required before encapsulation to improve the radionuclidic purity of the source if many impurities are present in the irradiated sample. Generally, if chemical purification is necessary, the radioisotope will be obtained as an aqueous solution, rather than a solid pellet or a wire. One method to immobilize the radioisotope would be to load the solution onto a solid substrate for encapsulation.

Brachytherapy sources are usually sealed so that the radioactive material is contained fully encapsulated within a protective capsule. This capsule is designed to prevent leakage or escape of the radioactive source and it makes the source rigid (ICRP, 2005). Furthermore, for photon emitting sources, the capsule can serve the purpose of absorbing alpha and beta rays produced through the source decay.

## 5.5 Overview: Paper 2

The purpose of the second study (see Paper 2) was to investigate the production, purification and immobilization techniques for  $^{153}\text{Gd}$  through a series of radiation chemistry and radiation physics experiments.

The first goal of the study was to determine the production capacity of  $^{153}\text{Gd}$ . By irradiating samples of enriched  $^{152}\text{Gd}$  at the McMaster Nuclear Reactor (MNR) site, we determined that the effective thermal neutron capture cross section was  $416 \pm 29$  b, which was much lower than that predicted by previous studies. Using this value in numerical simulations, we predicted that the maximum achievable specific activity of  $^{153}\text{Gd}$  was about 70 Ci/g  $^{152}\text{Gd}$ , after about 2-3 months of full-day irradiation, and demonstrated that there would be very little benefit in terms of maximum specific activity from a higher neutron flux. In addition, the amount of impurities produced was also evaluated numerically.

The second goal of the study was to determine the effectiveness of a technique to purify Gd from long-lived Eu impurities. The Eu/Gd separation technique via europium sulfate precipitation through a zinc column was demonstrated to be effective at removing large quantities of Eu from small amounts of Gd. This method can be implemented as a first strike method to remove the bulk of Eu and to equilibrate the concentrations of Gd and Eu in solution for the final processing step, but cannot completely isolate Gd from Eu. The Gd can only be isolated from the remaining rare earths (Eu, Sm) by techniques such as high pressure liquid chromatography (HPLC) or electrodeposition onto a platinum wire.

The third goal of the study was to evaluate a method to immobilize the radioisotope onto a solid substrate for encapsulation. We loaded liquid radioactive Gd onto various sorbents which were claimed to have a high affinity for Gd, and we determined that Dowex®50WX8-400 was the most effective sorbent for loading Gd ( $131 \pm 8$  mg/g sorbent). If  $^{153}\text{Gd}$  will be isolated as an aqueous solution, it can be loaded onto such a sorbent for encapsulation, but this will limit the total activity of the source.

---

This study has provided a production route for potential  $^{153}\text{Gd}$  brachytherapy sources, which could be realistically implemented at the MNR facilities. It has examined the advantages and disadvantages of producing  $^{153}\text{Gd}$  through irradiation of pre-sealed pellets of  $^{152}\text{Gd}$  enriched  $\text{Gd}_2\text{O}_3$ , in terms of production capacity, specific activity, purification methods, and immobilization for encapsulation.

# Chapter 6

## Brachytherapy Source Characteristics

### 6.1 Physical characteristics<sup>1</sup>

The half-life  $T_{1/2}$ , mean photon energy  $E_{\gamma,avg}$ , HVL in lead (Pb), TVL in platinum (Pt), specific air kerma rate constant  $\Gamma_{AKR}$  and means of production of the radioisotopes under investigation in this study are displayed in table 6.1.  $^{75}\text{Se}$ ,  $^{169}\text{Yb}$  and  $^{153}\text{Gd}$  have softer gamma emissions than  $^{192}\text{Ir}$ , thereby reducing the shielding requirements for the room.  $^{75}\text{Se}$  and  $^{153}\text{Gd}$  would have to be replaced fewer times per year compared to the current  $^{192}\text{Ir}$  and  $^{125}\text{I}$  sources.  $^{169}\text{Yb}$  and  $^{153}\text{Gd}$  would be suitable for interstitial IMBT using a Pt-based shield, since the shield thickness that could be fit inside an applicator of 1-2 mm would be large enough to decrease the intensity of radiation on the shielded to below 10% compared to the unshielded side. The disadvantage of the new intermediate energy sources compared to  $^{192}\text{Ir}$  is that the air kerma rate is much lower per unit activity, suggesting a higher activity source may be required to maintain a similar dose rate.

Radionuclide	$^{60}\text{Co}$	$^{192}\text{Ir}$	$^{75}\text{Se}$	$^{169}\text{Yb}$	$^{153}\text{Gd}$	$^{125}\text{I}$
$T_{1/2}$ (days)	5.27 (y)	73.8	118.5	32.0	240.4	59.4
$E_{\gamma,avg}$ (keV)	1250	360	210	93	60	28
HVL (mm Pb)	11	4.8	1.2	0.3	0.25	0.06
TVL (mm Pt)		9	4	0.8	0.37	0.2
$\Gamma_{AKR}$ ( $\mu\text{Gy m}^{-2}\text{GBq}^{-1}\text{h}^{-1}$ )	309	109.1	48.2	21.8	8.7	37.7
Means of production	$^{59}\text{Co}(n,\gamma)$	$^{191}\text{Ir}(n,\gamma)$	$^{74}\text{Se}(n,\gamma)$	$^{168}\text{Yb}(n,\gamma)$	$^{152}\text{Gd}(n,\gamma)$	$^{124}\text{Xe}(n,\gamma)$

TABLE 6.1: Physical properties of radionuclides.

<sup>1</sup>The information in this section is based on IAEA, 2005.

The radioisotopes under investigation can all be produced by neutron irradiation in a nuclear reactor.  $^{153}\text{Gd}$  can be produced either by the activation of  $^{152}\text{Gd}$  (direct production route) or by the activation of  $^{151}\text{Eu}$  (indirect production route). In the indirect production route,  $^{151}\text{Eu}$  undergoes one neutron capture event to form  $^{152}\text{Eu}$ , decays to  $^{152}\text{Gd}$ , and then undergoes a second neutron capture event to produce  $^{153}\text{Gd}$ . In the production of  $^{125}\text{I}$ ,  $^{124}\text{Xe}$  undergoes neutron capture to form  $^{125\text{m}}\text{Xe}$  and  $^{125\text{g}}\text{Xe}$ , which then decay to produce  $^{125}\text{I}$ .

## 6.2 Dosimetric evaluation

Calculations were performed with the MC toolkit Geant4 to simulate the dose distributions of hypothetical brachytherapy sources. The source geometry was modelled as a MicroSelectron-V2 source (Daskalov, Loffler, and Williamson, 1998), which consists of a long of a 3.6 mm long active core with a diameter of 0.65 mm enclosed in 0.9 mm diameter stainless steel capsule, with a 5 mm source guide. The active core of the source was one of  $^{192}\text{Ir}$ ,  $^{75}\text{Se}$ ,  $^{169}\text{Yb}$ ,  $^{153}\text{Gd}$ , or  $^{125}\text{I}$ . The source was placed in the center of a spherical water phantom with a 40 cm radius. The phantom was parameterised into shells with a radial thickness of 1 mm and a polar angle variation of  $5^\circ$ . The radioactive decay for brachytherapy sources was simulated using the radioactive decay physics lists. Photons were tracked using the standard Livermore physics list, with a production cut-off of 250 eV. At least  $10^7$  histories were simulated for each source to ensure good statistics of the dose distributions.

Figure 6.1 shows the radial dose function  $g_L(r)$  for the hypothetical  $^{192}\text{Ir}$ ,  $^{75}\text{Se}$ ,  $^{169}\text{Yb}$ ,  $^{153}\text{Gd}$  and  $^{125}\text{I}$  sources simulated in a water phantom with a 40 cm radius. For a high-energy source such as  $^{192}\text{Ir}$ , the radial dose function is near unity close to the source, and decreases slowly with further depth. The competing effects of both attenuation and scatter are roughly equivalent close to the source, while attenuation starts to dominate far away from the source.

For intermediate-energy sources, the Compton effect is dominant. At distances close to the source, attenuation in tissue is overcompensated by multiple scatter build-up from low-energy photons. In addition, the dose fall-off beyond 10 cm is greater as the energy decreases, which reduces the amount of dose given to healthy tissues far from the target.

For a low-energy source, on the other hand, the photoelectric effect (and therefore attenuation) dominates, leading to a radial dose function that decreases rapidly with distance. While this reduces the amount of normal tissue toxicity, this source can only be used to treat over small distances.

Overall, the intermediate-energy sources have radial dose functions that are better suited for brachytherapy applications than those of both  $^{192}\text{Ir}$  and  $^{125}\text{I}$ .

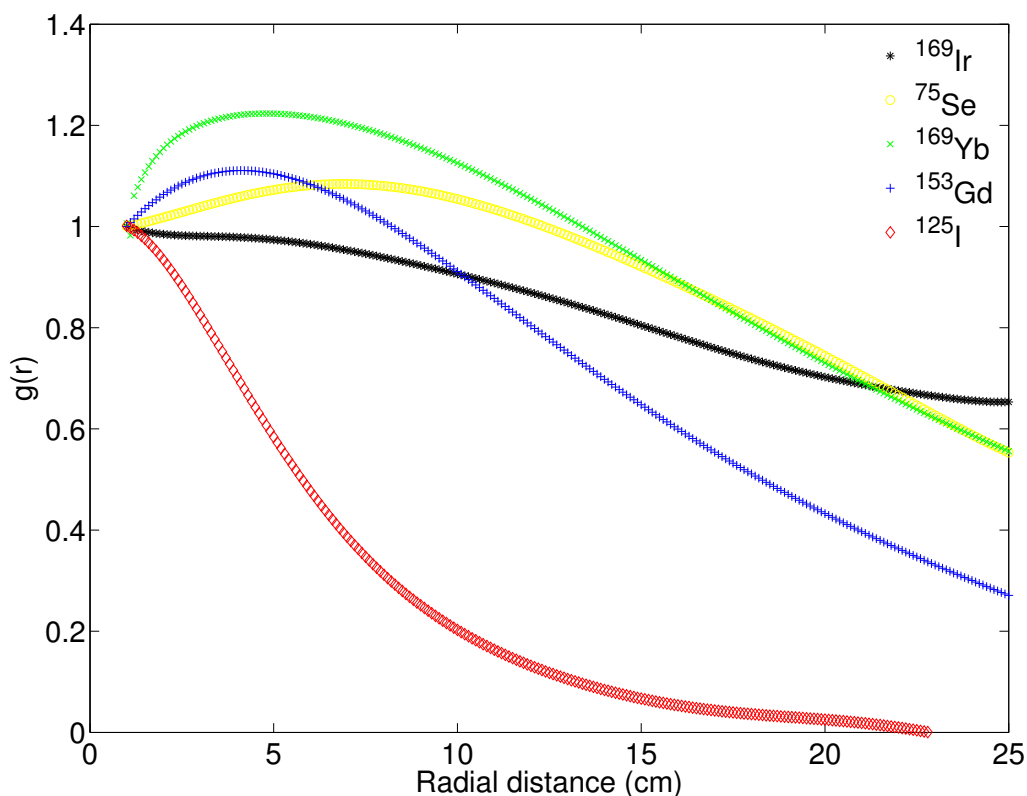


FIGURE 6.1: Radial dose function  $g_L(r)$  for the hypothetical  $^{192}\text{Ir}$ ,  $^{75}\text{Se}$ ,  $^{169}\text{Yb}$ ,  $^{153}\text{Gd}$  and  $^{125}\text{I}$  sources simulated in a water phantom with a 40 cm radius.

Figure 6.2 shows the 2D anisotropy function  $F(r, \theta)$  for the hypothetical sources. In general, the anisotropy function increases with increasing distance from the source. The anisotropy is greater for  $^{153}\text{Gd}$  than for higher energy sources, due to increased absorption of low energy photons in the distal end of the capsule. This is an advantage for shielded brachytherapy, where the dose needs to be directed in a specific direction only (specified by polar and azimuthal angles).

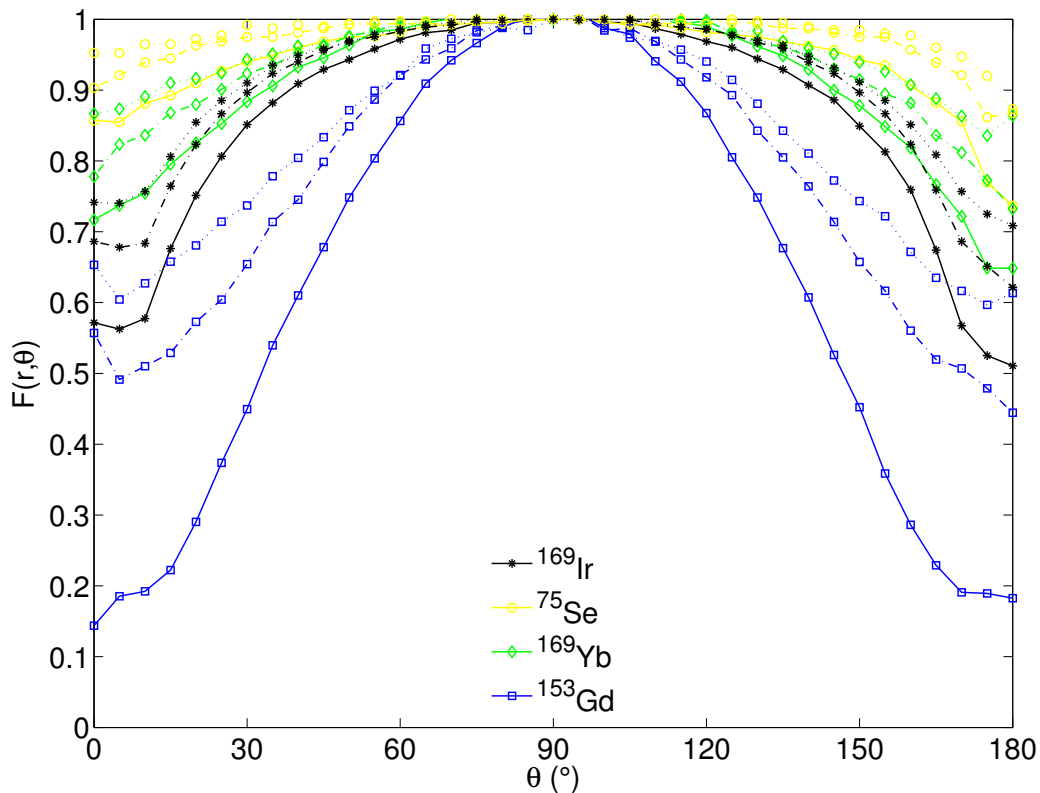


FIGURE 6.2: 2D Anisotropy function  $g_L(r)$  for the hypothetical  $^{192}\text{Ir}$ ,  $^{169}\text{Yb}$ , and  $^{153}\text{Gd}$  sources at radial distance of 1 cm (solid line), 5 cm (dashed line) and 10 cm (dotted line).

Intermediate-energy sources may be superior in terms of both the dose distributions and the lower shielding requirements for conventional HDR brachytherapy and IMBT. In particular,  $^{153}\text{Gd}$  seems to be the most suitable source in terms of its dosimetric advantages.

# Chapter 7

## Conclusions

In this work, we have demonstrated that intermediate-energy brachytherapy sources present various dosimetric, microdosimetric, and radiobiological advantages over sources currently used in HDR brachytherapy, while reducing shielding requirements for the brachytherapy suite. Such sources can potentially be used in combination with a rotating shield delivery system to enable IMBT.

We have predicted clinical weighting factors for  $^{75}\text{Se}$ ,  $^{169}\text{Yb}$  and  $^{153}\text{Gd}$ , which are considerably above unity and should therefore be taken into account during treatment planning. We have investigated the production, purification and immobilization techniques for  $^{153}\text{Gd}$  brachytherapy sources, and have evaluated the viability of such a source for HDR brachytherapy. Finally, we have demonstrated that intermediate-energy sources produce dose distributions that are ideal for HDR brachytherapy applications, better than high-energy sources such as  $^{192}\text{Ir}$  and low-energy sources such as  $^{125}\text{I}$ .

Future studies will focus on the introduction of the first IMBT delivery system using  $^{153}\text{Gd}$  and  $^{169}\text{Yb}$  as radioactive sources; the development of a means of production and encapsulation of  $^{153}\text{Gd}$  and  $^{169}\text{Yb}$  sources at the MNR site; the development of a Geant4-based dose calculation engine for optimization and validation of the source, encapsulation and applicator design; the measurement and simulation of dose distributions from shielded sources/catheters in water phantoms; and the evaluation of the potential for IMBT for various cancer sites commonly treated with brachytherapy.

# Bibliography

- Adams, Q E et al. (2014). "Interstitial rotating shield brachytherapy for prostate cancer". In: *Med. Phys.* 41.5, p. 051703.
- Agostinelli, S et al. (2003). "Geant4 - a simulation toolkit". In: *Nucl. Inst. and Meth. in Phys. Research* 506.3, pp. 250–303.
- Anand, P et al. (2008). "Cancer is a preventable disease that requires major lifestyle changes". In: *Pharm. Res.* 25.9, pp. 2097–116.
- Andreo, P (1991). "Monte Carlo techniques in medical radiation physics". In: *Phy. Med. Biol.* 36.7, pp. 861–920.
- Benaroya, H, S M Han, and M Nagurka (2005). "Probability models in engineering and science". In: *CRC press*.
- Berger, M J (1963). *Monte Carlo calculations of the penetration and diffusion of fast charged particles*. Ed. by M Rotenberg B Alder S Fernbach. Vol. 1. New York: Academic Press, p. 135.
- Bernal, M A et al. (2015). "Track structure modeling in liquid water: a review of the Geant4-DNA very low energy extension of the Geant4 Monte Carlo simulation toolkit". In: *Phys. Med.* 31, pp. 861–74.
- CCS (2016). *Canadian Cancer statistics at a glance*. Retrieved 10 August 2016.
- Dadhkah, M A et al. (2015). "Multihelix rotating shield brachytherapy for cervical cancer". In: *Med. Phys.* 42.11, pp. 6579–88.
- Daskalov, G M, E Loffler, and W F Williamson (1998). "Monte Carlo-aided dosimetry of a new high dose-rate brachytherapy source". In: *Med. Phys.* 25, pp. 2200–8.
- Ebert, M A (2002). "Possibilities for intensity-modulated brachytherapy: technical limitations on the use of non-isotropic sources". In: *Phys. Med. Biol.* 47, pp. 2459–509.

- (2006). “Potential dose-conformity advantages with multi-source intensity-modulated brachytherapy (IMBT)”. In: *Australas. Phys. Eng. Sc. Med.* 29.2, pp. 165–71.
- Enger, S A, D R Fisher, and R T Flynn (2013). “Gadolinium-153 as a brachytherapy source”. In: *Phys. Med. Biol.* 58.4, pp. 957–64.
- Gilmore, G and J Hemingway (1995). *Practical gamma-ray spectrometry*. Chichester: John Wiley & Sons.
- Goudsmit, S A and J L Saunderson (1940). In: *Phys. Rev.* 57, p. 24.
- Grimm, R and T Kaftal (1996). “Gamma radiography using selenium-75”. In: *Insight* 38.9.
- Hall, E J and A J Giaccia (2012). *Radiobiology for the radiologist*. 7th ed. Philadelphia: Lippincott Williams & Wilkins.
- IAEA (2005). *Radiation oncology physics: a handbook for teachers and students*. Ed. by E B Podgorsak. Vienna, Austria.
- ICRP (1990). “RBE for deterministic effects. ICRP publication 58”. In: *Ann. ICRP* 20.4.
- (2003). “Relative biological effectiveness (RBE), quality factor (Q), and radiation weighting factor ( $W_R$ ). ICRP publication 92”. In: *Ann. ICRP* 33.4.
- (2005). “Prevention of high-dose-rate brachytherapy accidents. ICRP publication 97”. In: *Ann. ICRP* 35.2.
- ICRU (1983). “Microdosimetry”. In: *ICRU Report* 36.
- (1985). “Recommended dose and volume specification for reporting interstitial brachytherapy”. In: *ICRU Report* 38.
- (2010). “Prescribing, recording, and reporting intensity-modulated photon-beam therapy (IMRT)”. In: *ICRU Report* 83.
- (2011). “Fundamental quantities and units for ionising radiation (revised)”. In: *ICRU Report* 11.1.
- Incerti, S et al. (2010). “Comparison of GEANT4 very low energy cross section models with experimental data in water”. In: *Med. Phys.* 37, pp. 4692–708.

- Incerti, S et al. (2013). "Energy deposition in small-scale targets of liquid water using the very low energy electromagnetic physics processes of the Geant4 toolkit". In: *Nucl. Inst. and Meth. in Phys. Research B* 306, pp. 158–64.
- Kellerer, A M (1985). *Fundamentals of microdosimetry*. Harcourt Brace Jovanovich.
- Kellerer, A M and H H Rossi (1984). "On the determination of microdosimetric parameters in time-varying radiation fields: the variance-covariance method". In: *Radiat. Res.* 97, pp. 237–45.
- Lillhok, J E et al. (2007). "Nanodosimetry in a clinical neutron therapy beam using the variance-covariance method and Monte Carlo simulation". In: *Phys. Med. Biol.* 52.16, pp. 4953–66.
- Lindborg, L and H Nikjoo (2011). "Microdosimetry and radiation quality determinations in radiation protection and radiation therapy". In: *Radiat. Prot. Dosim.* 143.2-4, pp. 402–8.
- Lindborg, L et al. (2013). "Lineal energy and radiation quality in radiation therapy: model calculations and comparison with experiment". In: *Phys. Med. Biol.* 58.1, pp. 3089–105.
- MacPherson, M S and J J Battista (1998). "Radioactivity measurements of ytterbium-169 brachytherapy sources". In: *Australas. Phys. Eng. Sci. Med.* 21.1, pp. 18–23.
- Mason, D L et al. (1992). "Ytterbium-169: calculated physical properties of a new radiation source for brachytherapy". In: *Med. Phys.* 19.3, pp. 695–703.
- Nath, R et al. (1995). "Dosimetry of interstitial brachytherapy sources: Recommendations of the AAPM Radiation Therapy Committee Task Group No. 43". In: *Med. Phys.* 22.1, pp. 209–34.
- Nikjoo, H and L Lindborg (2010). "RBE of low-energy electrons and photons". In: *Phys. Med. Biol.* 55.10, pp. 65–109.
- Nikjoo, H et al. (1991). "Energy deposition in small cylindrical targets by monoenergetic Electrons". In: *Int. J. Radiat. Biol.* 60.5, pp. 739–56.
- Papiez, M J and J J Battista (1994). "Radiance and particle fluence". In: *Phys. Med. Biol.* 39, pp. 1053–62.

- 
- Podgorsak, E B (2010). *Radiation physics for medical physicists*. 3rd ed. Springer-Verlag.
- Rivard, M J et al. (2004). "Update of AAPM Task Group No. 43 Report: a revised AAPM protocol for brachytherapy dose calculations". In: *Med. Phys.* 31.3, pp. 633–74.
- Rossi, H H and M Zaider (1995). *Microdosimetry and its applications*. Berlin: Springer-Verlag.
- Waker, A J (1995). "Principles of experimental microdosimetry". In: *Radiat. Prot. Dosim.* 61.4, pp. 297–308.
- WHO (2014). *Cancer Fact sheet No 297*. Retrieved 10 June 2014.

# Paper 1

# Microdosimetric evaluation of intermediate energy brachytherapy sources using GEANT4-DNA

Gabriel Famulari, Piotr Pater, Shirin A. Enger

## Abstract

**Purpose:** Radioisotopes such as  $^{75}\text{Se}$ ,  $^{169}\text{Yb}$  and  $^{153}\text{Gd}$  have photon energy spectra and half-lives that make them excellent candidates for use as radioactive sources in HDR brachytherapy. The purpose of this study is to perform a microdosimetric evaluation of the RBE at clinically relevant doses and dose rates for these potential novel sources.

**Materials and Methods:** Photon sources were modelled as point sources located in the center of a spherical water phantom with a radius of 40 cm using the Geant4 toolkit. The kinetic energy of all primary, scattered and fluorescence photons interacting in a scoring volume were tallied at various depths from the point source. Electron tracks were generated by sampling the photon interaction spectrum, and tracking all the interactions following the initial Compton or photoelectric interaction using the event-by-event capabilities of Geant4-DNA. The lineal energy spectra were obtained through random sampling of interaction points and overlaying scoring volumes within the associated volume of the tracks.

**Results and Discussion:** For low-LET radiation, the  $\bar{y}_D$ -ratio was approximately equal to the  $\alpha$ -ratio in the LQ-relation for a volume of about 30 nm. The weighting factors predicted were 1.10, 1.14, and 1.19 for  $^{75}\text{Se}$ ,  $^{169}\text{Yb}$ , and  $^{153}\text{Gd}$ , respectively. The intermediate energy sources  $^{75}\text{Se}$ ,  $^{169}\text{Yb}$ , and  $^{153}\text{Gd}$  are 5-15 % more biologically effective than current  $^{192}\text{Ir}$  sources. There is little variation in the radiation quality with depth from the source.

**Conclusion:** The clinical RBE for intermediate energy photon sources are considerably above unity and should be taken into account during treatment planning.

# 1 Introduction

## 1.1 Search for novel brachytherapy sources

Aiming at effective tumour sterilization with manageable side effects, the importance of brachytherapy is increasing in cancer therapy. Brachytherapy is commonly administered by gamma emitting radionuclides with low energies (Iodine-125 ( $^{125}\text{I}$ ) and Palladium-103 ( $^{103}\text{Pd}$ ),  $E < 50$  keV), intermediate energies (Ytterbium-169 ( $^{169}\text{Yb}$ ),  $50 \text{ keV} < E < 200 \text{ keV}$ ) or high energies (Iridium-192 ( $^{192}\text{Ir}$ ) and Cobalt-60 ( $^{60}\text{Co}$ ),  $E > 200$  keV (Beaulieu et al., 2012).  $^{192}\text{Ir}$  ( $t_{1/2} = 72$  days,  $E_{\gamma,avg} = 360$  keV) is a widely used isotope for high dose rate (HDR) brachytherapy, but has the disadvantage of emitting high-energy gamma radiation. This justifies the search for a radiation source with lower gamma energy and less shielding requirements.

Recent studies have identified and proposed gamma emitting radionuclides in the intermediate energy region that can provide radiobiological advantages, optimal depth dose profile, sufficient specific activity, nominal gamma energy, long half-life and minimal shielding requirements compared with  $^{192}\text{Ir}$ . Selenium-75 ( $^{75}\text{Se}$ ,  $t_{1/2} = 118.5$  days,  $E_{\gamma,avg} = 210$  keV) has been used as an alternative to  $^{192}\text{Ir}$  in industrial radiography, due to its softer gamma emission spectrum and significantly longer half-life (Grimm and Kaftal, 1996). Ytterbium-169 ( $^{169}\text{Yb}$ ,  $t_{1/2} = 32.0$  days,  $E_{\gamma,avg} = 93$  keV) had been considered as a radiation source for brachytherapy applications (Mason et al., 1992; MacPherson and Battista, 1998; Zellmer, Gillin, and Wilson, 1992; Meigooni and Nath, 1992), but is not currently manufactured. Gadolinium-153 ( $^{153}\text{Gd}$ ,  $t_{1/2} = 240.4$  days,  $E_{\gamma,avg} = 60$  keV) has theoretically been investigated as a brachytherapy source for use in intensity modulated brachytherapy (Enger, Fisher, and Flynn, 2013; Adams et al., 2014).  $^{75}\text{Se}$ ,  $^{169}\text{Yb}$  and  $^{153}\text{Gd}$  have photon energy spectra and half-lives that make them excellent candidates for use as radioactive sources in brachytherapy.

## 1.2 Relative biological effectiveness of electrons and photons

The biological effect (BE) of radiation is directly related to absorbed dose, but depends also on other factors such as fractionation, dose rate, radiation quality, biological system and endpoints. The BE is quantified in terms of the relative biological effectiveness (RBE), defined as the ratio between the absorbed dose of a reference radiation such as  $^{60}\text{Co}$  and that of a test radiation for a given biological endpoint.

Clinical experience of fractionated treatments can be summarized by a linear-quadratic (LQ) dose response relationship (Brenner, 2008) as well as clinical RBE values,  $W_{isoE}$ , which are reported weighting factors (IAEA, 2008). The LQ relation can be described as:

$$\text{BE} = \alpha nd + \beta nd^2 = \alpha D \left( 1 + \frac{d}{(\alpha/\beta)} \right), \quad (1)$$

where  $d$  is the fraction of the total absorbed dose,  $D$ , delivered in  $n$  equal fractions, and  $\alpha$  and  $\beta$  are independent of each other and the initial and final slope of the survival curves for the irradiated cells. The LQ formalism describes a biophysical model of cell killing, where  $\alpha$  depends both on the biological endpoint and the radiation quality, while  $\beta$  only depends on the endpoint. The above relation is expected to be valid for doses in the range of 2-10 Gy.

If treatments are given with two different radiation qualities, the goal is to achieve the same biological effect with the equation below:

$$W_{isoE,X} = \frac{D_\gamma}{D_X} = \frac{\alpha_X \left( 1 + \frac{d_X}{(\alpha/\beta)_X} \right)}{\alpha_\gamma \left( 1 + \frac{d_\gamma}{(\alpha/\beta)_\gamma} \right)}. \quad (2)$$

where the subscripts  $X$  and  $\gamma$  represent the test radiation and the reference radiation, respectively. For early reacting tissues and many tumours exposed to low linear energy transfer (LET) beams, the  $\alpha/\beta$  ratio is on the order of  $10 \text{ Gy}^{-1}$  (Thames and Hendry, 1987). For a typical fraction of  $d = 2 \text{ Gy}$ , the BE is dominated by the first term within the parenthesis. The weighting factor for low-LET radiation can then be approximated

as the  $\alpha$ -ratio between the two radiation qualities:

$$W_{isoE,X} = \frac{D_\gamma}{D_X} \approx \frac{\alpha_X}{\alpha_\gamma}. \quad (3)$$

Currently, the International Commission on Radiation Protection assigns a radiation weighting factor (RBE) of unity for all photon emitting sources (ICRP, 2007), equating the RBE of high and low energy photon sources. However, experimental and calculated studies with low energy X-ray sources (Barendsen and Walter, 1963; Wambersie and Dutreix, 1971; Zeitz et al., 1977) and electronic brachytherapy (eBt) sources (Brenner et al., 1999; White et al., 2016) have shown that the RBE at clinically relevant doses and dose rates for low energy photon sources are considerably above unity. If new intermediate energy brachytherapy sources will be introduced into the clinic, the RBE of such sources should be taken into account during the treatment planning stage.

### 1.3 Evaluation of RBE using microdosimetry

Microdosimetry has been used extensively to characterize radiation quality in radiation therapy and radiation protection. While LET is a macroscopic quantity defined by the average energy lost by a particle, the lineal energy  $y$  is a stochastic quantity describing the distribution of energy deposited by ionizing radiation in a microscopic region, or domain, such as the DNA. If the probability of damage on the nanometre level is related to the energy imparted to a relevant volume, then it is better described by the microdosimetric distribution for the same object size than by the LET.

Lineal energy is a recommended quantity for the evaluation of radiation quality and RBE. However, lineal energy distributions can vary significantly with the size and shape of the scoring volumes used. It is therefore crucial to establish the target volumes for which the lineal energy is directly proportional to the clinical RBE, or weighting factor. According to various computational and experimental studies (Grindborg and Olko, 1997; Lindborg and Grindborg, 1997; Lillhok et al., 2007; Lindborg et al., 2013;

Lindborg et al., 2015), it has been concluded that the dose mean lineal energy  $\bar{y}_D$  in a volume of about 10-15 nm is approximately proportional to the  $\alpha$ -ratio derived from the LQ relation in fractionated radiotherapy in both low-LET and high-LET radiation:

$$\frac{\alpha_X}{\alpha_\gamma} \approx \frac{\bar{y}_{D,X}}{\bar{y}_{D,\gamma}}. \quad (4)$$

In the LQ model, the  $\alpha$  coefficient is the parameter related to the yield of lethal lesions produced by single radiation tracks, and can be approximated to first order by the single event dose mean lineal energy  $\bar{y}_D$ , a term which only accounts for the direct action of radiation on DNA.

Microdosimetric distributions can typically be measured using tissue-equivalent proportional counters (TEPC) or simulated using Monte Carlo (MC) track structure (TS) (MCTS) simulation codes. MCTS simulations rely on interaction cross sections of charged particles with matter and require total and differential cross sections of all ionization or excitation processes considered. This is different from the commonly used MC simulations based on continuous slowing down approximation, also called condensed history technique, where the only ingredient is the stopping power, or energy loss per track length. In the condensed-history, which is a macroscopic MC approach, the path of charged particles is divided into a number of steps during which the effect of several interactions is handled together by appropriate multiple-scattering theories.

However, since the tissue-equivalent diameter of the detectors are typically in the order of 1  $\mu\text{m}$  and measurements of the energy deposition in nanometre sized volumes is very difficult, containing large uncertainties, MCTS simulations are the preferred method to calculate quantities of interest in these small volumes. To calculate the lineal energy distributions in macroscopic regions, it is necessary to integrate MCTS simulations with macroscopic MC simulations to be time efficient.

---

## 1.4 Objectives

The main goal of this study is to perform a microdosimetric evaluation of the clinical RBE for fractionated radiotherapy for novel/potential intermediate energy HDR brachytherapy sources, using a combination of MCTS simulations and track sampling algorithms.

## 2 Materials and Methods

### 2.1 Generation of electron tracks

Electron tracks from photon sources are generated in a two step process using the MC toolkit Geant4 (Agostinelli et al., 2003). In a first simulation, monoenergetic photons and brachytherapy sources are modelled as point sources located in the center of a spherical water phantom with a radius of 40 cm. The kinetic energy of all primary, scattered and fluorescence photons interacting in spherical shells are tallied. The shells have a thickness equivalent to twice the CSDA range of the most energetic electrons that can be set in motion by the photon source. The radioactive decay for brachytherapy sources is handled through nuclear decay i.e. there are no hard coded decay spectra for the studied isotopes. The radioactive decay data comes from the Evaluated Nuclear Structure Data File (ENSDF) which is maintained by Brookhaven National Laboratory. Photons are tracked using the standard Livermore physics list with atomic deexcitation activated. The pre-step kinetic energy of all photons that interact within each volume is recorded. Electrons are not tracked during this phase, which speeds up the simulation. The kinetic energies are grouped in bins of 100 eV for energies less than 1 keV and in bins of 1 keV for energies greater than 1 keV. At least  $10^8$  histories are simulated for each source to ensure good statistics for the energy distribution.

In a second simulation, 1000 electron tracks are generated by sampling the photon interaction spectrum, and tracking all the interactions following the initial Compton or photoelectric interaction using the event-by-event capabilities of Geant4-DNA (Incerti

et al., 2010; Bernal et al., 2015). The method assumes that photons interactions within a given shell will generate electron tracks which will deposit energy in smaller scoring volumes (1~1000 nm) randomly distributed throughout the shell. The source is simulated as a point source in an infinitely large water phantom. All electrons are tracked down to 10 eV, at which point their energy is deposited locally. All secondary photons, including fluorescent photons, are killed. Atomic deexcitation is activated for processes producing vacancies in atomic shells (fluorescence, Auger electron emission). The Geant4-DNA processes are only valid for photons and electrons with energies up to 1 MeV. However, the  $^{60}\text{Co}$  interaction spectrum contains energies in the  $1 \text{ MeV} < h\nu < 1.33 \text{ MeV}$  range. If an energy above 1 MeV is sampled, then the energy is set to 1 MeV. Bremsstrahlung is unlikely below 1 MeV in water and can therefore be ignored. Pair production cannot occur below 1 MeV.

## 2.2 Random sampling and scoring

Lineal energy measurements require calculating the distribution of energy deposited for single events in the scoring volume. Lineal energy is defined as:

$$y = \frac{E}{\bar{l}} \quad (5)$$

where  $E$ ,  $\bar{l}$ , and  $y$  denote the energy deposited in the scoring site, mean chord length, and lineal energy, respectively (ICRU, 1983). The mean chord length for convex objects under mean-free path randomness ( $\mu$ -randomness), which occurs when all tracks intersecting the sphere originate uniformly from random points in space and are isotropically distributed, has been studied in detail (Kellerer, 1985). The mean chord length is  $\bar{l} = \frac{4}{3}r$  for spheres with radius  $r$  and  $\bar{l} = \frac{2rh}{r+h}$  for cylinders with radius  $r$  and height  $h$ . The single event dose-mean lineal energy  $\bar{y}_D$  can be obtained:

$$\bar{y}_D = \int y d(y) dy = \frac{\int y^2 f(y) dy}{\int y f(y) dy} \quad (6)$$

where  $f(y)$  and  $d(y)$  represent the frequency and dose distributions of lineal energy, respectively.

The random sampling of the track is performed using the concept of associated volume. The associated volume of a track is the volume around the track with a sampling efficiency of exactly one. Sampling is performed by overlaying scoring volumes inside this associated volume. For spherical scoring volumes, random sampling is performed by randomly selecting a transfer point, randomly placing a sphere of radius  $r_{sv}$  within a distance  $r_{sv}$  from the transfer point, and recording the energy deposited within the scoring sphere. For cylindrical scoring volumes, random sampling requires randomly overlaying a cylinder of radius  $r_{sv}$ , height  $h_{sv}$ , and a randomly determined orientation, on a cylinder with the same dimensions and orientation centered on the transfer point, and recording the energy deposited within the scoring cylinder. By sampling the interaction points, this ensures that each sampling step will score at least one energy deposition, thus minimizing the computation time required. However, this method is biased towards region of high density of transfer points. In order to avoid oversampling areas of tracks where the density of transfer points are greater, the energy deposition event is scored with a weight  $\omega_{ed}$  inversely proportional to the number of energy deposition events within the scoring volume. Each track is sampled 1000 times, irrespective of the track's associated volume. To account for the fact that longer tracks have a greater probability to interact with a given scoring volume, the event is also weighted by a factor  $\omega_{av}$  proportional to the associated volume of the track, which is estimated as the union of spheres of radius  $r_{sv}$  for spherical scoring volumes and radius  $r = \sqrt{r_{sv}^2 + (h_{sv}/2)^2}$  for cylindrical scoring volumes centered at each transfer point. The dose-mean lineal energy can then be calculated according to the equation:

$$\bar{y}_D = \frac{\sum_{i=1}^N y_i^2 \omega_{ed,i} \omega_{av,i}}{\sum_{i=1}^N y_i \omega_{ed,i} \omega_{av,i}} \quad (7)$$

where  $\omega_{ed,i}$  and  $\omega_{av,i}$  represent the appropriate weights for each scoring event  $i$ . The analysis was performed using Matlab R2014a. scoring

## 2.3 Simulations

As a validation of the random sampling algorithm, the relative frequency distribution of energy deposited  $f(> E)/f(> 0)$  was calculated for 1, 10, and 100 keV electrons and 10, 100, and 1000 nm spheres using both the associated volume technique and uniform sampling of tracks. The relative frequency distribution  $f(> E)/f(> 10 \text{ eV})$  for 1 keV electrons was then simulated for a few cylindrical scoring volumes ( $2 \text{ nm} \times 2 \text{ nm}$ ,  $25 \text{ nm} \times 25 \text{ nm}$ ), and the results were compared to previous work using the Geant4-DNA physics list (Incerti et al., 2013). Dose-mean lineal energy values were calculated for 1 keV and 100 keV monoenergetic electrons using cylinders with equal height and diameter in the 5-1000 nm range.

Lineal energy distributions were calculated for common/potential brachytherapy sources ( $^{60}\text{Co}$ ,  $^{192}\text{Ir}$ ,  $^{75}\text{Se}$ ,  $^{169}\text{Yb}$ ,  $^{153}\text{Gd}$ , and  $^{125}\text{I}$ ), and 100 kVp X-ray source at distances of 0.5, 5, 10, and 15 cm from the center, using spheres with 5-1000 nm diameter. The 100 kVp X-ray spectrum was simulated using the *SpekCalc* user code (Poludniowski et al., 2004), included 7 mm Be window, 3.14 mm Al filter and  $30^\circ$  target angle, and was scored at 0.5 m from the source in air. The dose-mean lineal energy ratios were tallied using  $^{60}\text{Co}$  at 5 mm depth as the reference.

## 3 Results and Discussion

### 3.1 Validation of sampling algorithm

Figure 1 shows the cumulative relative frequency distributions of energy deposition  $f(> E)/f(> 0)$  for various incident electron kinetic energies and spherical volumes obtained using the methodology described in this study, as well as through spatially random sampling of tracks. The agreement between the methods is very good for all

energies and scoring volumes considered, which confirms the consistency of the sampling algorithm presented in this work. The general agreement between the curves demonstrates that the concept of  $\mu$ -randomness holds even for very low electron energies, where the tracks do not necessarily intersect the scoring volumes in straight lines.

Uniform sampling consists of randomly placing scoring volumes within the bounding box of the track and storing the energy deposited, but is far less efficient in terms of computation time. As an example, Rossi and Zaider (Rossi and Zaider, 1995) estimate that for low LET radiation and for a radius smaller than 10 nm, the sampling efficiency is only about 1 %, whereas our methodology always has a sampling efficiency of 100 %.

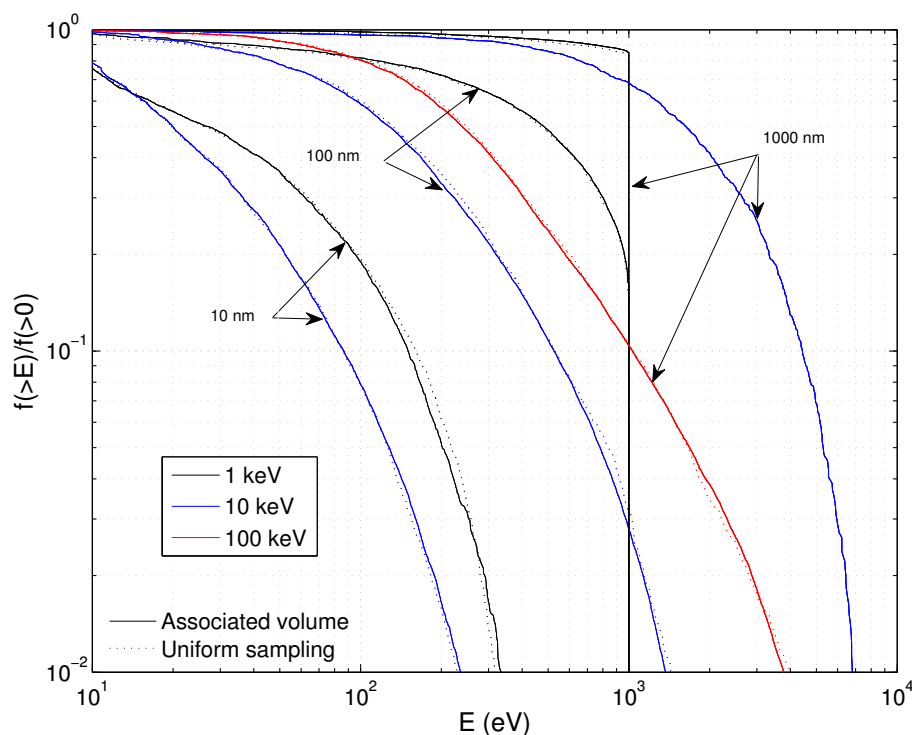


FIGURE 1: Relative frequency distribution of the energy deposition  $f(>E)/f(>0)$  obtained using the associated volume method (full line) and uniform sampling (dashed line), for various monoenergetic electron energies and spherical scoring volumes. The results are presented in cumulative form.

### 3.2 Monoenergetic electrons

Figure 2 shows the cumulative relative frequency distributions of energy deposition above 10 eV  $f(> E)/f(> 10 \text{ eV})$  for 1 keV electrons, using  $2 \text{ nm} \times 2 \text{ nm}$  and  $25 \text{ nm} \times 25 \text{ nm}$  cylindrical targets. The 10 eV lower limit permits the comparison to previous data obtained using Geant4-DNA (Incerti et al., 2013) and MOCA8B (Nikjoo et al., 1991), where scoring was made by enclosing entire tracks in a spherical virtual volume, representing a cell nucleus, in which cylindrical targets to be scored were randomly placed. While the absolute frequency of energy deposition  $f(> E)$  per Gy per target can not be obtained with our methodology, the relative distribution can be presented to compare different physics models and sampling algorithms.

For 1 keV electron tracks, the global tendency of the energy deposition distribution in this work agrees quite well with the results obtained by Incerti *et al.*, with small differences observed for larger scoring volumes. However, there is a significant difference between the results obtained with MOCA8B and those obtained with Geant4-DNA, as MOCA8B produces a greater amount of higher energy deposits. This can be explained by a difference in differential and total ionization cross section between the codes. In particular, for 1 keV electrons, the Geant4-DNA stopping power is about 40 % lower than for MOCA8B (Incerti et al., 2010). This will effectively lower the amounts of high energy deposits in favour of low energy deposits. Unfortunately, to the authors' knowledge, energy deposition distributions obtained using Geant4-DNA physics models for higher energy incident electrons have not been published, which limits the comparison between the different methods to a single energy and a few target geometries. This is not surprising, as larger virtual volumes would be needed to enclose electron tracks with higher energy, requiring a significant increase in computational power.

Figure 3 shows the dose mean lineal energy  $\bar{y}_D$  as a function of object diameter for 1 keV and 100 keV monoenergetic electrons, for cylindrical scoring volumes with

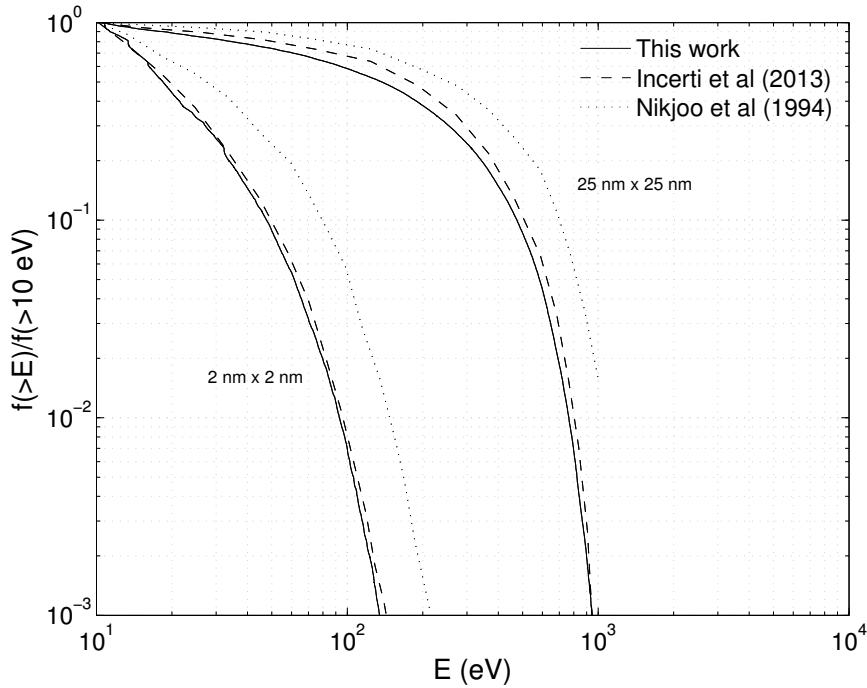


FIGURE 2: Relative frequency distribution of the energy deposition above 10 eV  $f(> E)/f(> 10 \text{ eV})$  for 1 keV electrons, using  $2 \text{ nm} \times 2 \text{ nm}$  and  $25 \text{ nm} \times 25 \text{ nm}$  cylindrical scoring volumes. The results are compared to previous data obtained with Geant4-DNA by Incerti *et al.* (2013) and with MOCA8B by Nikjoo *et al.* (1991). The results are presented in cumulative form.

equal height and diameter, and compares the results to those obtained using the electron transport codes MOCA8B (Nikjoo *et al.*, 1994) and KURBUC (Nikjoo *et al.*, 2011). For the majority of scoring volume sizes, the  $\bar{y}_D$  calculated with Geant4-DNA are significantly lower than those predicted by MOCA8B and KURBUC for both 1 keV and 100 keV electrons, for reasons explained above. In addition, the differences between the  $\bar{y}_D$  values generally become larger as the object diameter decreases. It is therefore expected that these differences in the  $\bar{y}_D$  for electrons in the nanometre range will lead to inconsistencies in the  $\bar{y}_D$  for low energy photons between the various MCTS codes.

### 3.3 Photon beams

Values of  $\bar{y}_D$  for a large range of scoring volumes have been reported both by experiments and track structure calculations for a 100 kV X-ray beam (added filter 3.14 mm

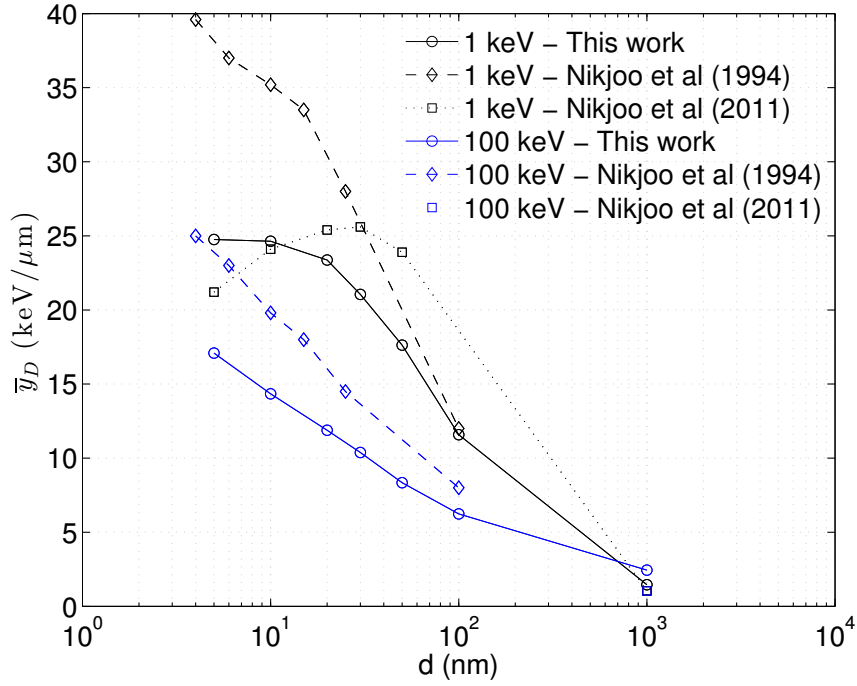


FIGURE 3: Dose mean lineal energy  $\bar{y}_D$  as a function of object diameter  $d$  for 1 keV and 100 keV monoenergetic electrons, using cylindrical scoring volumes with equal height and diameter. The results are compared to previous data obtained with MOCA8B by Nikjoo *et al.* (1994) and with KURBUC by Nikjoo *et al.* (2011).

Al) and a  $^{60}\text{Co}$  Siemens therapy beam (Grindborg, Samuelsson, and Lindborg, 1995; Grindborg and Olko, 1997). In order to compare the results from different MCTS codes, it was necessary to simulate both spectra. The photon fluence spectrum generated by the software SpekCalc is shown in figure 4, and is meant to approximate the output of the 100 kV X-ray therapy unit (HVL = 0.144 mm Cu) used in their microdosimetry studies. Since the make of the X-ray unit was not specified and a target angle was needed for the simulation, a typical angle of  $30^\circ$  was chosen, resulting in a mean energy of 49.7 keV and HVL = 0.129 mm Cu.

Figure 5 shows  $\bar{y}_D$  for both the 100 kV X-ray beam and  $^{60}\text{Co}$   $\gamma$  beam for a range of spherical scoring sites. The results from our track structure simulations were compared to previous calculations for  $^{60}\text{Co}$  (Grindborg and Olko, 1997) and for 100 kV X-rays (Lindborg *et al.*, 2013). As expected from the results in section 3.2, the  $\bar{y}_D$  predicted by Geant4-DNA are generally lower than those calculated in previous studies.

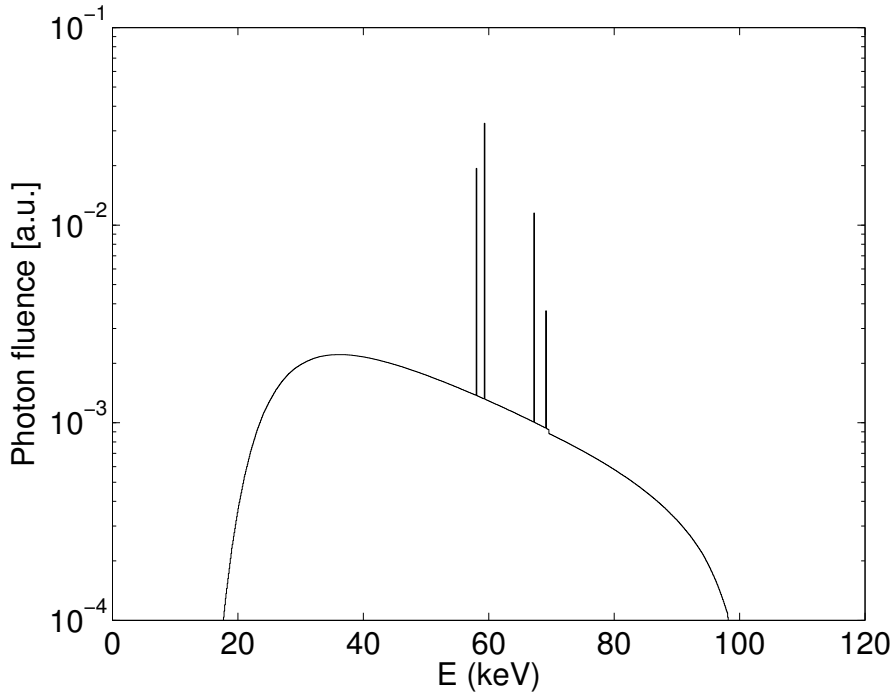


FIGURE 4: Photon fluence spectrum of an 100 kV X-ray tube (7 mm Be window, 3.14 mm Al filter, 30° target angle) measured at 0.5 m from the source. Spectrum was generated using SpekCalc.

This was expected, as previous studies (Lillhok et al., 2007; Lindborg et al., 2013) calculated  $\bar{y}_D$  by weighting the relative dose fraction for electrons with given energies by the energy dependent  $\bar{y}_D(E)$  for monoenergetic electrons, calculated with an electron transport code such as MOCA8B or KURBUC. The photon microdosimetry calculations were therefore relying on the accuracy of the low energy physics models used in the electron calculations, which has been vastly improved with the arrival of Geant4-DNA. Producing lineal energy distributions directly using track structure simulations and fast sampling algorithms eliminates the need to combine a dataset of energy dependent  $\bar{y}_D(E)$  for monoenergetic electrons (which typically have to be interpolated for calculation purposes) with particle fluences or dose profiles.

Furthermore, the lineal energy calculations in nanometre domains were typically calculated in cylindrical volumes for electrons and in spherical volumes for photons, which introduced another inconsistency, as cylinders and spheres with the same mean chord length  $\bar{l}$  (under  $\mu$ -randomness) have different volumes and can measure slightly

different energy deposition patterns. It is therefore crucial to establish general standards for microdosimetric calculations using track structure simulations, such that results can be compared equivalently.

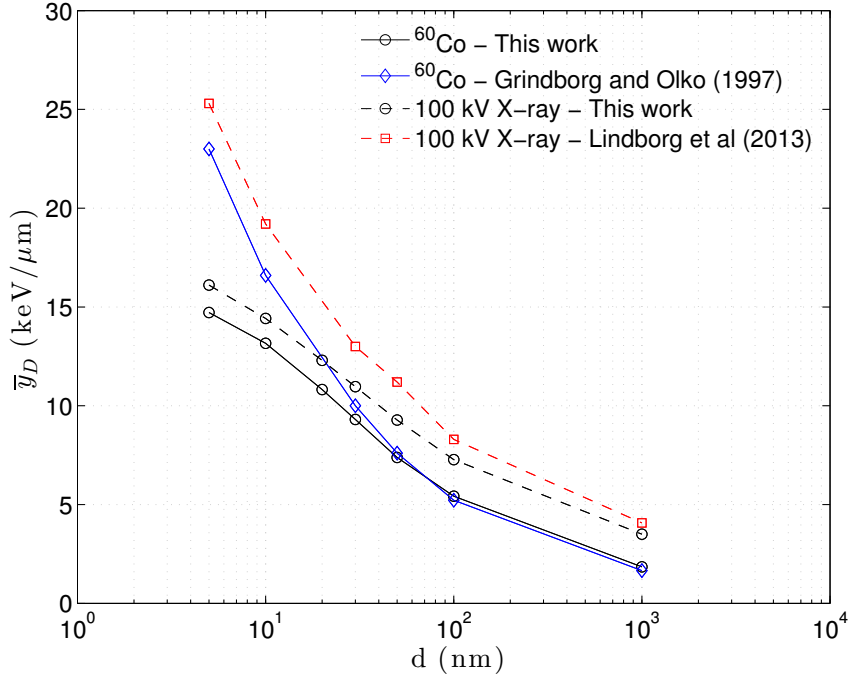


FIGURE 5: Dose mean lineal energy  $\bar{y}_D$  as a function of spherical site diameter  $d$  for  $^{60}\text{Co}$   $\gamma$ -rays and 100 kV X-rays at 5 mm depth in water. The results are compared to Grindborg and Olko (1997) for  $^{60}\text{Co}$  and Lindborg *et al.* (2013) for 100 kV X-rays.

While the  $\bar{y}_D$  values agree within typical uncertainties ( $\pm 20\%$ ) expected in microdosimetry for larger diameter spherical sites, the disagreement between the codes becomes more significant for smaller scoring volumes ( $r \leq 20$  nm). The differences in the  $\bar{y}_D$  caused a shift in the curves for  $\bar{y}_{D,X}/\bar{y}_{D,\gamma}$  ratio between  $^{60}\text{Co}$   $\gamma$ -rays and 100 kV X-rays, as demonstrated in figure 6. For a given site size, the lineal energy ratios calculated in this study are lower than those calculated by Lindborg *et al.*. For instance, the ratio between these two radiation qualities at 10 nm has dropped from 1.16 to 1.08. This has important ramifications, since the diameter at which the  $\bar{y}_D$ -ratio coincides with the determined  $\alpha$ -ratio of 1.20 is closer to 30 nm than it is to 10-15 nm. However, it is important to note that a conservative  $\pm 5\%$  uncertainty in the  $\alpha$ -ratio will have a consequence that the diameter of interest would be in the 20-50 nm range according to

our calculations, compared to the 10-20 nm range predicted by the previous study. An accurate, suggested value for the clinical RBE between the two radiation qualities is needed to determine the relevant object size for microdosimetric measurements, since small changes in the  $\alpha$ -ratio will result in significant differences in the object volume.

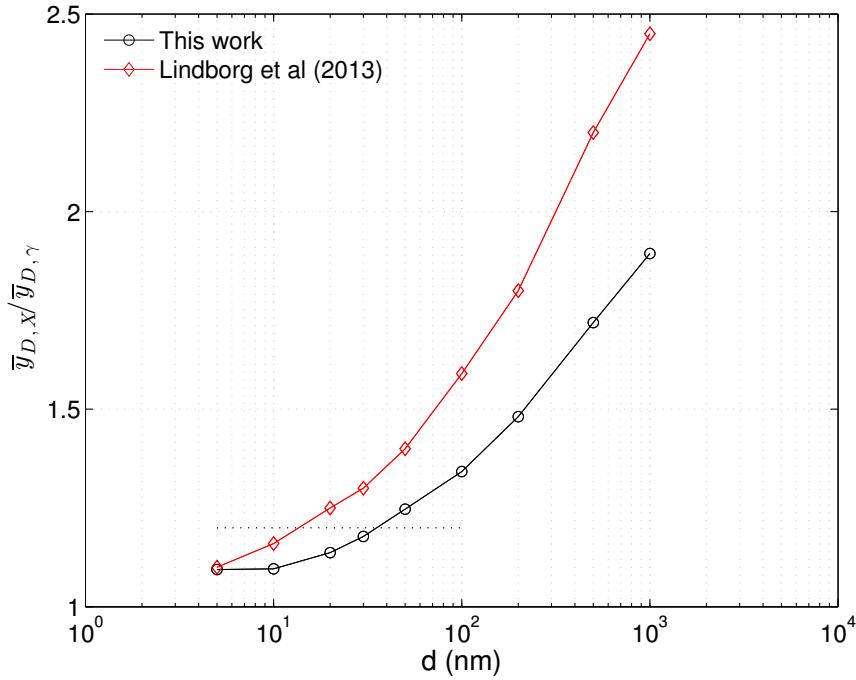


FIGURE 6: Dose mean lineal energy ratios  $\bar{y}_{D,X}/\bar{y}_{D,\gamma}$  between  $^{60}\text{Co}$   $\gamma$ -rays and 100 kV X-rays as a function of spherical site diameter at 5 mm depth in water. The results are compared to Lindborg *et al.* (2013). The horizontal line corresponds to  $\alpha$ -ratio of 1.20.

### 3.4 Microdosimetric evaluation of brachytherapy sources

The lineal energy spectra for the brachytherapy sources under investigation are presented in figure 7, for a range of depths in water. The dose mean lineal energy values as a function of depth are also shown in figure 8. The uncertainties are reported as standard error. While the photon fluence spectrum typically hardens with increasing distance from the source,  $\bar{y}_D$  does not vary significantly for the variety of photon sources studied. This is in line with the conclusions from other simulation studies with low-energy X-ray sources (White *et al.*, 2016; Kirkby *et al.*, 2013). The uncertainty in

the mean values is dominated by the statistical fluctuations of the track sampling algorithm. Small differences can be noticed in the lineal energy distributions, but the combined effect results in a fairly constant mean. This signifies that in order to characterize an average RBE for a source, any depth in the phantom can be chosen as an appropriate depth for measurement. To be consistent, a depth of 5 mm was chosen as the depth of calculation since it is close enough to the source to ensure optimal statistics for the photon interaction spectrum, but is far enough from the source such that the scoring volume is beyond any potential source, encapsulation and applicator design.

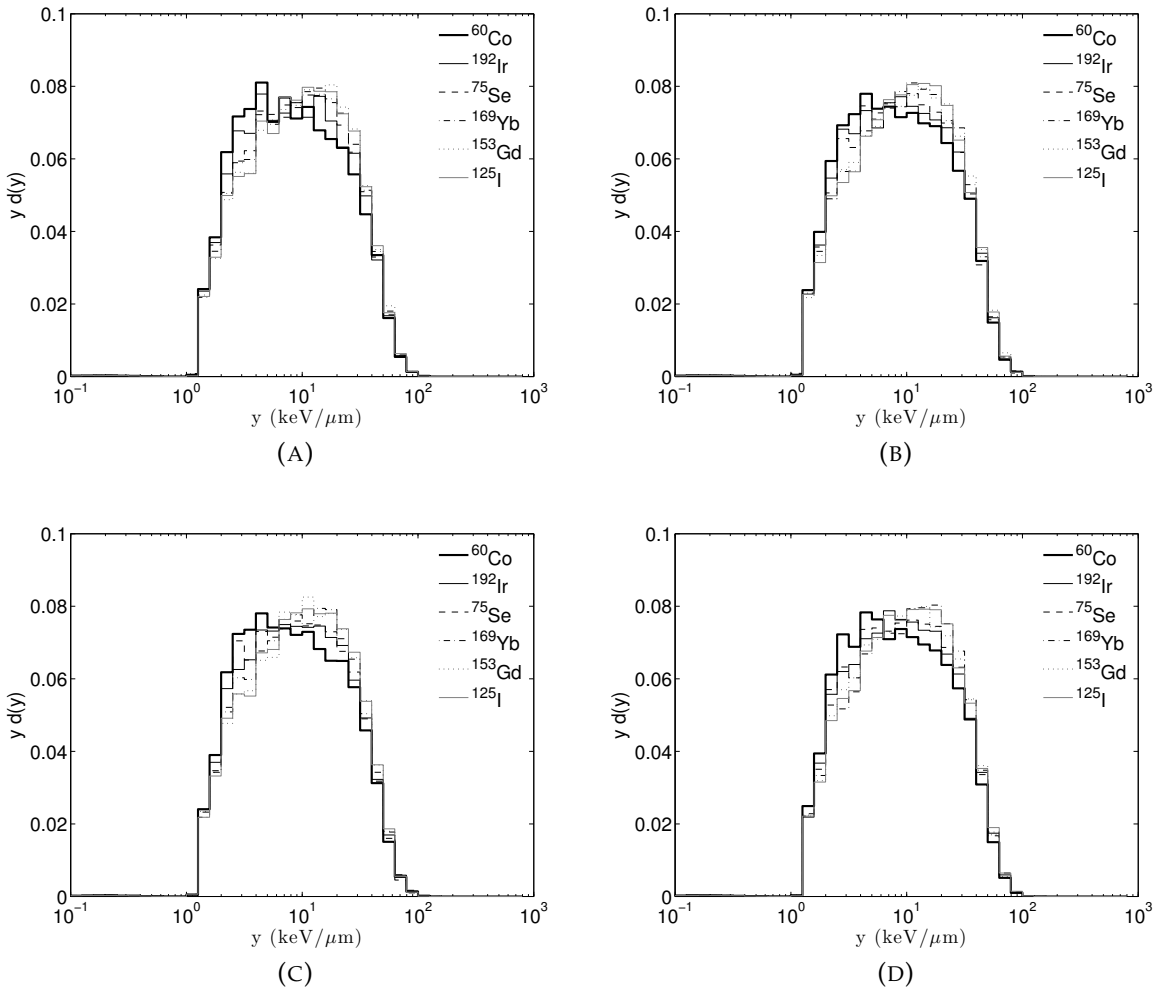


FIGURE 7: Lineal energy spectra for various brachytherapy sources at (a) 5 mm, (b) 50 mm, (c) 100 mm and (d) 150 mm depth in water, for 10 nm spheres. Equal area under the curve corresponds to equal fraction of dose deposition.

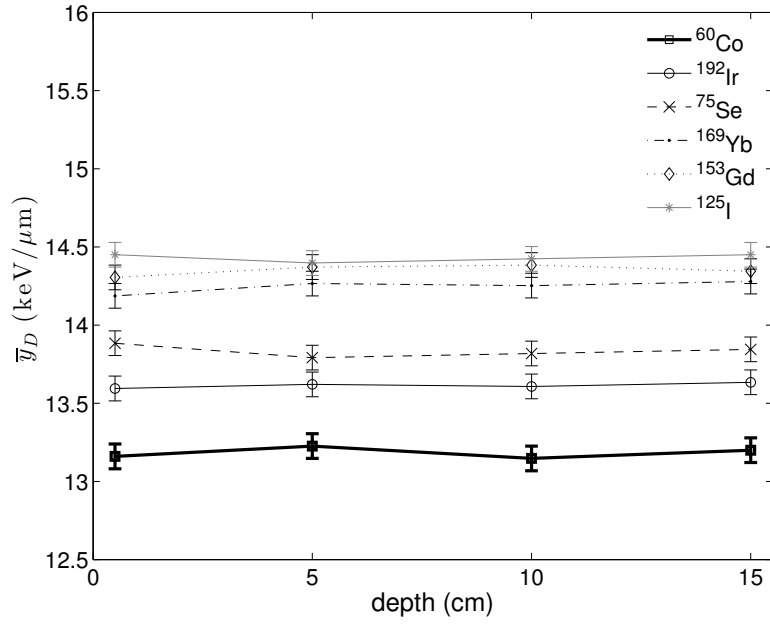


FIGURE 8: Dose mean lineal energy  $\bar{y}_D$ , for 10 nm spheres, as a function of radial distance from the source for various brachytherapy isotopes.

It is important to note that a point source was used in this study and placed in a center of a water phantom. The main reasoning being that the dimensions of the potential intermediate energy brachytherapy sources have yet to be established. This ensures fair comparison between the sources. The effect of the inclusion of the source, encapsulation and applicator design on  $\bar{y}_D$  has not been investigated and is beyond the scope of this work. The results from this study should only be used as a general guide for the estimation of biological effectiveness. It is expected, however, that small changes in the fluence spectrum, due to photon attenuation and in scatter within the capsule, will have a minimal effect on  $\bar{y}_D$ , based on the conclusions reached in this section.

As photon energy decreases,  $\bar{y}_D$  generally increases. However, the radiation quality of  $^{153}\text{Gd}$  is comparable to that of  $^{125}\text{I}$ , even though the average photon energy decreases from 60 keV to 30 keV. Although a softer spectrum would typically result in a higher lineal energy, this is not the case in the 20-80 keV range. As photon energy decreases from 80 keV to 20 keV, the kinetic energy of the photoelectrons, Auger electrons and Compton electrons set in motion will decrease, but this is offset by the relative increase

in the production of photoelectrons, since the photoelectric cross section is higher at lower energies. An intermediate-energy brachytherapy source such as  $^{153}\text{Gd}$  is therefore expected to be just as biologically effective as a low energy source, while having an ideal radial dose function for HDR brachytherapy applications (Enger, Fisher, and Flynn, 2013).

The lineal energy spectra are presented for 10 nm and  $1\ \mu\text{m}$  sites in figure 9. The distributions shift towards higher lineal energy for lower photon energy, but this shift is more obvious for larger scoring sites. While distributions can look significantly different on a larger scale based on the energies of the primary and secondary particles, the energy deposition patterns tend to resemble one another on a much smaller scale.

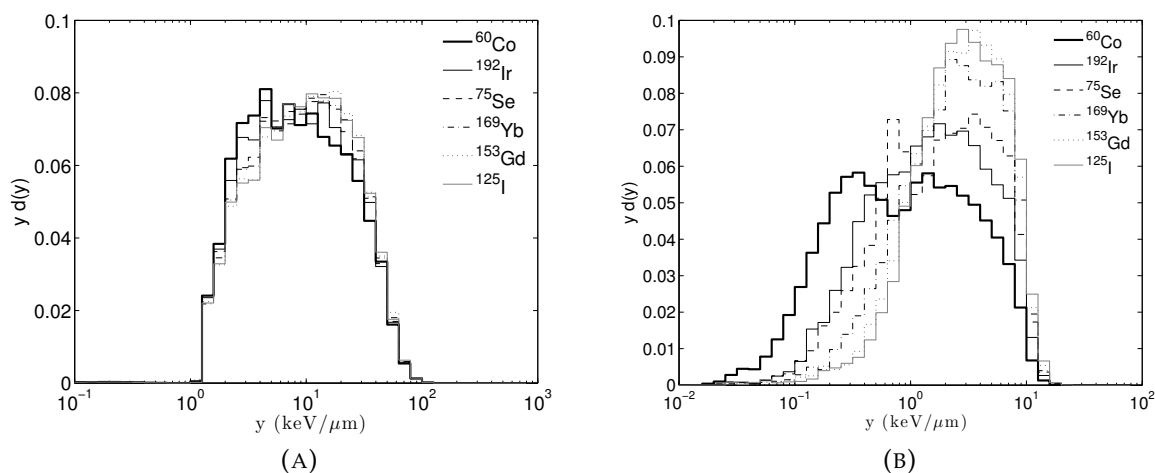


FIGURE 9: Lineal energy spectra for various brachytherapy sources at 5 mm depth in water, for (a) 10 nm and (b)  $1\ \mu\text{m}$  spheres. Equal area under the curve corresponds to equal fraction of dose deposition.

The two peaks occurring in the center of the  $^{60}\text{Co}$  spectrum ( $0.2\ \text{keV}\ \mu\text{m}^{-1} < y < 2\ \text{keV}\ \mu\text{m}^{-1}$ ) in figure 9b are typically not visible in measured and simulated lineal energy distributions, but has been noted in simulation studies with the PENELOPE code (Stewart et al., 2002; Hugtenburg, Chaoui, and Pattison, 2007; Chiriotti et al., 2014). This double peak is also visible for the 10 nm site, but to a lesser extent. The occurrence of these peaks are likely due to shortcomings of the model used to sample the differential cross section for small energy transfers associated with inelastic scattering. The

authors encourage future studies to include spectra, not only mean values, to allow comparison between physics models, track structure codes, and sampling algorithms.

The dose mean lineal energy ratios  $\bar{y}_{D,X}/\bar{y}_{D,\gamma}$  are shown as a function of object diameter  $d$  for various brachytherapy sources in figure 10. For a given brachytherapy source, the  $\bar{y}_D$ -ratio increases with larger scoring volume sites. The ratios of 1.05 and 1.18 at about 30 nm for  $^{192}\text{Ir}$  and  $^{125}\text{I}$ , respectively, seem to correlate well with published experimental data and simulations, as expected from the results in section 3.3. Scalliet and Wambersie (Scalliet and Wambersie, 1987) claim that the RBE values for  $^{125}\text{I}$  in the 1.15-1.20 range are in general observed for high doses and high dose rates. Pater *et al.* (Pater et al., 2016) calculated RBE values for double strand break (DSB) induction of 1.04 and 1.16 for  $^{125}\text{Ir}$  and  $^{125}\text{I}$ , respectively, using a combination of Geant4 with DNA damage yields for monoenergetic electrons from the Monte Carlo Damage Simulation (MCDS) software. It is therefore expected that the results obtained using our methodology at 30 nm, which can correctly predict the RBE for the high and low energy radioisotopes, can be used to predict the  $\alpha$ -ratios for the intermediate energy sources.

Based on the results at 30 nm, we predict that the weighting factors for  $^{75}\text{Se}$ ,  $^{169}\text{Yb}$ , and  $^{153}\text{Gd}$  sources will be 1.10, 1.14, and 1.19, respectively. The intermediate energy sources  $^{75}\text{Se}$ ,  $^{169}\text{Yb}$ , and  $^{153}\text{Gd}$  can potentially be 5-15 % more biologically effective than current  $^{192}\text{Ir}$  sources.

Microdosimetric quantities such as lineal energy represent a very powerful tool for medical physicists and radiation biologists, since only the physical properties of energy deposition are required to directly predict the entire effects (direct and indirect) of radiation on a cell culture, or *in vivo*. However, verification of the accuracy of simulated microdosimetric data is difficult in nanometre sized targets, since the experimental uncertainties of TEPC measurements are very large below 30 nm and are simply unreliable. Extremely accurate cross section models for MCTS simulation codes are needed for the modelling of microdosimetry calculations, and to correctly predict the appropriate volume of interest that correlates with the weighting factors.

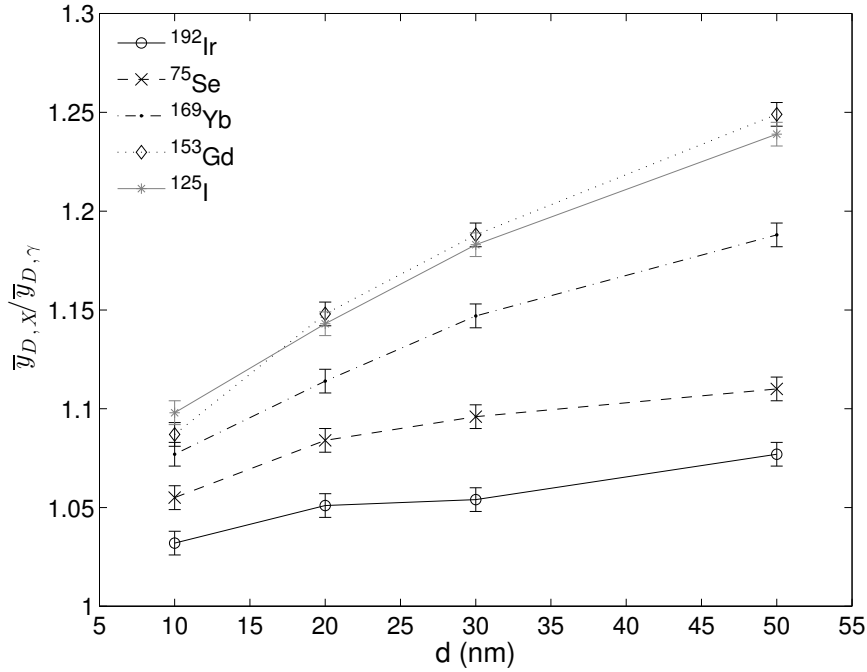


FIGURE 10: Dose mean linear energy ratios  $\bar{y}_{D,X}/\bar{y}_{D,\gamma}$  as a function of object diameter  $d$  for various brachytherapy sources. The reference value refers to  $^{60}\text{Co}$   $\gamma$ -rays at 5 mm depth.

The approximation between the clinical weighting factor  $W_{isoE}$  (often denoted clinical RBE) and the  $\alpha$ -ratio for fractionated radiotherapy contains a few caveats. First, it is assumed the weighting factor is equivalent to the clinical RBE to express the weighting of the dose when changing from one radiation quality to the other. However, there are other factors than the clinical RBE that may influence the absorbed dose, such as the dose distribution. In many cases, the dose given to a tumour is limited by the dose given to organs at risk (OAR), which can vary if the dose distribution is also altered. Second, it is assumed that the  $\alpha/\beta$  ratio is constant for low LET radiation, which is only valid for megavoltage photons and for early responding endpoints (Thames and Hendry, 1987). In the kilovoltage regime, the  $\alpha/\beta$  ratio can vary based on the endpoint, tissue type, radiation quality, dose, dose rate and fractionation scheme. However, a ratio between 8-14 Gy will only result in an error of at most 5 %.

## 4 Conclusions

The biological effectiveness for fractionated radiotherapy for potential intermediate energy HDR brachytherapy sources was evaluated by comparing the dose mean lineal energy values in nanometre sized volumes. The lineal energy spectra were obtained through random sampling of electron tracks, by overlaying scoring volumes within the associated volume of the tracks. It was demonstrated that, for low-LET radiation, the  $\bar{y}_D$ -ratio was approximately equal to the  $\alpha$ -ratio in the LQ-relation for a volume of about 30 nm. Intermediate energy radioisotopes can be 5-15% more biologically effective than  $^{192}\text{Ir}$  sources currently used in HDR brachytherapy, while offering better dose distributions and reducing shielding requirements. The biologically weighted dose of the sources must be taken into account during the treatment planning stage.

## Acknowledgements

We would like to acknowledge support from the CREATE Medical Physics Research Training Network grant (number 432290) of the Natural Sciences and Engineering Research Council (NSERC), discovery grant (number 241018).

# Bibliography

- Adams, Q E et al. (2014). "Interstitial rotating shield brachytherapy for prostate cancer". In: *Med. Phys.* 41.5, p. 051703.
- Agostinelli, S et al. (2003). "Geant4 - a simulation toolkit". In: *Nucl. Inst. and Meth. in Phys. Research* 506.3, pp. 250–303.
- Barendsen, G W and H M D Walter (1963). "Effect of different ionizing radiations on human cells in tissue cultures. III. Experiments with cyclotron accelerated particles and deuterons". In: *Radiat. Res.* 18, pp. 106–19.
- Beaulieu, L et al. (2012). "Report of the Task Group 186 on model-based dose calculation methods in brachytherapy beyond the TG-43 formalism: Current status and recommendations for clinical implementation". In: *Med. Phys.* 39.10, pp. 106–19.
- Bernal, M A et al. (2015). "Track structure modeling in liquid water: a review of the Geant4-DNA very low energy extension of the Geant4 Monte Carlo simulation toolkit". In: *Phys. Med.* 31, pp. 861–74.
- Brenner, David J (2008). "The linear-quadratic model is an appropriate methodology for determining isoeffective doses at large doses per fraction". In: *Semin. Radiat. Oncol.* 18, pp. 234–9.
- Brenner, David J et al. (1999). "Clinical relative biological effectiveness of low-energy x-rays emitted by miniature x-ray devices". In: *Phys. Med. Biol.* 44, pp. 323–33.
- Chiriotti, S et al. (2014). "Monte Carlo tools to supplement experimental microdosimetric spectra". In: *Radiat. Prot. Dosimetry* 161.1-4, pp. 454–8.
- Enger, Shirin A, Darrell R Fisher, and Ryan T Flynn (2013). "Gadolinium-153 as a brachytherapy source". In: *Phys. Med. Biol.* 58.4, pp. 957–64.
- Grimm, R and T Kaftal (1996). "Gamma radiography using selenium-75". In: *Insight* 38.9.

- Grindborg, J E and P Olko (1997). "A comparison of measured and calculated yD-values in the nanometre region for photon beams in dosimetry: an interdisciplinary approach". In: *12th Symp. on Microdosimetry*. Ed. by D T Goodhead, P O'Neill, and H G Menzel. Cornwall: Hartnolls Ltd, pp. 387–90.
- Grindborg, J E, G Samuelsson, and L Lindborg (1995). "Variance-Covariance Measurements in Photon Beams for Simulated Nanometre Objects". In: *Radiat. Prot. Dosimetry* 61.1-3, pp. 193–8.
- Hugtenburg, R P, Z Chaoui, and J E Pattison (2007). "Microdosimetric event distributions in sub-cellular volumes with a general purpose Monte Carlo code". In: *Nucl. Instrum. Meth. A* 580.1, pp. 157–60.
- IAEA (2008). *Relative Biological Effectiveness in Ion Therapy*. Tech. rep. International Atomic Energy Agency, Vienna, Austria.
- ICRP (2007). "The 2007 recommendations of the International Commission on Radiological Protection. ICRP publication 103". In: *Ann. ICRP* 37.2-4, pp. 1–332.
- ICRU (1983). "Microdosimetry". In: *ICRU Report* 36.
- Incerti, S et al. (2010). "Comparison of GEANT4 very low energy cross section models with experimental data in water". In: *Med. Phys.* 37, pp. 4692–708.
- Incerti, S et al. (2013). "Energy deposition in small-scale targets of liquid water using the very low energy electromagnetic physics processes of the Geant4 toolkit". In: *Nucl. Inst. and Meth. in Phys. Research B* 306, pp. 158–64.
- Kellerer, A M (1985). *Fundamentals of microdosimetry*. Harcourt Brace Jovanovich.
- Kirkby, C et al. (2013). "RBE of kV CBCT radiation determined by Monte Carlo DNA damage simulations". In: *Phys. Med. Biol.* 58.16, pp. 5693–704.
- Lillhok, J E et al. (2007). "Nanodosimetry in a clinical neutron therapy beam using the variance-covariance method and Monte Carlo simulation". In: *Phys. Med. Biol.* 52.16, pp. 4953–66.
- Lindborg, L and J E Grindborg (1997). "Nanodosimetry results and radiotherapy beams: a clinical application?" In: *Radiat. Prot. Dosimetry* 70.1-4, pp. 541–6.

- Lindborg, Lennart et al. (2013). "Lineal energy and radiation quality in radiation therapy: model calculations and comparison with experiment". In: *Phys. Med. Biol.* 58.1, pp. 3089–105.
- (2015). "Nanodosimetry and RBE values in radiotherapy". In: *Radiat. Prot. Dosimetry* 166.1-4, pp. 339–42.
- MacPherson, Miller S and Jerry J Battista (1998). "Radioactivity measurements of ytterbium-169 brachytherapy sources". In: *Australas. Phys. Eng. Sci. Med.* 21.1, pp. 18–23.
- Mason, D L et al. (1992). "Ytterbium-169: calculated physical properties of a new radiation source for brachytherapy". In: *Med. Phys.* 19.3, pp. 695–703.
- Meigooni, A S and R Nath (1992). "A comparison of radial dose functions for  $^{103}\text{Pd}$ ,  $^{125}\text{I}$ ,  $^{145}\text{Sm}$ ,  $^{241}\text{Am}$ ,  $^{169}\text{Yb}$ ,  $^{192}\text{Ir}$ , and  $^{137}\text{Cs}$  brachytherapy sources". In: *Int. J. Radiat. Oncol. Biol. Phys.* 22.5, pp. 1125–30.
- Nikjoo, H et al. (1991). "Energy deposition in small cylindrical targets by monoenergetic Electrons". In: *Int. J. Radiat. Biol.* 60.5, pp. 739–56.
- (1994). *Energy Deposition by monoenergetic electrons in small cylindrical targets*.
- Nikjoo, H et al. (2011). "A database of frequency distributions of energy depositions in small-size targets by electrons and ions". In: *Radiat. Prot. Dosimetry* 143.2-4, pp. 145–51.
- Pater, P et al. (2016). "Event-by-event electron spectra in cells for RBE calculations". In: *Phys. Med. Biol.*
- Poludniowski, G et al. (2004). "*SpeckCalc*: a program to calculate photon spectra from tungsten anode x-ray tubes". In: *Phys. Med. Biol.* 54.19, N433.
- Rossi, H H and M Zaider (1995). *Microdosimetry and its applications*. Berlin: Springer-Verlag.
- Scalliett, P and A Wambersie (1987). "Which RBE for iodine 125 for clinical application". In: *Radiotherapy and Oncology* 9, pp. 221–30.
- Stewart, R D et al. (2002). "Microdosimetric properties of ionizing electrons in water: a test of the PENELOPE codesystem". In: *Phys. Med. Biol.* 47.1, pp. 79–88.

- Thames, H D and J H Hendry (1987). *Fractionation in radiotherapy*. New York: Taylor and Francis.
- Wambersie, A and J Dutreix (1971). "Problèmes dosimétriques posés par la détermination de l'EBR dans un large domaine d'énergie". In: *Biophysical Aspects of Radiation Quality*, pp. 261–72.
- White, S A et al. (2016). "A comparison of the relative biological effectiveness of low energy electronic brachytherapy sources in breast tissue: a Monte Carlo study". In: *Phys. Med. Biol.* 61, pp. 383–99.
- Zeitz, L et al. (1977). "Determination of RBE of soft X-rays". In: *Radiat. Res.* 70, pp. 552–63.
- Zellmer, D L, M T Gillin, and J F Wilson (1992). "Microdosimetric single event spectra of Ytterbium-169 compared with commonly used brachytherapy sources and teletherapy beams". In: *Radiat. Res.* 23.3, pp. 627–32.

# Paper 2

# Practical Aspects of $^{153}\text{Gd}$ as a Radioactive Source for Use in Brachytherapy

Gabriel Famulari, Tomas Urlich, Andrea Armstrong, Shirin A. Enger

## Abstract

**Purpose:** Gadolinium-153 ( $^{153}\text{Gd}$ ) has been proposed as a potential novel source for high dose rate (HDR) brachytherapy. The goal of this study is to investigate the production, purification and immobilization techniques for  $^{153}\text{Gd}$  through a series of experiments performed at McMaster Nuclear Reactor (MNR). In this work, the viability of the direct production pathway, through irradiation of enriched  $^{152}\text{Gd}$ , was examined.

**Materials and Methods:** To determine the effective thermal neutron cross section for the  $^{152}\text{Gd}(n,\gamma)$  reaction,  $^{152}\text{Gd}$  targets (obtained from  $^{152}\text{Gd}$  enriched  $\text{Gd}_2\text{O}_3$ ) were irradiated during 2 h and counted on a high purity germanium detector (HPGe). These results were used to predict the maximum achievable specific activity of  $^{153}\text{Gd}$ . The efficiency of a Eu/Gd separation technique via europium sulfate precipitation through a zinc column was tested. The loading capacity for Gd was evaluated for a series of sorbents with high affinity for lanthanides (Dowex®50WX8-400, AG®50W-X2, AG®50W-X12).

**Results and Discussion:** From the net counts at 97.4 and 103.2 keV, the effective thermal neutron cross section was  $394 \pm 16$  b and  $438 \pm 18$  b, respectively, resulting in a final value of  $416 \pm 29$  b. Based on this value, the maximum predicted specific activity of  $^{153}\text{Gd}$  was about 70 Ci/g  $^{152}\text{Gd}$ , after about 2-3 months of full-day irradiation. There would be very little benefit in terms of maximum specific activity from a higher neutron flux than that at MNR. The Eu/Gd separation technique via europium sulfate precipitation through a zinc column was demonstrated to be effective at removing large quantities of Eu from small amounts of Gd, but additional purification through

high pressure liquid chromatography or electrodeposition on a solid wire may still be required. Dowex®50WX8-400 had the largest loading capacity for Gd ( $131 \pm 8$  mg/g sorbent) and can be an effective method to load liquid  $^{153}\text{Gd}$  into a capsule.

**Conclusion:** The major advantage of producing  $^{153}\text{Gd}$  through the direct production pathway is the possibility to irradiate pre-sealed pellets of enriched  $^{152}\text{Gd}$ , thereby removing the need to perform chemical separation in hot cells with large quantities of long-lived, high gamma emission radio-impurities. However, chemical purification may still be required to improve the radionuclidic purity of the source, in which case the  $^{153}\text{Gd}$  will be isolated as an aqueous solution, and can be loaded onto a solid substrate for encapsulation.

# 1 Introduction

## 1.1 Current status of brachytherapy

Brachytherapy is a cancer treatment modality in which encapsulated radiation sources are placed directly into, or near, localized tumours, giving a high radiation dose to the malign volume while maintaining a low dose to surrounding healthy tissues. Aiming at effective tumour sterilization with manageable side effects, the importance of brachytherapy is increasing in cancer therapy. Iridium-192 ( $^{192}\text{Ir}$ ,  $t_{1/2} = 72$  days,  $E_{\gamma,avg} = 360$  keV) is a widely used gamma isotope for high dose rate (HDR) brachytherapy. HDR brachytherapy combines remote afterloader technology with high source strength and short treatment times.  $^{192}\text{Ir}$  is criticized due to the high-energy gamma emissions, which require the treatment room to be sufficiently shielded. Additionally, the spectrum of  $^{192}\text{Ir}$  is inherently contaminated with beta emission, which is not accounted for in clinical treatment planning system. The beta energy spectrum of  $^{192}\text{Ir}$  has a mean value of about 200 keV and a maximum value of about 670 keV.

The emission of relatively high-energy gamma and the beta contamination justifies the search for a lower-energy photon-emitting source with comparable dose distribution and dose rate as  $^{192}\text{Ir}$ , but with longer half-life and less beta contamination.

## 1.2 Geometrical constraints for brachytherapy sources

The  $^{192}\text{Ir}$  source used in HDR brachytherapy is a small line source, enclosed in a stainless steel capsule, welded to the end of a flexible drive cable. The outer dimensions of the sources vary between 0.6 and 1.6 mm in diameter and 3.6 to 6 mm in length, depending on the model (AAPM and ESTRO, 2012). The active cores typically range between 0.3 and 1 mm in diameter and 1.3 and 5 mm in length. The source needs to be able to navigate through transfer tubes of various designs, each aimed for specific applicators or catheters, which are inserted directly into the patient. The outer diameter of the transfer tubes and the catheters is typically restricted to at most 2 mm.

HDR brachytherapy delivers a dose of at least 12 Gy/h, and requires automatic remote afterloading due to the high activity of the source (ICRU, 1985). Due to the geometrical constraints imposed by the delivery system, it is necessary to produce a source with a very high specific activity.

### 1.3 Development of a new brachytherapy source

Gadolinium-153 ( $^{153}\text{Gd}$ ,  $t_{1/2} = 240.4$  days,  $E_{\gamma,avg} = 60$  keV) has theoretically been investigated as a brachytherapy source for use in intensity modulated brachytherapy (Enger, Fisher, and Flynn, 2013; Adams et al., 2014).  $^{153}\text{Gd}$  can be produced either by the direct production route, via neutron activation of the lighter gadolinium isotope  $^{152}\text{Gd}$ , or by the indirect production route, through neutron bombardment of natural europium (47.8 %  $^{151}\text{Eu}$ , 52.2 %  $^{153}\text{Eu}$ ). In the indirect production route,  $^{151}\text{Eu}$  undergoes one neutron capture event to form  $^{152}\text{Eu}$ , decays (via beta decay) to  $^{152}\text{Gd}$ , and then undergoes a second neutron capture event to produce  $^{153}\text{Gd}$ .

One of the key challenges associated with developing  $^{153}\text{Gd}$  or any new brachytherapy source is the procurement and encapsulation of the radioisotopes. The radioisotope component of a brachytherapy source is generally introduced either in the form of a solid wire, as in the case of  $^{192}\text{Ir}$ , or as a solid substance that has been impregnated with a liquid radioisotope and allowed to dry, as is done for iodine-125 ( $^{125}\text{I}$ ,  $t_{1/2} = 60$  days,  $E_{\gamma,avg} = 28$  keV). The appropriate method depends on the chemical form in which the radioisotope is obtained, and is directly influenced by the production route that is used to generate the radioisotope.

Regardless of the production route of  $^{153}\text{Gd}$ , after completed neutron irradiation, chemical purification of  $^{153}\text{Gd}$  is required to remove most of the long-lived europium radioisotopes  $^{152}\text{Eu}$  ( $t_{1/2} = 12.7$  y),  $^{154}\text{Eu}$  ( $t_{1/2} = 8.5$  y) and  $^{155}\text{Eu}$  ( $t_{1/2} = 4.8$  y) (Case, Acree, and Cutshall, 1967; Ramey, 1988; Johnsen et al., 2013). This has an important practical ramification, as the  $^{153}\text{Gd}$  will be obtained as an aqueous solution, rather than as a solid pellet or wire. Attempting to form the  $^{153}\text{Gd}$  solution into a wire or solid

pellet would likely result in the dispersion of radioactive contamination throughout the work area, and may therefore be not viable from a radiation safety standpoint.  $^{125}\text{I}$  brachytherapy seeds contain  $^{125}\text{I}$  that is adsorbed on spheres of silver metal, ceramics, or anion exchange resins; while none of these materials is appropriate for adsorbing  $^{153}\text{Gd}$ , a cationic metal, the concept still holds.

## 1.4 Objectives

The aim of this study is to take an immobilization approach for production of the radioisotope  $^{153}\text{Gd}$  as a brachytherapy source through a series of experiments performed at McMaster Nuclear Reactor (MNR). Research toward  $^{153}\text{Gd}$  sources will focus on developing a means of immobilizing the radioisotope on a solid support that can subsequently be encapsulated in medical grade titanium tubing to produce a brachytherapy source.

## 2 Materials and Methods

The development of new brachytherapy sources involves four key steps. First, an appropriate radioisotope must be selected. Next, a facility capable of producing the radioisotope must be identified. Following this, a method must be developed to immobilize and encapsulate the radioisotope in a device that is an appropriate size, shape, and material for use in brachytherapy. Finally, the source must be tested for its compliance with standards set out in nuclear regulatory documents such as the International Standards Organization's ISO 2919:2012 (ISO, 2012).

In this study we will investigate production of  $^{153}\text{Gd}$  as a brachytherapy source at MNR, a 5 MW open-pool nuclear reactor that is the most powerful university-based research reactor in Canada. The reactor is a multi-purpose research facility, and has a number of irradiation sites with different characteristics that allows the production of micro-Curies of radioactivity for method development experiments, multi-Curie batches of radioisotopes for commercial distribution, and everything in between. The

nuclear reactor is capable of producing  $^{153}\text{Gd}$ . The radioactive material will be handled at McMaster University’s High Level Laboratory Facility (HLLF) located adjacent to MNR. HLLF is a suite of state-of-the-art nuclear research laboratories that is unique in Canada, in that it is licensed as a nuclear facility by the Canadian Nuclear Safety Commission (CNSC). HLLF provides heavily shielded “hot cells” for safe handling of large quantities of radioisotopes, and analytical tools such as an automated High Performance Liquid Chromatography instrument equipped with a radiometric detector that enables the isolation of particular radioisotopes from complex chemical matrices.

## 2.1 Thermal neutron cross section of $^{153}\text{Gd}$

In order to assess the effective cross-section of the  $^{152}\text{Gd}$  neutron capture reaction in  $^{157}\text{Gd}$  depleted materials, a small quantity (10 mg) of isotopically enriched  $\text{Gd}_2\text{O}_3$  (enriched to 30.6 %  $^{152}\text{Gd}$ ) was purchased from Trace Sciences International. The relative abundance of the isotopes and the impurities present are provided in Table 1. A Gd stock solution was prepared in order to produce small samples of the substance with precisely known masses of Gd. The oxide powder was dissolved in 30  $\mu\text{l}$  of 1 M HCl and diluted to 1 ml with distilled water in a stock vial. Four 50  $\mu\text{l}$  samples of the solution were pipetted into polyethylene containers and were air-dried. Each sample contained 0.132 mg  $^{152}\text{Gd}$ . In addition, four samples of natural  $\text{Cr}_2\text{O}_3$  (Sigma-Aldrich) were weighed and placed in polyethylene containers. These samples were placed alongside the Gd samples to provide an estimate of the thermal flux in each irradiation site.

Isotope	Abundance (%)	Impurities	Abundance (ppm)
$^{152}\text{Gd}$	30.6	Eu	7000
$^{154}\text{Gd}$	9.3	Sm	11000
$^{155}\text{Gd}$	18.1		
$^{156}\text{Gd}$	14.8		
$^{157}\text{Gd}$	8.6		
$^{158}\text{Gd}$	11.0		
$^{160}\text{Gd}$	7.6		

TABLE 1: The relative abundance of isotopes and impurities in the  $^{152}\text{Gd}$  enriched  $\text{Gd}_2\text{O}_3$ .

The samples were placed in capsules for irradiation in the reactor core. The capsules were irradiated for 2 hours, at an operating power of 5 MW and approximate neutron flux of  $10^{13} \text{ n cm}^{-2} \text{ s}^{-1}$ . The samples were allowed to decay overnight, and were then removed from the capsules. The cool-down period permits the decay for all short-lived activation products generated during reactor irradiation.

The gammas from the samples were counted using a Be-window high purity germanium (HPGe) detector (Aptec). The samples were placed at 300 mm away from the detector surface (position 9) during 10 min. The results were analysed using the software GammaVision (ORTEC). The detection efficiency ( $\eta$ ) as a function of energy for the position selected is shown in Figure 1. The detection efficiencies were 0.122 % and 0.118 % at the 97.4 and 103.2 keV lines, respectively, corresponding to the most significant gamma peaks of  $^{153}\text{Gd}$ . The activity (Bq) was determined by dividing the counts per second (cps) values measured by the detector by the detection efficiency ( $\eta$ ) and the absolute gamma intensity ( $I_\gamma$ ) for the given energy ( $E_\gamma$ ). Since  $^{153}\text{Sm}$  ( $t_{1/2} = 46.7 \text{ h}$ ), which, similarly to  $^{153}\text{Gd}$ , decays to excited levels of  $^{153}\text{Eu}$  and therefore has significant gamma peaks at the exact same energies as  $^{153}\text{Gd}$ , were expected from the irradiation of the targets (Holden, 1986), the samples were counted again 47 h later. Based on the difference in the counts and the half-life of  $^{153}\text{Sm}$ , the  $^{153}\text{Sm}$  component of the measured peaks were eliminated from the counts. This ensures that the measured activity is restricted to  $^{153}\text{Gd}$ . An effective cross section for the  $^{152}\text{Gd}$  neutron capture reaction was determined as follows:

$$\sigma = \frac{Aw}{m_\alpha N_A \phi (1 - e^{-\lambda t_i}) e^{-\lambda t_d}}, \quad (1)$$

where  $A$  is the activity,  $m_\alpha$  is the mass of the daughter isotope,  $w$  is the atomic weight of the element,  $N_A$  is Avogadro's number,  $\phi$  is the thermal neutron flux,  $\lambda$  is the decay constant of the radioisotope produced,  $t_i$  is the irradiation time and  $t_d$  is the time since the end of irradiation.

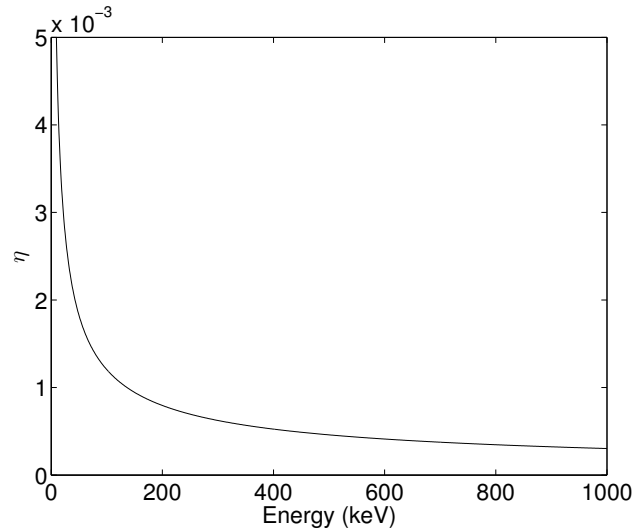


FIGURE 1: Efficiencies of the HPGe detector as a function of energy at position 9.

## 2.2 Achievable specific activity of $^{153}\text{Gd}$

In this study, the direct production route was evaluated numerically. A system of 21 ordinary differential equations was used to describe variations in the quantities of the various isotopes (both radioactive and stable) created during the production of  $^{153}\text{Gd}$  (see appendix). The specific activity of the radioisotopes, defined here as the activity of the radionuclide per unit mass of the stable precursor  $^{152}\text{Gd}$ , produced by the irradiation of the enriched  $^{152}\text{Gd}$  target was determined as a function of irradiation time. A neutron flux of  $2.5 \times 10^{13} \text{ n cm}^{-2} \text{ s}^{-1}$  was chosen to represent the value for the neutron flux for an irradiation site at MNR. The effect of neutron flux on the maximum specific activity of  $^{153}\text{Gd}$  was also examined. Half-lives were taken from the Lund/LBNL nuclear data library (Chu, Ekstrom, and Firestone, 1999). Empirical thermal neutron capture cross sections were taken from the Atlas of Neutron Capture Cross Section (Kopecky et al., 1999). The effective thermal neutron cross section measured in section II.I was included in the analysis. The parameters used for the simulation are shown in the appendix. The analysis was performed with MATLAB R2014a. The system was numerically integrated using the Euler method with a step size of 0.01 h. A continuous irradiation time was considered, as well as a typical irradiation schedule at MNR (14 h per day, 5 days per week, 50 weeks per year).

## 2.3 Chemical purification of $^{153}\text{Gd}$

MNR is currently not licensed to produce  $^{153}\text{Gd}$  from the indirect production method, due to the large amounts of long-lived radioactive Eu waste products (16 Ci Eu waste/1 Ci Gd produced) that must be chemically processed into a suitable form for disposal (Ramey, 1988). However, the processing experiments that are required for the purification of  $^{153}\text{Gd}$  can be tested using non-radioactive isotopes of the particular elements and small quantities of radioactive tracers.  $^{159}\text{Gd}$  is an ideal radioactive label for chemical separation experiments, since it has the same chemical properties as  $^{153}\text{Gd}$ , but a short half-life ( $t_{1/2} = 18.5$  h).  $^{159}\text{Gd}$  is produced by neutron irradiation of  $^{158}\text{Gd}$  targets.

A stock solution was prepared using  $\text{Gd}_2\text{O}_3$  enriched to 97.9 %  $^{158}\text{Gd}$  (Sigma-Aldrich) dissolved in HCl and distilled water. A 200  $\mu\text{l}$  sample containing 4 mg stable Gd was pipetted into a quartz ampoule. The sample was dried, sealed, wrapped in aluminum foil and encapsulated. The capsule was irradiated for 14 hours at an approximate neutron flux of  $10^{13} \text{ n cm}^{-2} \text{ s}^{-1}$ . The sample was allowed to decay overnight and was then removed from the capsule. The sample of radioactive  $^{159}\text{Gd}$  was dissolved in 300  $\mu\text{l}$  of 0.1 M HCl and diluted to 1 ml with distilled water.

In order to more accurately assess the Eu/Gd separation process, a solution was prepared using 198.4 mg natural  $\text{Eu}_2\text{O}_3$  (containing 171.34 mg natural Eu) and 500  $\mu\text{l}$  of the  $^{159}\text{Gd}$  stock solution (containing 2 mg Gd) in methanol. The Gd was chemically separated according to a previously published Eu/Gd separation technique via europium sulfate precipitation through a zinc column (Johnsen et al., 2013). The technique involves reducing Eu(III) to Eu(II), the latter of which precipitates, and filtering off the Gd. The percentage of Gd recovered could be quantifiable due to the presence of  $^{159}\text{Gd}$ , since a portion of the Gd might co-precipitate with  $\text{EuSO}_4$ . The activity of  $^{159}\text{Gd}$  in solution was measured in the Atomlab<sup>TM</sup> 500 dose calibrator, which had been previously calibrated for  $^{159}\text{Gd}$ , prior and post-separation. The remaining solution was passed through the zinc column a second time to determine whether further separation can be achieved.

The residual Eu mixed in with the Gd was quantified by neutron activation analysis (NAA). A 200  $\mu\text{l}$  sample from the 5 ml solution was irradiated for 30 s through the system at the Centre for Neutron Activation Analysis (CNAA) at MNR. The sample was counted on the HPGe detector for 10 minutes. The sample was placed at 300 mm away from the detector surface (position 9). The count rate was measured at 344.3 keV, corresponding to the most significant gamma peak of  $^{152}\text{Eu}$ . The amount of Eu remaining in the solution was quantified by comparing the count rate of the sample and the count rate for a known mass (1.00 mg) of natural Eu irradiated for a given time (30 s) through the system and counted at the same distance from the detector.

## 2.4 Sorption of Gd on solid supports

A non-active Gd stock solution was prepared from 2.2 g  $\text{Gd}_2\text{O}_3$  enriched to 97.9 %  $^{158}\text{Gd}$  (Sigma-Aldrich) dissolved in 100  $\mu\text{l}$  of 1 M HCl, heated until dry, and subsequently dissolved in 9 ml of distilled water. A  $^{159}\text{Gd}$  sample was prepared in the same manner as in section 2.3 and dissolved in 400  $\mu\text{l}$  of 0.25 M HCl. A 300  $\mu\text{l}$  sample of the  $^{159}\text{Gd}$  solution was added to 4 ml of the non-radioactive stock solution and 700  $\mu\text{l}$  of distilled water.

A series of sorbents (Dowex®50WX8-400 ion-exchange resin (Sigma Aldrich), analytical grade AG®50W-X2 cation exchange resin (Bio-Rad), analytical grade AG®50W-X12 cation exchange resin (Bio-Rad)) that have high loading capacity for Gd were weighed and packed into Pasteur pipettes. The sorbents were compacted into a cylindrical volume with approximately 20 mm height and 6 mm diameter. The mass of sorbents used are listed in table 4. A 300  $\mu\text{l}$  sample of the  $^{159}\text{Gd}$  solution was pipetted onto each sorbent and the sorbent was rinsed with water to check for breakthrough of the  $^{159}\text{Gd}$ . More  $^{159}\text{Gd}$  solution was added in small portions, checking for breakthrough after each addition. The loading capacity of each material for Gd (mg Gd per g sorbent) was determined by quantifying the amount of  $^{159}\text{Gd}$  loaded onto the sorbent and the amount remaining in the solution. The activity of  $^{159}\text{Gd}$  in the sorbent and the

eluate were measured in the dose calibrator.

The amount of Gd in each sample was quantified by NAA. A 10  $\mu\text{l}$  sample from the non-active stock solution was irradiated for 10 min through the system. The sample was counted on the HPGe detector for 10 min. The sample was placed at 300 mm away from the detector surface (position 9). The count rate was measured at 363.5 keV, corresponding to the most significant gamma peak of  $^{159}\text{Gd}$ . The amount of Gd in the solution was quantified by comparing the count rate of the sample and the count rate for a known mass (2.00 mg) of natural Gd irradiated for a given time (10 min) through the system and counted at the same distance from the detector.

## 2.5 Sintering of $\text{Gd}_2\text{O}_3$

Finally, the physical properties of  $\text{Gd}_2\text{O}_3$  were examined. In order to obtain the density of  $\text{Gd}_2\text{O}_3$  as obtained from commercial suppliers, a sample of natural  $\text{Gd}_2\text{O}_3$  was tightly packed into a 0.40 ml volume inside the barrel of a pre-weighed 1 ml syringe, then weighed. A second sample of  $\text{Gd}_2\text{O}_3$  was heated overnight in a muffle furnace at 1000  $^\circ\text{C}$ , the highest achievable temperature for the furnace, to see if it began to sinter (become compacted). The density of the heated sample was then measured in an identical fashion. The change in density was determined in order to quantify the benefit associated with sintering.

## 3 Results and Discussion

### 3.1 Thermal neutron cross section of $^{153}\text{Gd}$

The experimental results from the irradiation of the  $\text{Cr}_2\text{O}_3$  samples are shown in Table 2. From the net count rates at 320.1 keV, the activity of  $^{51}\text{Cr}$  in the samples was determined and the thermal neutron flux for each irradiation site was estimated accordingly. These flux values were used to determine the effective cross section for  $^{152}\text{Gd}$ .

Isotope	$E_\gamma$ (keV)	$I_\gamma$ (%)	$\eta$ (%)	$\sigma$ (b)	Net count rate (cps)	A ( $\mu\text{Ci}$ )	$\phi$ ( $\text{n cm}^{-2} \text{s}^{-1}$ )
$^{51}\text{Cr}$	320.1	9.89	0.060	15.9	169.75	76.1	$1.54 \times 10^{13}$
					124.45	55.8	$1.10 \times 10^{13}$
					172.54	77.3	$1.48 \times 10^{13}$
					171.29	76.7	$1.46 \times 10^{13}$

TABLE 2: Determination of thermal flux from the irradiation of four samples of natural  $\text{Cr}_2\text{O}_3$ .

Figure 2 shows the measured HPGe energy spectrum of the Gd sample 16 h and 63 h after the completion of irradiation. By subtracting the  $^{153}\text{Sm}$  contribution from the count rate for the gamma peaks at 97.4 and 103.2 keV, the net count rates for  $^{153}\text{Gd}$  were obtained. The summary for the experimental results are shown in Table 3. From the net counts at 97.4 and 103.2 keV, we obtained  $394 \pm 16$  b and  $438 \pm 18$  b, respectively. The effective neutron capture cross section for  $^{152}\text{Gd}$  was determined from the weighted mean of the two values, resulting in a final value of  $416 \pm 29$  b. The uncertainties are largely dominated by the statistical variation between the various samples. Since the thermal neutron capture cross section is not measured directly, the accuracy of the value is highly dependent on the accuracy of the gamma intensity, detector efficiency, half-life and neutron flux (or cross section of sample used to determine neutron flux). If the values used by the experimenter are significantly different from those presently recommended in the literature, the cross section data will be directly affected.

Isotope	$E_\gamma$ (keV)	$I_\gamma$ (%)	$\eta$ (%)	$\phi$ ( $\text{n cm}^{-2} \text{s}^{-1}$ )	Net count rate (cps)	A ( $\mu\text{Ci}$ )	$\sigma$ (b)
$^{153}\text{Gd}$	97.4	29.5	0.122	$1.54 \times 10^{13}$	279.3	21.0	404
				$1.10 \times 10^{13}$	197.6	14.8	398
				$1.48 \times 10^{13}$	269.6	20.2	404
				$1.46 \times 10^{13}$	243.7	18.2	370
	103.2	22.0	0.118	$1.54 \times 10^{13}$	229.5	23.9	459
				$1.10 \times 10^{13}$	155.3	16.2	436
				$1.48 \times 10^{13}$	213.1	22.2	443
				$1.46 \times 10^{13}$	196.1	20.4	414

TABLE 3: Determination of cross section for  $^{152}\text{Gd}(n,\gamma)$  reaction.

The achievable specific activity of any radioisotope produced by neutron activation in a highly thermalized flux is proportional to the thermal neutron capture cross section ( $\sigma$ ) of its precursor, as well as the neutron flux ( $\phi$ ) of the irradiation site. Previously,

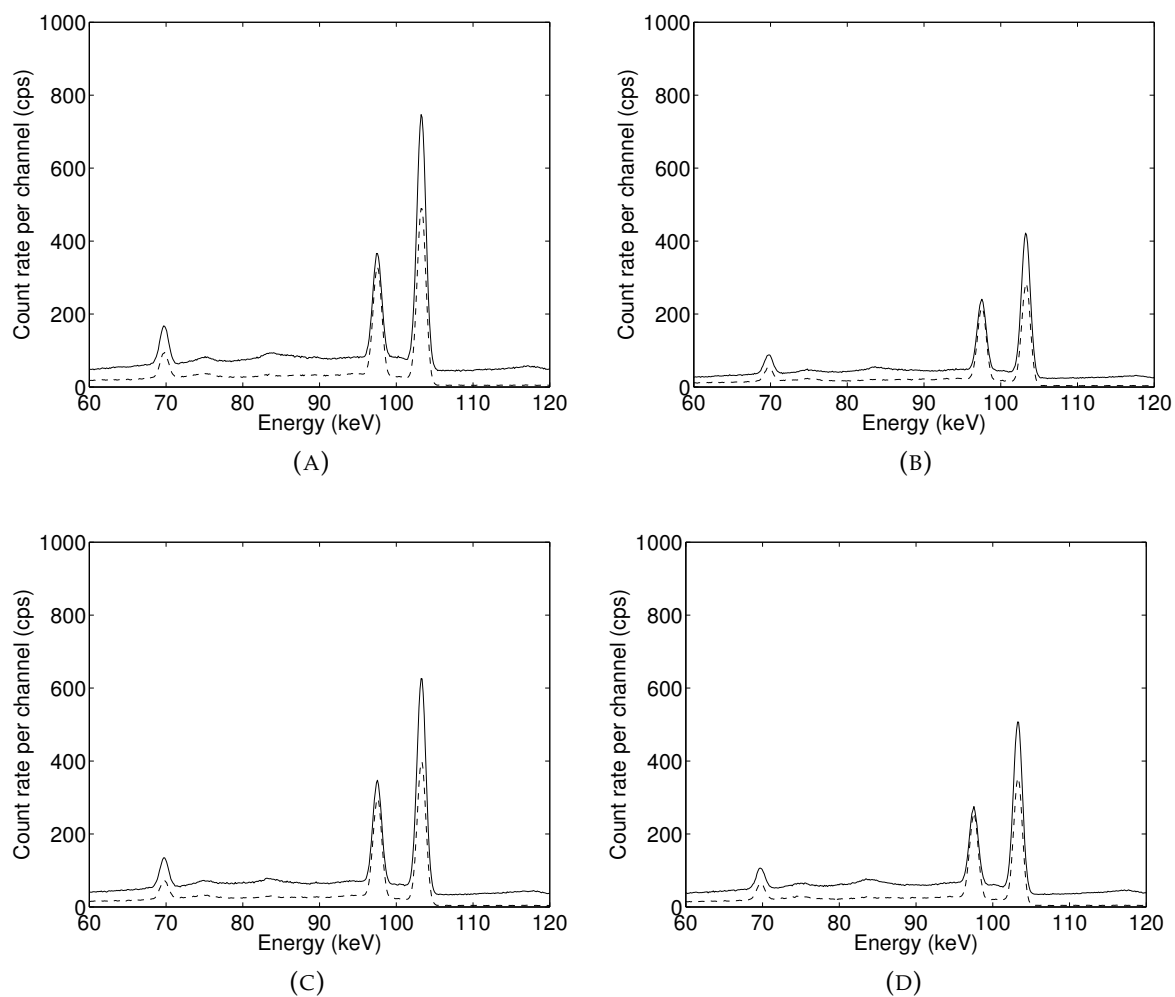


FIGURE 2: Energy spectra from the gross count rates of the four irradiated Gd samples (a,b,c,d) in the energy region of the  $^{153}\text{Gd}$  gamma peaks. Upper (solid line) and lower (dotted line) spectra were obtained 16 h and 63 h after the end of irradiation, respectively. The net counts were obtained by subtracting the background counts from higher energy from the gross counts.

it was difficult to accurately predict the yield of  $^{153}\text{Gd}$  since conflicting – and significantly different – values were reported in the literature for the  $^{152}\text{Gd}(n,\gamma)$  reaction cross section. The data for  $^{152}\text{Gd}$  is complicated since it has an extremely low abundance (0.2 %) in natural Gd found in terrestrial samples. There were two inconsistent measurements on this reaction at thermal neutron energy,  $1100 \pm 100$  b (Steinnes, 1972),  $735 \pm 10$  b (Heft, 1978) and  $615 \pm 60$  b (Lee et al., 2011).

Steinnes (Steinnes, 1972) performed an activation measurement on a sample of natural Gd and counted the gamma peaks with a NaI detector, which could not resolve

the two significant gamma rays at 97.4 and 103.2 keV. Since Sm impurities were likely present in the Gd sample, the contribution of  $^{153}\text{Sm}$  to both the 97.4 and 103.2 keV lines was wrongly attributed to the counts for  $^{152}\text{Gd}$ , providing an overestimated result for the thermal cross section of  $^{152}\text{Gd}$ . Holden (Holden, 1986) estimated that the cross section for this measurement, corrected for the Sm impurities, was effectively  $894 \pm 300$  b.

Heft (Heft, 1978) performed an activation measurement on a sample of natural Gd and counted the gamma rays at 97.4 keV using a Ge(Li) detector. While this detector could distinguish the two main gamma peaks, the counts were only measured at 97.4 keV to minimize the effect of the Sm impurities (the gamma intensities for  $^{153}\text{Sm}$  decay are 0.8 % at 97.4 keV and 29.2 % at 103.2 keV). However, an absolute intensity of 31.7 % was used, while the current recommended value is 29.5 % Xiaolong, 2010. If we normalize the intensity to 29.5 %, the thermal neutron cross section becomes  $803 \pm 11$  b. While this provides a more precise cross section than Steinnes' revised result, it is nevertheless significantly higher than the one measured in this study.

Recently, Lee (Lee et al., 2011) evaluated a new cross section value of  $615 \pm 60$  b by irradiating pure gadolinium foils with well known isotopic composition, measuring the yield of gammas from the neutron capture for the  $^{158}\text{Gd}(n,\gamma)^{159}\text{Gd}$  reaction, for which the cross section can be determined with much lower uncertainties, and obtained the thermal neutron cross section for  $^{152}\text{Gd}$  by a comparison with the activity measurements of  $^{158}\text{Gd}$ . Their results are nevertheless significantly higher than the ones obtained in this study.

The discrepancy between the values may be due to the neutron irradiation conditions used for the measurements. Ideally, the cross section would be measured in a perfectly thermalized flux, but reactor-produced neutrons contain significant amounts of epithermal, resonance and fast neutrons, which have different cross sections than thermal neutrons. Self-shielding and flux depression during irradiation can also limit the total activity of the sample and the determined cross-section. Alternatively, it may be due to the composition of the material used to make the measurement: natural

---

gadolinium contains  $^{157}\text{Gd}$ , which has the largest thermal neutron cross-section of any stable isotope (255,000 b) (Abdushukurov et al., 2007) and may lower the apparent cross-sections of other isotopes present, including  $^{152}\text{Gd}$ . Finally, the Sm impurities have contributed to substantial errors and incorrectly elevated values in previous cross section measurements.

In the cases where a natural foil was irradiated, there is a significant amount of uncertainty associated with the amount of  $^{152}\text{Gd}$  present in natural Gd, which will introduce error in the published yields. Our values should be more accurate, since we use an enriched sample with a precisely known weight percent of  $^{152}\text{Gd}$ . Natural Eu activates to form Gd-153, and is a common impurity in natural Gd - this would certainly make a cross-section appear larger than it actually is. The significant differences in the values suggest that there is a need for additional data.

The thermal neutron cross-section measured can be used to accurately predict the maximum specific activity of  $^{153}\text{Gd}$  achievable at MNR by the direct production route. It can also be used in conjunction with empirically determined cross-sections for Eu neutron capture reactions to determine the maximum specific activity of  $^{153}\text{Gd}$  produced through irradiation of natural Eu. Finally, these numbers should work equally well for calculating production yields and specific activities at other nuclear reactors, provided the reactor produces a highly thermalized flux of neutrons.

### 3.2 Achievable specific activity of $^{153}\text{Gd}$

The specific activity of the various radioisotopes created in the production of  $^{153}\text{Gd}$  from neutron irradiation on the enriched  $^{152}\text{Gd}$  target were plotted as a function of irradiation time in Figure 3. The maximum predicted specific activity of  $^{153}\text{Gd}$  was about 70 Ci/g  $^{152}\text{Gd}$  (equivalent to 21 Ci/g total Gd), after 1600-2400 h (2-3 months) of continuous irradiation at MNR. According to the current irradiation schedule at MNR (14 h per day, 5 days per week, 50 weeks per year), it would take at least 5 months to obtain the desired optimal activity. Note that since the specific activity is quoted per

unit mass of the stable precursor  $^{152}\text{Gd}$ , this maximum specific activity is valid for both the direct and indirect production routes. The indirect production route can, however, achieve a specific activity roughly twice as high when weighted by the total mass of Gd (Ramey, 1988). Adapting the irradiation time to the schedule of the reactor has a minimal effect on the value of the maximum activity achievable, due to the relatively long half-life of  $^{153}\text{Gd}$  and the relatively high neutron flux.

The maximum specific yield for the process is about 18 Ci/g enriched  $\text{Gd}_2\text{O}_3$ . While the indirect production route yields only 3 Ci/g natural  $\text{Eu}_2\text{O}_3$  (Ramey, 1988), the cost associated with the indirect route is orders of magnitude cheaper. The cost of enriched  $^{152}\text{Gd}$  oxide is \$130 000/g compared to \$2.25/g for natural  $\text{Eu}_2\text{O}_3$ . Further enriching the target will improve the maximum yield, but the cost of production will likely increase as well. Unfortunately, there does not currently exist a  $^{152}\text{Gd}$  target with a higher purity on the market.

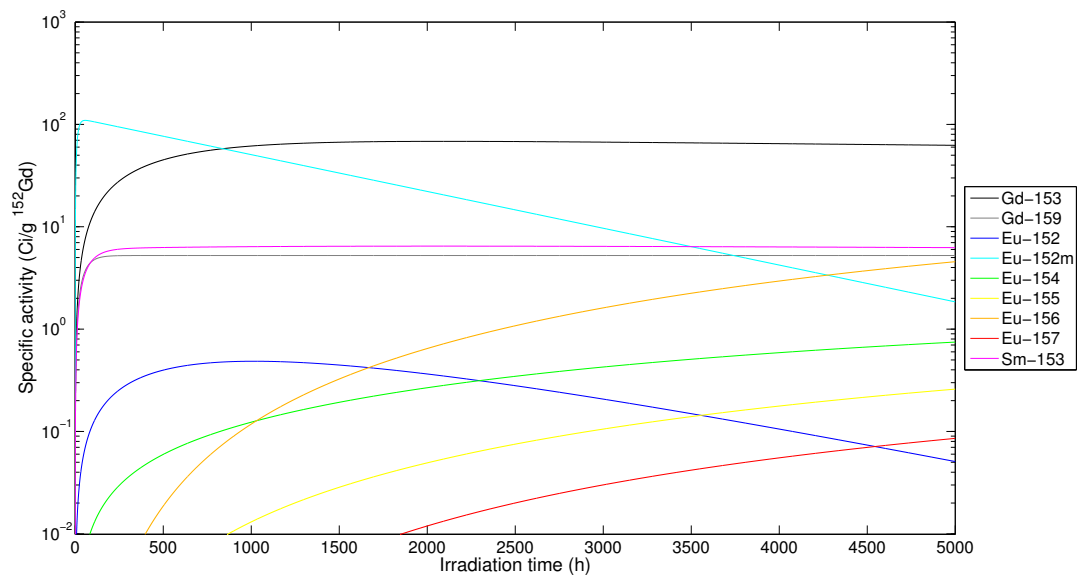
The direct production of  $^{153}\text{Gd}$  produces small quantities of long-lived ( $t_{1/2} > 4$  y) radioisotopes ( $^{152}\text{Eu}$ ,  $^{154}\text{Eu}$ ,  $^{155}\text{Eu}$ ), which could not be eliminated by chemical separation techniques if the  $^{152}\text{Gd}$  target is encapsulated prior to irradiation. Both  $^{152}\text{Eu}$  and  $^{154}\text{Eu}$  emit photons in the 120-1400 keV range, while  $^{155}\text{Eu}$  emits photons in the 45-105 keV range. The long-lived Eu impurities contribute to about 1 % of the total activity of the source for the irradiation time required to obtain the optimal  $^{153}\text{Gd}$  specific activity. The other impurities can be eliminated by allowing the sample to decay for a few days after irradiation. The joint AAPM/ESTRO TG-167 report (Nath et al., 2016) conservatively recommends that radioimpurities be minimized to such levels that their dosimetric contributions over the range of clinically relevant distances in the vicinity of the source should be less than 5 % of the dosimetric contributions of the primary radionuclide. Since the dosimetric influence of the contaminating radionuclides based on their half-lives and emission energies have not yet been investigated, through experiments or simulations, it is not possible to determine whether or not the direct production of  $^{153}\text{Gd}$  using pre-sealed pellets of  $^{152}\text{Gd}$  enriched  $\text{Gd}_2\text{O}_3$  could potentially be a viable production pathway. If the amount of long-lived Eu impurities is deemed too high by

medical physicists and radiation safety experts, additional purification steps would be required to improve the radionuclidic purity. The chemical processing steps must then be conducted in radiological hot cells.

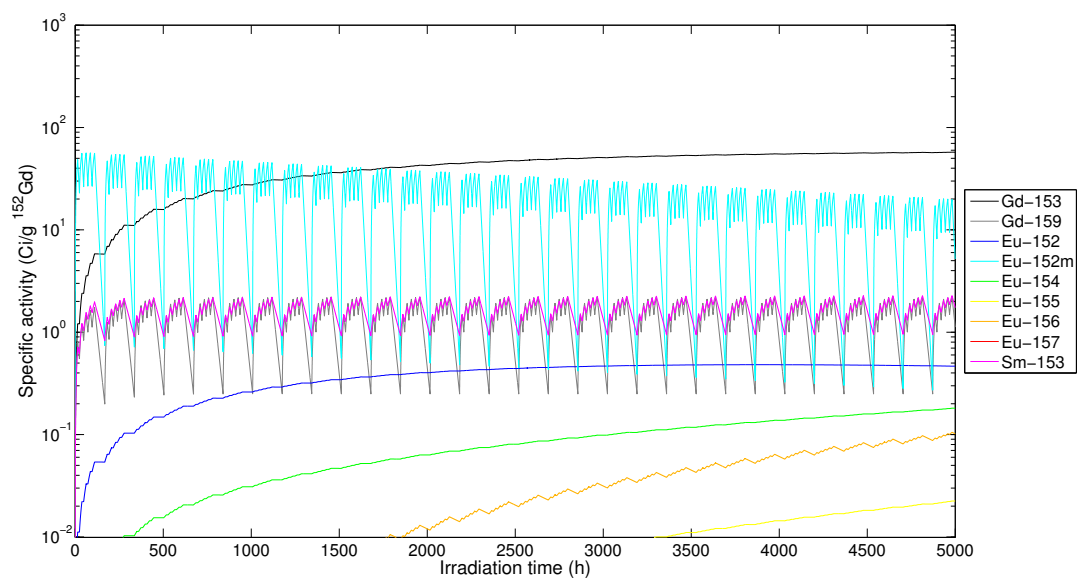
Figure 4 show the effect of neutron flux on the maximum achievable specific activity of  $^{153}\text{Gd}$ . At low neutron flux values ( $< 10^{14} \text{ n cm}^{-2} \text{ s}^{-1}$ ), the maximum achievable specific activity increases linearly with neutron flux, and is also limited by the non-ideal reactor schedule when compared to continuous irradiation conditions. However, at high neutron flux values ( $> 10^{14} \text{ n cm}^{-2} \text{ s}^{-1}$ ), the specific activity attainable reaches a plateau value (72 Ci/g  $^{152}\text{Gd}$ ), which is then not affected by the reactor schedule. A higher neutron flux than that at MNR does not significantly increase the maximum achievable specific activity, since greater amounts of  $^{154}\text{Gd}$  are produced without a significant increase in  $^{153}\text{Gd}$ .  $^{153}\text{Gd}$  has a very large cross-section (20,000 b), hence, irradiation at a very high flux would rapidly lead to nuclear burn-out of the desired isotope in favor of the heavier isotope. Based on these observations, the authors concluded that there is very little benefit in terms of maximum specific activity from a higher neutron flux, or optimal irradiation schedules, for the production of  $^{153}\text{Gd}$ . The conditions of the irradiation site will, however, have an effect on the irradiation time required to attain this specific activity.

### 3.3 Chemical purification of $^{153}\text{Gd}$

The Eu/Gd separation technique via europium sulfate precipitation through a zinc column removed up to 97.5 % of the Eu from the mixed Gd/Eu solution (167.09 mg out of 171.34 mg), with a Gd recovery yield of 88 % (1.76 mg out of 2 mg). A second separation step through the zinc column did not filter any additional Eu. The results agree very well with previous Gd target processing experiments (Johnsen et al., 2013). This technique can certainly improve the purity of the mixed Gd/Eu solution, but only to up to a certain level (0.4 mg Gd/1 mg Eu).



(A)



(B)

FIGURE 3: Predicted specific activities of the main radioisotopes created in the production of  $^{153}\text{Gd}$  from (a) continuous irradiation and (b) irradiation according to MNR schedule of  $^{152}\text{Gd}$  enriched  $\text{Gd}_2\text{O}_3$  ( $\phi = 2.5 \times 10^{13} \text{ n cm}^{-2} \text{ s}^{-1}$ ).

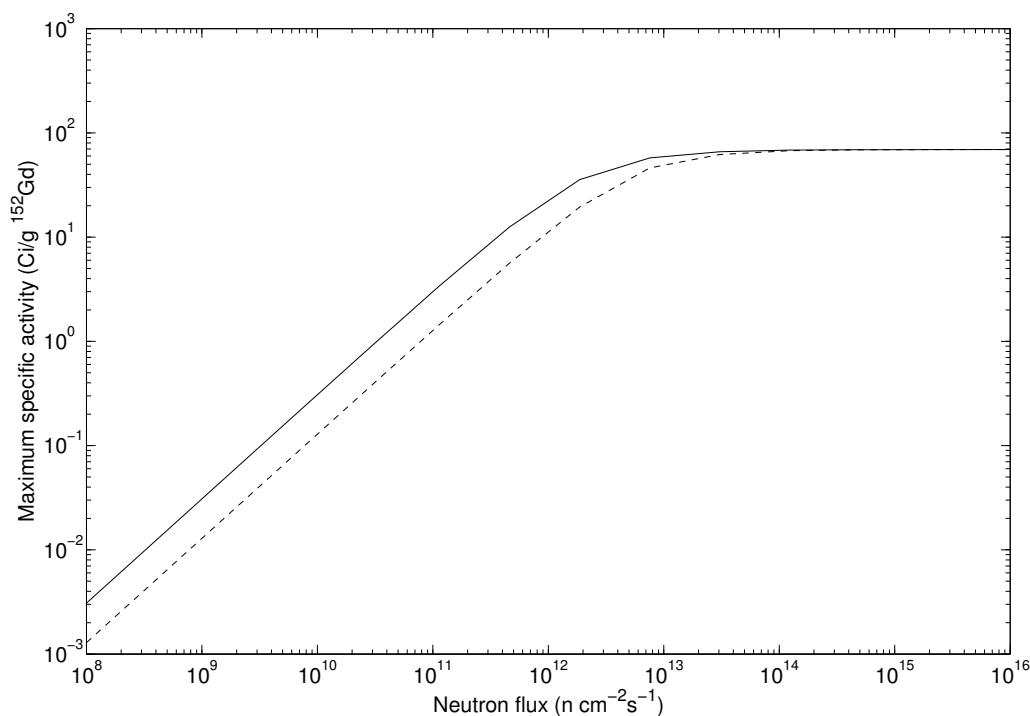


FIGURE 4: Effect of neutron flux on the maximum predicted specific activity of  $^{153}\text{Gd}$  from continuous irradiation (solid line) and irradiation according to MNR schedule (dashed line).

The indirect production of  $^{153}\text{Gd}$  from natural Eu should produce higher specific activity material than the direct route; however, it involves separating microgram quantities of Gd from tens of grams of Eu. The Eu/Gd separation technique via europium sulfate precipitation through a zinc column was demonstrated to be effective at removing large quantities of Eu from small amounts of Gd. This method can be implemented as a first strike method to remove the bulk of Eu and to equilibrate the concentrations of Gd and Eu in solution for the final processing step. The Gd can then be isolated from the remaining rare earths (Eu, Sm) by high pressure liquid chromatography (Ramey, 1988), electrochemical separation (Case, Acree, and Cutshall, 1967), or electrodeposition on solid platinum wire in ionic liquids (Glukhov, Greish, and Kustov, 2010). These techniques should work equally well for the chemical processing of  $^{153}\text{Gd}$  produced via the direct production route, where Eu concentrations are expected to be significantly lower than Gd concentrations.

### 3.4 Sorption of Gd on solid supports

Whether  $^{153}\text{Gd}$  is produced from  $^{152}\text{Gd}$  or  $^{151}\text{Eu}$ , it will most likely be isolated as an aqueous solution, chemically purified and converted to a solid for encapsulation as a brachytherapy source. One method to immobilize the radioisotope would be to load the solution onto a solid substrate for encapsulation. The loading capacities for the various sorbents tested are presented in Table 4. Dowex®50WX8-400 ion-exchange resin was found to have the largest loading capacity for Gd ( $131 \pm 8$  mg/g sorbent). While the sorbents were successful in loading significant amounts of Gd, large quantities of sorbent would be required to load small amount of radioisotope.

Since the specific activity of a Gd source is already limited by the high cross-section of  $^{153}\text{Gd}$  compared to  $^{152}\text{Gd}$ , loading Gd onto a sorbent will further restrict the achievable activity of a brachytherapy source. It is therefore crucial to use a sorbent with a high loading capacity for Gd and a high density. The sorbent must also be easy to manipulate, such that it can be easily encapsulated in a thin stainless steel capsule. The results suggest that Dowex®50WX8-400 ion-exchange resin is a prime candidate as a solid substrate for the encapsulation of  $^{153}\text{Gd}$ .

Sorbent	$m_{\text{Gd}}$ (mg)	$m_{\text{sorbent}}$ (mg)	$A_{\text{sorbent}}$ ( $\mu\text{Ci}$ )	$A_{\text{eluate}}$ ( $\mu\text{Ci}$ )	Loading capacity (mg/g)
Dowex®50WX8-400	51.0	357.9	89	4	136.4
	51.0	364.7	35	1	136.0
	51.0	410.4	46	1	121.6
AG®50W-X2	51.0	356.7	68	35	94.4
	51.0	395.7	31	16	85.0
	51.0	400.0	29	13	88.0
AG®50W-X12	51.0	372.3	73	9	122.0
	51.0	376.9	30	5	116.0
	51.0	373.5	37	5	120.3

TABLE 4: The loading capacities for various sorbents.

### 3.5 Sintering of $Gd_2O_3$

The density of  $Gd_2O_3$  in powder form at room temperature was  $2.07 \text{ g/cm}^3$ . After heating the  $Gd_2O_3$  overnight at  $1000 \text{ }^\circ\text{C}$ , the substance formed clumps and was substantially easier to manipulate. After sintering, the density was  $2.22 \text{ g/cm}^3$ , representing an increase of approximately 7 %. However, a density as high as  $7.4 \text{ g/cm}^3$  is reported in the literature (Patnaik, 2002), which may refer to the metal oxide state obtained after heating the substance to extremely high temperatures.  $Gd_2O_3$  should exhibit a more condensed (hexagonal) phase when heated to more than  $2100 \text{ }^\circ\text{C}$ , but less than its melting point of  $2400 \text{ }^\circ\text{C}$ . Commercially available furnaces should be able to reach these temperatures.

$Gd_2O_3$ , as obtained from commercial suppliers, is a very fine powder and is extremely difficult to handle. The substance is actually much less dense than the values quoted in the literature. Sintering  $Gd_2O_3$  offers the advantage to provide a substance that will be easier to manipulate and weigh, for example, before dissolving the powder in acid. If  $^{153}\text{Gd}$  is eventually produced and encapsulated as an oxide powder or a pressed oxide pellet, sintering the substance before encapsulation can also improve the achievable activity of a source.

### 3.6 Treatment time

Based on the predicted maximum achievable specific activity, density, and geometrical constraints of a  $^{153}\text{Gd}$  brachytherapy source, the maximum activity of a single source would be restricted to 200-300 mCi for the direct production pathway. The dose rate of a  $^{153}\text{Gd}$  source would be at least 250 times lower than that of an  $^{192}\text{Ir}$  source. In order to minimize treatment times,  $^{153}\text{Gd}$ -based HDR brachytherapy must be delivered using a multi-source, multi-catheter approach. Even if 10 sources are used simultaneously, we expect that the treatment times will increase from minutes to hours, which may not be realistic from a clinical perspective.

## 4 Conclusions

In this study, we have investigated the production capacity and maximum attainable specific activity of  $^{153}\text{Gd}$ . The major advantage of producing  $^{153}\text{Gd}$  through the direct production pathway is the possibility to irradiate pre-sealed pellets of  $^{152}\text{Gd}$  enriched  $\text{Gd}_2\text{O}_3$ , thereby removing the need to perform chemical separation in hot cells with large quantities of long-lived, high gamma emission radio-impurities. However, chemical purification may still be required to improve the radionuclidic purity of the source, if the amount of the long-lived radio-impurities produced is deemed unacceptable. In that case, the  $^{153}\text{Gd}$  will be isolated as an aqueous solution, and can be loaded onto a solid substrate such as a sorbent with a high affinity for Gd, or through electrodeposition onto a platinum wire. The maximum specific activity of  $^{153}\text{Gd}$  may limit the viability of this radioisotope as a potential novel source for HDR brachytherapy.

## Acknowledgements

We would like to acknowledge support from the CREATE Medical Physics Research Training Network grant (number 432290) of the Natural Sciences and Engineering Research Council (NSERC), discovery grant (number 241018).

# Appendix

## System of equations

$$\begin{aligned}
\frac{dN_{152Gd}}{dt} &= 0.72\lambda_{152m1Eu}N_{152m1Eu} + 0.28\lambda_{152Eu}N_{152Eu} - \phi\sigma_{152Gd}N_{152Gd} \\
\frac{dN_{153Gd}}{dt} &= \phi\sigma_{152Gd}N_{152Gd} - \lambda_{153Gd}N_{153Gd} - \phi\sigma_{153Gd}N_{153Gd} \\
\frac{dN_{154Gd}}{dt} &= \phi\sigma_{153Gd}N_{153Gd} + \lambda_{154Eu}N_{154Eu} - \phi\sigma_{154Gd}N_{154Gd} \\
\frac{dN_{155Gd}}{dt} &= \phi\sigma_{154Gd}N_{154Gd} + \lambda_{155Eu}N_{155Eu} - \phi\sigma_{155Gd}N_{155Gd} \\
\frac{dN_{156Gd}}{dt} &= \phi\sigma_{155Gd}N_{155Gd} + \lambda_{156Eu}N_{156Eu} - \phi\sigma_{156Gd}N_{156Gd} \\
\frac{dN_{157Gd}}{dt} &= \phi\sigma_{156Gd}N_{156Gd} + \lambda_{157Eu}N_{157Eu} - \phi\sigma_{157Gd}N_{157Gd} \\
\frac{dN_{158Gd}}{dt} &= \phi\sigma_{157Gd}N_{157Gd} - \phi\sigma_{158Gd}N_{158Gd} \\
\frac{dN_{159Gd}}{dt} &= \phi\sigma_{158Gd}N_{158Gd} - \lambda_{159Gd}N_{159Gd} - \phi\sigma_{159Gd}N_{159Gd} \\
\frac{dN_{160Gd}}{dt} &= \phi\sigma_{159Gd}N_{159Gd} - \phi\sigma_{160Gd}N_{160Gd} \\
\frac{dN_{161Gd}}{dt} &= \phi\sigma_{160Gd}N_{160Gd} - \lambda_{161Gd}N_{161Gd} \\
\frac{dN_{151Eu}}{dt} &= -\phi\sigma_{151Eu}^a N_{151Eu} - \phi\sigma_{151Eu}^b N_{151Eu} \\
\frac{dN_{152m1Eu}}{dt} &= \phi\sigma_{151Eu}^a N_{151Eu} - \lambda_{152m1Eu}N_{152m1Eu} - \phi\sigma_{152m1Eu}N_{152m1Eu} \\
\frac{dN_{152Eu}}{dt} &= \phi\sigma_{151Eu}^b N_{151Eu} - \lambda_{152Eu}N_{152Eu} - \phi\sigma_{152Eu}N_{152Eu} \\
\frac{dN_{153Eu}}{dt} &= \phi\sigma_{152m1Eu}N_{152m1Eu} + \phi\sigma_{152Eu}N_{152Eu} + \lambda_{153Gd}N_{153Gd} \\
&\quad + \lambda_{153Sm}N_{153Sm} - \phi\sigma_{153Eu}N_{153Eu} \\
\frac{dN_{154Eu}}{dt} &= \phi\sigma_{153Eu}N_{153Eu} - \lambda_{154Eu}N_{154Eu} - \phi\sigma_{154Eu}N_{154Eu} \\
\frac{dN_{155Eu}}{dt} &= \phi\sigma_{154Eu}N_{154Eu} - \lambda_{155Eu}N_{155Eu} - \phi\sigma_{155Eu}N_{155Eu}
\end{aligned}$$

$$\begin{aligned}
\frac{dN_{156Eu}}{dt} &= \phi\sigma_{155Eu}N_{155Eu} - \lambda_{156Eu}N_{156Eu} - \phi\sigma_{156Eu}N_{156Eu} \\
\frac{dN_{157Eu}}{dt} &= \phi\sigma_{156Eu}N_{156Eu} - \lambda_{157Eu}N_{157Eu} - \phi\sigma_{157Eu}N_{157Eu} \\
\frac{dN_{158Eu}}{dt} &= \phi\sigma_{157Eu}N_{157Eu} - \lambda_{158Eu}N_{158Eu} \\
\frac{dN_{152Sm}}{dt} &= 0.28\lambda_{152m1Eu}N_{152m1Eu} + 0.72\lambda_{152Eu}N_{152Eu} - \phi\sigma_{152Sm}N_{152Sm} \\
\frac{dN_{153Sm}}{dt} &= \phi\sigma_{152Sm}N_{152Sm} - \lambda_{153Sm}N_{153Sm} - \phi\sigma_{153Sm}N_{153Sm} \\
A_{153Gd} &= \lambda_{153Gd}N_{153Gd} \\
A_{159Gd} &= \lambda_{159Gd}N_{159Gd} \\
A_{161Gd} &= \lambda_{161Gd}N_{161Gd} \\
A_{152m1Eu} &= \lambda_{152m1Eu}N_{152m1Eu} \\
A_{152Eu} &= \lambda_{152Eu}N_{152Eu} \\
A_{154Eu} &= \lambda_{154Eu}N_{154Eu} \\
A_{155Eu} &= \lambda_{155Eu}N_{155Eu} \\
A_{156Eu} &= \lambda_{156Eu}N_{156Eu} \\
A_{157Eu} &= \lambda_{157Eu}N_{157Eu} \\
A_{158Eu} &= \lambda_{158Eu}N_{158Eu} \\
A_{153Sm} &= \lambda_{153Sm}N_{153Sm}
\end{aligned}$$

## Parameters

Cross section	(b)	Decay constant	(h <sup>-1</sup> )	Flux	(n cm <sup>-2</sup> s <sup>-1</sup> )
$\sigma_{152}Gd$	1100	$\lambda_{153}Gd$	$1.19 \times 10^{-4}$	$\phi$	$2.5 \times 10^{13}$
$\sigma_{153}Gd$	20000	$\lambda_{159}Gd$	$3.75 \times 10^{-2}$		
$\sigma_{154}Gd$	85	$\lambda_{161}Gd$	$1.16 \times 10^1$		
$\sigma_{155}Gd$	60900	$\lambda_{152m1}Eu$	$7.45 \times 10^{-2}$		
$\sigma_{156}Gd$	1.5	$\lambda_{152}Eu$	$5.86 \times 10^{-6}$		
$\sigma_{157}Gd$	259000	$\lambda_{154}Eu$	$9.20 \times 10^{-6}$		
$\sigma_{158}Gd$	3	$\lambda_{155}Eu$	$1.66 \times 10^{-5}$		
$\sigma_{159}Gd$	50	$\lambda_{156}Eu$	$1.90 \times 10^{-3}$		
$\sigma_{160}Gd$	1	$\lambda_{157}Eu$	$4.56 \times 10^{-2}$		
$\sigma_{151}^a Eu$	3300	$\lambda_{158}Eu$	$9.06 \times 10^{-1}$		
$\sigma_{151}^b Eu$	5900	$\lambda_{153}Sm$	$1.50 \times 10^{-2}$		
$\sigma_{152m1}Eu$	12800				
$\sigma_{152}Eu$	70000				
$\sigma_{153}Eu$	350				
$\sigma_{154}Eu$	1500				
$\sigma_{155}Eu$	3950				
$\sigma_{156}Eu$	400				
$\sigma_{157}Eu$	200				
$\sigma_{158}Eu$	208				
$\sigma_{153}Sm$	400				

TABLE 5: Parameters for the simulation.

# Bibliography

- AAPM and ESTRO (2012). "Dose calculation for photon-emitting brachytherapy sources with average energy higher than 50 keV: report of the High Energy Brachytherapy Source Dosimetry (HEBD) Working Group". In:
- Abdushukurov, D A et al. (2007). "Modeling the registration efficiency of thermal neutrons by gadolinium foils". In: *J. Instrumentation* 2.04, P04001.
- Adams, Quentin E et al. (2014). "Interstitial rotating shield brachytherapy for prostate cancer". In: *Med. Phys.* 41.5, p. 051703.
- Case, F N, E H Acree, and N H Cutshall (1967). *Production study of gadolinium-153*. Tech. rep. Oak Ridge National Laboratory, Oak Ridge, TN, United States.
- Chu, S Y F, L B Ekstrom, and R B Firestone (1999). *The Lund/LBNL Nuclear Data Search Version 2.0*. URL: <http://nucleardata.nuclear.lu.se/toi/>.
- Enger, Shirin A, Darrell R Fisher, and Ryan T Flynn (2013). "Gadolinium-153 as a brachytherapy source". In: *Phys. Med. Biol.* 58.4, pp. 957–64.
- Gluhkov, L M, A A Greish, and L M Kustov (2010). "Electrodeposition of rare earth metals Y, Gd, Yb in ionic liquids". In: *Russ. J. Phys. Chem.* 84.1, pp. 104–8.
- Heft, R E (1978). *Conf. on Computers in Activ. Analysis*. Tech. rep., p. 495.
- Holden, Norman E (1986). *Neutron cross-sections for  $^{152}\text{Gd}$  and  $^{153}\text{Gd}$* . Tech. rep. Brookhaven National Laboratory, Upton, NY, United States.
- ICRU (1985). *Report 38: Dose and volume specification for reporting intracavitary therapy in gynecology*. Tech. rep. International Commission on Radiation Units & Measurements.
- ISO (2012). *ISO 2919:2012 Radiological protection - Sealed radioactive sources - General requirements and classification*. Tech. rep. International Organization for Standardization, Geneva, Switzerland.

- Johnsen, Amanda M et al. (2013). "A non-aqueous reduction process for purifying  $^{153}\text{Gd}$  produced in natural europium targets". In: *Appl. Radiat. Isot.* 82, pp. 158–65.
- Kopecky, J et al. (1999). *Atlas of neutron capture cross sections*. Tech. rep. International Nuclear Data Committee, International Atomic Energy Agency, Netherlands.
- Lee, J Y et al. (2011). "Measurements of thermal neutron cross sections". In: *J. Kor. Phys. Soc.* 59.2.
- Nath, Ravinder et al. (2016). "Guidelines by the AAPM and GEC-ESTRO on the use of innovative brachytherapy devices and applications: report of Task Group 167". In: *Med. Phys.* 43.6, pp. 3178–205.
- Patnaik, Pradyot (2002). *Handbook of inorganic chemicals*. New York, NY, United States: McGraw Hill.
- Ramey, D W (1988). *Gadolinium-153 production at the Oak Ridge National Laboratory*. Tech. rep. Oak Ridge National Laboratory, Oak Ridge, TN, United States.
- Steinnes, E (1972). In: *J. Inorg. Nucl. Chem.* 34, p. 2699.
- Xiaolong, H (2010). "Evaluation of the decay data of  $^{153}\text{Gd}$ ". In: *Appl. Radiat. Isot.* 68.1, pp. 18–22.